

MOMENTUM CONTROL SYSTEMS AND THEIR
APPLICATION IN ROBOTIC SYSTEMS

A Dissertation

Presented to the Faculty of the Graduate School

of Cornell University

In Partial Fulfillment of the Requirements for the Degree of

Doctor of Philosophy

by

David Sawyer Elliott

December 2019

© 2019 David Sawyer Elliott

MOMENTUM CONTROL SYSTEMS AND THEIR APPLICATION IN ROBOTIC SYSTEMS

David Sawyer Elliott, Ph. D.

Cornell University 2019

This dissertation advances the field of momentum control systems, specifically control momentum gyroscopes (CMGs), with three main contributions. The first two contributions improve the generality and performance of constraint-based steering laws for CMGs, while the third focuses on a novel implementation of CMGs that exploits their torque efficiency.

First, this work provides analytical, closed-form gimbal-angle constraint functions that maximize the performance for CMG arrays with parallel gimbal axes. The analytical solutions define an optimal gimbal-angle set for a given angular-momentum state for any planar array with four or more CMGs. Proofs verify the global optimality of the provided gimbal-angle set constraints for nearly all angular-momentum states. A numerical assessment provides evidence of global optimality for the remaining angular-momentum states. In conjunction with previously developed constraint implementations methods, the provided constraints offer a general, high-performance, and fault-tolerant steering law. Simulations comparing the performance of this approach to that of an existing constraint-based method illustrates its improvement. The resulting steering law is also broadly applicable to aerospace and robotics problems. These constraints optimize velocity-tracking capability of planar serial manipulators, resulting in a control method that enables robotic end effectors to track large velocities, benefiting many tasks such as rapid mobile manipulation. Due to their generality, the constraint functions are also applicable to hyper-redundant multi-degree-of-freedom systems, including snake-like robots, enabling high-performance singularity avoidance.

Second, this work provides a closed-form constraint-based steering law for the four-CMG box-90 array, one of the most common arrays in practice. The steering law offers guaranteed avoidance of all internal singularities. Furthermore, performance guarantees dictate a maximum torque magnitude that the array is capable of producing in all directions, within the array's mechanical limitations. These performance guarantees increase the robustness of the overall control architecture by enabling maneuvers to be designed such that the torque commands remain bounded by the available torque. They also enable the CMGs for a particular application to be sized without the need for inexact numerical methods, such as Monte Carlo simulations. The proposed steering law is compared to the local-gradient steering law, which highlights its benefits over this and other candidate laws for the four-CMG box-90 array.

Finally, this dissertation focuses on a novel implementation of CMGs that exploits their torque efficiency. Specifically, it explores a polyhedral rover that uses a CMG for rolling locomotion. Unlike reaction wheels, which have been used in similar rovers to enable hopping and tumbling motions, CMGs have not been explored extensively. Nevertheless, their torque and energy efficiency make them well suited for rover applications, motivating the development of design principles and control architectures that use CMGs effectively. This dissertation explores how exploiting the interaction between the chassis and the ground through morphology and control design, enables the rover with just one CMG to locomote over extreme terrain more efficiently and predictably, compared to other contemporary rover architectures.

BIOGRAPHICAL SKETCH

D. Sawyer Elliott graduated from Rochester Institute of Technology with a Bachelor of Science in Mechanical Engineering in 2015. During his undergraduate career he worked at Massachusetts Institute of Technology Lincoln Laboratory, where he worked on small spacecraft for weather sensing. Currently, he is a Ph.D. candidate at Cornell University under Professor Mason Peck, with a focus on dynamics and controls. While at Cornell University he worked on a small spacecraft project with the goal of autonomously docking two CubeSats. His PhD research explores control methods for momentum control systems, as well as the control of gyroscopically actuated robotic systems and their applications for extreme terrain exploration. Upon completion of his PhD he will continue to develop novel control methodologies for aerospace vehicles at Johns Hopkins Applied Physics Laboratory.

ACKNOWLEDGEMENTS

I am incredibly grateful for the many individuals who have provided me with generous support and encouragement throughout my graduate career. To Dr. Mason Peck, thank you for your patience and support through this process. From developing research ideas to achieving my career goals, you have provided instrumental help and insights that had made everything possible. To Dr. Issa Nesnas, thank you for the generous time and insightful comments you have provided not only for my work, but also for my career development. To my committee members, Drs. Ross Knepper and Douglas MacMartin, thank you for your suggestions and advice for this dissertation work. Thank you to all of my fellow PhD students who have been a great source of help and inspiration for my research and career goals.

Thank you, Patti Wojock and Marica Sawyer, for all of your help getting through the maze of administrative tasks associated with finishing a PhD. Thank you to all of the undergraduate and graduate students that have worked with me on the development of the rover architecture.

To my father, who would sacrifice anything for me to get a good education, thank you. To Xinqi, thank you for your unwavering support that made this journey possible, and your humor that kept it all fun.

Lastly, this dissertation work would not have been possible without the generous support of the NASA Space Technology Research Fellowship.

TABLE OF CONTENTS

Chapter 1 Introduction	9
1.1 Contributions.....	10
Chapter 2 Control Moment Gyroscopes	12
2.1 Dynamics	12
2.2 Steering Laws.....	14
2.2.1 Singularities	17
2.2.2 Torque Capability	18
2.2.3 Desired Capabilities	18
2.3 Current Methodologies	19
2.4 Limitations	20
2.5 Constraint-Based Steering Laws.....	21
2.5.1 Past work.....	24
Chapter 3 Planar Array	26
3.1 Torque Capability Optimization	26
3.1.1 Planar Array Simplifications.....	29
3.2 Planar Array Constraints.....	30
3.2.1 Arrays with an Even Number of CMGs Greater Than Three.....	31
3.2.2 Arrays with Five CMGs.....	33
3.2.3 Arrays with Seven CMGs	34
3.2.4 Arrays with an Odd Number of CMGs Greater Than Seven.....	36
3.2.5 Implementation	38
3.3 Comparison.....	40
3.4 Conclusion	47
Chapter 4 Four CMG Roof Array.....	49
4.1 Box-90 Singularities	50
4.2 Box-90 Constraint Function.....	54
4.3 Steering Law Performance.....	57
4.4 Performance Comparison.....	64
4.4.1 Methodology	66
4.4.2 Results.....	68
4.5 Conclusion	73
Chapter 5 Polyhedral Extreme Terrain Exploration Rover.....	75
5.1 Previous Research.....	76
5.2 Rover Design	76
5.3 PETER's Dynamics	79
5.3.1 Dynamics Derivation	81
5.4 Control Architecture	85
5.4.1 Step Trajectory Planner.....	86
5.4.2 Step Tracking Controller.....	90
5.5 PETER's Predicted Performance.....	91
5.5.1 Experimental Rover Specifications.....	92
5.5.2 Analysis Techniques	93

5.5.3	Results.....	95
5.5.4	Discussion.....	97
5.6	Contextualization of Performance	98
5.6.1	Evaluated Steps.....	99
5.6.2	Results.....	102
5.6.3	Discussion.....	104
5.7	Conclusion	105
Chapter 6	Conclusion.....	107
Appendix	109
7.1	Torque Capability Derivation	109
7.1.1	Moore-Penrose pseudoinverse.....	109
7.1.2	Four-CMG Box-90 and the Augmented Jacobian Method.....	113
7.1.3	Four-CMG Box-90 and the Local Gradient Steering Law	116
7.2	Proofs of Global Optimality for Planar Array Constraints.....	119
7.2.1	Arrays with an Even Number of CMGs Greater Than Three.....	123
7.2.2	Arrays with an Odd Number of CMGs More Than Three.....	127
7.3	Spherical Constraint Function for Four CMG Box-90 Array.....	132
7.4	PETER's Chassis Shape	134
References	137

LIST OF SYMBOLS

$\hat{\mathbf{a}}$	= Unit vector a
\mathbf{V}	= Vector V
${}^A\mathbf{V}$	= Vector V represented in coordinate system A
$\underline{\mathbf{I}}$	= Inertia dyadic I
$\boldsymbol{\omega}^{A/B}$	= Angular velocity of the A reference frame relative to the B frame
$\mathbf{V} \cdot \mathbf{U}$	= The dot product of vectors V and U
$\mathbf{V} \times \mathbf{U}$	= The cross product of vectors V and U
$\frac{c_d}{dt} \boldsymbol{\omega}^{A/B}$	= The derivative of $\boldsymbol{\omega}^{A/B}$ with respect to the frame C
$\frac{c_{d^2}}{dt^2} \boldsymbol{\omega}^{A/B}$	= Derivative with respect to the frame C of $\frac{c_d}{dt} \boldsymbol{\omega}^{A/B}$
\dot{v}	= The time derivative of the scalar v
A^T	= The transpose of matrix A
A^{-1}	= The inverse of matrix A
A^+	= The Moore-Penrose pseudoinverse of matrix A
$\det(A)$	= The determinant of matrix A
$N(A)$	= The matrix representation of the null space of matrix A
$\text{adj}(A)$	= Adjoint matrix of matrix A

$\|C\|_n$ = l^n -norm of the column matrix C

$\lfloor x \rfloor$ = Resulting integer from rounding the value of x down to the nearest integer

$\lceil x \rceil$ = Resulting integer from rounding the value of x up to the nearest integer

$A(i, j)$ = The value of matrix A in the i^{th} row and the j^{th} column

$I_{n \times n}$ = n by n identity matrix

$|s|$ = Absolute value of the scalar s

CHAPTER 1 INTRODUCTION

A momentum control system (MCS) actuates the rotational degrees of freedom (DoFs) of a body through internal motion. MCSs commonly used for the actuation of spacecraft for two main reasons. First, MCSs enable agile motion due to their power-efficient production of torque. Second, MCSs do not require an expendable resource like propellant to operate. The two most common MCS technologies are reaction wheels (RWs) and control moment gyroscopes (CMGs). A RW applies torque to a system by changing its own angular-momentum magnitude. In contrast, a CMG applies a torque primarily by changing its own angular-momentum direction, imparting a gyroscopic torque between the CMG and the body to which it is mounted. Specifically, a CMG usually comprises a constant-speed rotor mounted on a gimbal that can tilt the rotor to redirect the momentum. Because CMGs apply torque gyroscopically, they can produce large output torques efficiently with respect to power, weight, and volume. They offer orders-of-magnitude greater power efficiency than similarly sized RWs, making them widely applicable for spacecraft, ships, robotic systems, among others [1]–[8].

Like any MCS, an array of CMGs can become singular. A singularity is a state of the array in which the array is incapable of producing torque in one or more directions. Unlike RW arrays, which become singular only when the wheels reach maximum speed, CMG arrays can also become singular even when individual devices are not saturated, i.e., when the momentum of the array is within its maximum envelope [1]. For applications where it is critical to be able to track a desired trajectory, singularities must be avoided. However, simply avoiding singularities is often insufficient in practical applications, where a CMG's mechanical limitations limit the torque that the array can produce as the array approaches a singularity. To enable the array to produce a desired

torque, the array must not only avoid singularities but also must stay sufficiently far from them, such that the mechanical limitations do not prohibit the production of the torque. In general, maximizing torque capability, i.e., the amount of torque that the array can produce within its limitations, maximizes the control authority the array has over the system. So, such a solution helps minimize size, weight, and power. This perspective, maximizing torque capability vs. mere singularity avoidance, is an unusual but powerful one that informs the present work.

1.1 Contributions

This dissertation discusses three main research contributions. The first two contributions focus on the development of high-performance steering laws. Specifically, a general steering law for planar array architecture is provided that globally maximizes the array's torque capability in closed form. The generality of the steering law results in fault-tolerant operations, where one or more CMGs can fail, and yet the steering law can still perform optimally. The closed-form formulation eliminates the need for implementing numerical methods in an operational environment, resulting in a predictable and computationally efficient steering law. A comparison between the provided steering law and a state-of-the-art methodology shows the increased torque capability of the provided constraint. This dissertation also offers a closed-form steering law that has higher performance than contemporary methods for the four-CMG box-90 array, one of the most common arrays in practice. Additionally, performance guarantees are developed for the steering law, enabling the performance of the array to be computed analytically. These guarantees enable systems to be more robust by enabling motions to be planned such that they are guaranteed to be achievable. A comparison between a state-of-the-art steering law and the provided steering law highlights the main benefit of the provided steering law: performance guarantees.

The final contribution of this work is a novel rover architecture that exploits the torque efficiency of the CMGs to enable efficient locomotion through extreme terrain on a wide array of planetary bodies. Specifically, this dissertation provides design principles for the rover architecture and a control architecture for the rover that enables predictable and efficient locomotion through extreme terrain. A comparison of a contemporary rover architecture to the proposed rover architecture shows that the CMG-based architecture uses less energy than contemporary rovers, highlighting the torque efficiency CMGs.

The dissertation is structured as follows. Chapter 2 provides a general overview of CMGs, their dynamics, and steering laws. Chapter 3 discusses the general steering law for planar CMG arrays. Chapter 4 discusses the steering law for the four-CMG box-90 array. Chapter 5 discusses the novel rover architecture for exploration of extreme terrain. Chapter 6 provides a conclusion for the dissertation.

CHAPTER 2 CONTROL MOMENT GYROSCOPES

There are many types of CMGs; all exploit the gyroscopic effect of tilting a spinning rotor to change momentum, imparting an internal torque to the vehicle. The two most common are single-gimbal CMGs (SGCMGs) and dual-gimbal CMGs (DGCMGs) with fixed-speed rotors. A SGCMG can apply torque only in a plane. A DGCMG has one more actuation degree of freedom (DoF) than a SGCMG, but at the cost of torque efficiency with respect to size, weight and energy usage [1], [9]. Much less common, both types of CMGs can use variable-speed rotors. Variable speed allows the CMG to apply torque along the angular-momentum vector of the rotor, adding an actuation DoF. However, the spin torque is typically orders of magnitude lower than the gyroscopic torque, making it minimally useful [1]. Allowing speed variation increases the overall CMG mass and complexity, decreases energy efficiency, and introduces control-related singularity problems [1]. Fixed-speed SGCMGs are solely discussed in this dissertation because of their mechanical robustness and torque efficiency with respect to rotor size. Thus, in the present work, unless otherwise stated, the term CMG refers to a fixed-speed SGCMG. A collection of multiple CMGs is known as an array of CMGs. Many different array architectures exist. For this dissertation, it is assumed that all arrays are uniform, meaning all CMGs have identical angular momentum and mechanical capabilities.

2.1 Dynamics

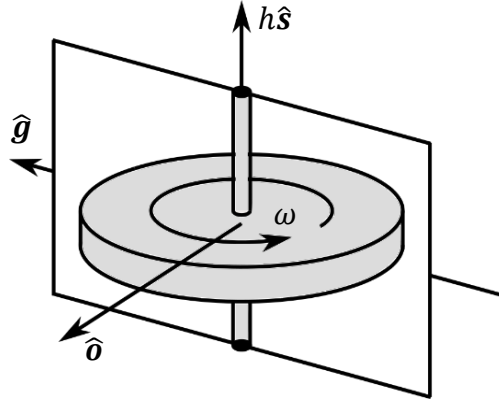


Figure 1. Coordinate system of a CMG. *The rotor pictured here rotates at a rate, ω about the \hat{s} axis, storing angular momentum in the \hat{s} direction. That rotor tilts about the gimbal axis, \hat{g} , at a gimbal rate $\dot{\delta}$, generating a torque felt by the system in the output torque direction, \hat{o} . As the CMG applies torque by rotating its rotor about the gimbal axis, the angular-momentum direction and output torque direction rotate with respect to the system by a gimbal angle, δ .*

Figure 1 shows a CMG and its gimbal-fixed frame of reference, G, with an associated coordinate system. With n CMGs, there are n individual gimbal coordinate systems. The N, B and R frames are not shown, but they represent an inertial frame of reference, a body-fixed frame of reference and a rotor-fixed frame of reference, respectively.

To apply torque to a body, a steering law manipulates the total angular momentum of an array of CMGs by gimbaling each CMG rotor. The angular momentum of a body with n identical CMGs is shown in Eq. (1), where \mathbf{H}_b represents the bodies angular momentum, and \mathbf{I}_r and \mathbf{I}_g represent the CMGs' rotor inertia dyadic about their center of mass, the inertia dyadic of the CMGs' gimbal assembly about their center of mass, respectively.

$$\mathbf{H}_{total} = \mathbf{H}_b + \mathbf{H}_{CMG} = \mathbf{H}_b + \sum_{i=1}^n (\mathbf{I}_r \cdot \boldsymbol{\omega}^{R_i/N} + \mathbf{I}_g \cdot \boldsymbol{\omega}^{G_i/N}) \quad (1)$$

Taking the derivative of Eq. (1) yields the equation of motion, where \mathbf{T} is the torque the array imparts on the body. Equation (2) assumes that there are no external torques acting on the system.

$$\mathbf{T} = \frac{N_d}{dt} \mathbf{H}_b \quad (2)$$

$$\mathbf{T} = - \sum_{i=1}^n \left(\underline{\mathbf{I}}_r \cdot \frac{G_i d}{dt} \boldsymbol{\omega}^{R_i/G_i} + (\underline{\mathbf{I}}_r + \underline{\mathbf{I}}_g) \cdot \frac{G_i d}{dt} \boldsymbol{\omega}^{G_i/B} + (\underline{\mathbf{I}}_r + \underline{\mathbf{I}}_g) \cdot \frac{B_d}{dt} \boldsymbol{\omega}^{B/N} \right. \\ \left. + \boldsymbol{\omega}^{G_i/N} \times (\underline{\mathbf{I}}_r \cdot \boldsymbol{\omega}^{R_i/N} + \underline{\mathbf{I}}_g \cdot \boldsymbol{\omega}^{G_i/N}) - (\underline{\mathbf{I}}_r + \underline{\mathbf{I}}_g) \cdot (\boldsymbol{\omega}^{G_i/B} \times \boldsymbol{\omega}^{B/N}) \right) \quad (3)$$

2.2 Steering Laws

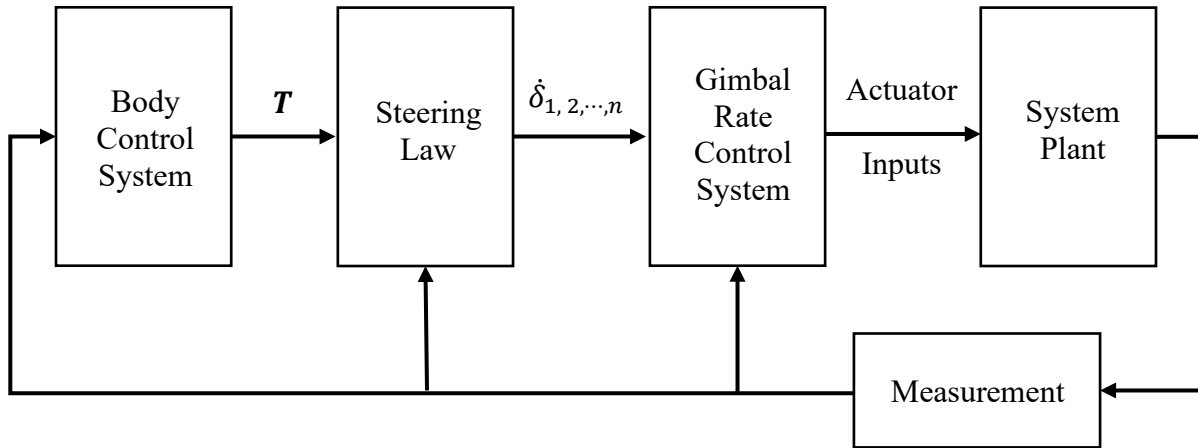


Figure 2. Feedback control system.

The output torque, \mathbf{T} , is applied to the body. \mathbf{T} is an output of the MCS but is considered an input in the feedback-control sense. Figure 2 shows a common control architecture for a system with a CMG array. To achieve a desired motion of the body, a body control system commands \mathbf{T} as part of this feedback-control architecture. The steering law then determines the gimbal rates to achieve the command. A low-level control system computes actuator inputs to achieve the desired gimbal rates.

The complexity of \mathbf{T} greatly complicates the development of a steering law. However, Eq. (3) can be simplified by first recognizing that the CMG's rotor spins at a constant rate, resulting in $\frac{G_i d}{dt} \boldsymbol{\omega}^{R_i/G_i}$ being zero. Additionally, the rotor spins at a high speed (thousands of RPM) while the gimbal and the resultant body rotations and accelerations are much smaller, thus $\boldsymbol{\omega}^{R_i/G_i}$ is much larger than, $\frac{B d}{dt} \boldsymbol{\omega}^{B/N}$, $\frac{G_i d}{dt} \boldsymbol{\omega}^{G_i/B}$, $\boldsymbol{\omega}^{G_i/B}$, and $\boldsymbol{\omega}^{B/N}$. As a result, while a detailed simulation would include the full physics, steering-law synthesis and system design can proceed without explicitly accommodating them [1]. Incorporating the simplifications into Eq. (3) yields Eq. (4).

$$\mathbf{T} = - \sum_{i=1}^n \boldsymbol{\omega}^{G_i/N} \times (\underline{\mathbf{L}}_r \cdot \boldsymbol{\omega}^{R_i/G_i}) \quad (4)$$

Equation (4) is split into two terms: the output torque, \mathbf{T}_o , and the base-rate torque, \mathbf{T}_b . Equation (5) shows the output torque, where h_i is the magnitude of the angular momentum of the i^{th} CMG, $\dot{\delta}_i$ is the i^{th} CMG's gimbal rate, $\hat{\boldsymbol{\theta}}_i$ is the direction that the CMG's gyroscopic torque is applied when rotated about the gimbal axis.

$$\mathbf{T}_o = - \sum_{i=1}^n \left(\boldsymbol{\omega}^{G_i/B} \times (\underline{\mathbf{L}}_r \cdot \boldsymbol{\omega}^{R_i/G_i}) \right) = \sum_{i=1}^n h \dot{\delta}_i \hat{\boldsymbol{\theta}}_i \quad (5)$$

A CMG can apply this so-called output torque anywhere in a plane, but not instantaneously. The direction of the output torque depends on the instantaneous gimbal angle δ . Equation (6) represents the base-rate torque of the CMG.

$$\mathbf{T}_b = - \sum_{i=1}^n \boldsymbol{\omega}^{B/N} \times (\underline{\mathbf{L}}_r \cdot \boldsymbol{\omega}^{R_i/G_i}) \quad (6)$$

For most practical applications, the body rate, $\boldsymbol{\omega}^{B/N}$, is small compared to the gimbal rates, enabling the base rate torque to be treated as a disturbance when synthesizing a steering law, simplifying Eq. (2) to Eq. (7) [1].

$$\mathbf{T} = \sum_{i=1}^n h \dot{\delta}_i \hat{\boldsymbol{\delta}}_i = \frac{N_d}{dt} \mathbf{H}_b \quad (7)$$

The output torque of the CMG array is rewritten as a matrix equation, where $\hat{\boldsymbol{\delta}}_i$ is the 3x1 matrix representation of $\hat{\boldsymbol{\delta}}_i$, and T is the matrix representation of the vector \mathbf{T} . For brevity, the coordinate system for the matrix representation is not shown, but the coordinates are consistent for all CMGs and torque.

$$T = h[\hat{\boldsymbol{\delta}}_1, \hat{\boldsymbol{\delta}}_2, \dots, \hat{\boldsymbol{\delta}}_n] \begin{bmatrix} \dot{\delta}_1 \\ \dot{\delta}_2 \\ \vdots \\ \dot{\delta}_n \end{bmatrix} = hJ \begin{bmatrix} \dot{\delta}_1 \\ \dot{\delta}_2 \\ \vdots \\ \dot{\delta}_n \end{bmatrix} \quad (8)$$

Steering laws are designed to compute a gimbal-rate set such that the array produces a desired T . If the array has the same number of CMGs as the body has rotational degrees of freedom (generally three), then the Jacobian, J , is square, enabling the gimbal-rate set that achieves a desired torque to be calculated by a simple matrix inversion, as shown in Eq. (9), for the likely case of identical angular-momentum magnitude (h) for all CMGs.

$$\begin{bmatrix} \dot{\delta}_1 \\ \dot{\delta}_2 \\ \vdots \\ \dot{\delta}_n \end{bmatrix} = \frac{J^{-1}T}{h} \quad (9)$$

However, in this case, because there is a unique set of gimbal rates to achieve a desired torque, there is no way to avoid singularities or progress the array to gimbal-angle sets that maximize

torque capability. For these reasons, arrays often have more CMGs than rotational degrees of freedom. Thanks to the redundancy of such arrays, infinite gimbal-angle sets exist that achieve the same array angular-momentum state. Consequently, infinite gimbal-rate sets can achieve a desired torque. Each unique gimbal-rate set produces a unique array motion, but all achieve the same desired torque. Equation (10) shows all possible gimbal rate sets that achieve a desired torque, where $N(J)$ is the matrix representation of the null space of J , J^+ is the Moore-Penrose pseudoinverse of J , $\det(JJ^T)$ is the determinant of JJ^T , $\text{adj}(JJ^T)$ is the adjoint of JJ^T , and U is a control-input matrix.

$$\begin{bmatrix} \dot{\delta}_1 \\ \dot{\delta}_2 \\ \vdots \\ \dot{\delta}_n \end{bmatrix} = J^+ \frac{T}{h} + N(J)^T U \quad (10)$$

$$J^+ = J^T (JJ^T)^{-1} = \frac{J^T \text{adj}(JJ^T)}{\Omega}$$

$$\Omega = \det(JJ^T)$$

Infinite combinations for U exist, each resulting in a different gimbal-rate set. Steering laws dictate U such that the array achieves desired performance characteristics.

2.2.1 Singularities

At some gimbal-angle sets, J is singular, i.e., it is not full rank. When the array is singular, Ω is equal to zero, resulting in J^+ being undefined. Singularities may be external or internal. External singularities occur when the array is saturated, i.e., the array has achieved its maximum possible angular momentum in a particular direction. The impact of external singularities on the array is often mitigated through proper sizing of actuators for a particular application [1]. Thus, these

singularities are not considered when developing steering laws. Internal singularities are gimbal-angle sets that result in the array being singular, but not saturated. For most applications, steering laws dictate U to avoid these internal singularities.

2.2.2 *Torque Capability*

Due to mechanical limitations, such as gimbal rate, the magnitude of torque that the array can produce is limited. These gimbal rate limitations result in arrays capability to produce torque progressing to zero as the array approaches a singularity. The capability of the array to produce torque given the mechanical limitations of the array is referred to as torque capability, TC . For this dissertation, TC is reported as a normalized quantity: the maximum magnitude of torque the array can produce in any direction relative to the maximum torque magnitude for each CMG (i.e., the product of a single CMG's maximum gimbal rate and its angular momentum). The maximum torque magnitude the array can produce in any direction, in contrast to any single direction, is explored because in many practical applications, torque commands are not known *a priori*. Thus, the array must be capable of producing a desired torque magnitude in any commanded direction. The array may be capable of producing a torque magnitude that exceeds TC in some directions. However, the array cannot produce more torque than specified by TC in all directions.

2.2.3 *Desired Capabilities*

For most applications there are four desired performance characteristics that steering laws should meet by appropriately dictating U [1], [10]–[12]. Steering laws should achieve a high level of TC , because maximizing TC maximizes the control authority that the array has over the system. So, such a solution helps minimize size, weight, and power. Additionally, achieving a non-zero

TC also guarantees the avoidance of all internal singularities. Steering laws should also be computationally tractable, enabling the array to be implemented on aerospace systems, which often have limited computational capability. Furthermore, steering laws should have predictable performance during operation, enabling the capabilities of the system to be accurately determined *a priori*. The most common application of CMGs is aerospace systems, for which it is critical that the system not only achieve high performance, but also have a high probability of mission success. Greater predictability of the array's performance enables desired maneuvers and operations to be planned such that the array can produce the desired motion, increasing the probability of mission success. Lastly, steering laws should achieve the above three performance characteristics for panoply of array architectures.

2.3 Current Methodologies

Currently, the most common singularity avoidance methods are trajectory-optimization steering laws, Local gradient (LG) steering laws, constraint-based (CB) steering laws, and singularity-robust steering laws [1], [11]. Trajectory-optimization steering laws plan motion for the array's gimbal angles that optimize a user-defined cost function, given a desired trajectory of the body [13]–[15]. For practical applications, it is impossible to perfectly model the systems dynamics and the disturbances acting on the system. These unmodeled effects necessitate a second steering law that does not require future knowledge to trim the array around the computed trajectory. Thus, the performance of these steering laws is largely dictated by the performance of the secondary steering law used to trim the array. These methods can also be computationally intensive due to the complex dynamics of many aerospace systems.

LG steering laws progress the array to a gimbal-angle set that maximizes a user-defined cost function, following the gradient of the cost function in real time [9], [16], [17]. These steering laws are computationally tractable, and for some arrays, the steering laws are capable of achieving a high level of TC . However, for many arrays, these steering laws do not guarantee singularity avoidance and so do not guarantee a non-zero level of TC . Additionally, there is no general way to predict the performance of these steering laws exactly. For most applications, inexact Monte Carlo simulations are used to predict array performance.

CB steering laws use the null motion of the array to progress the array to a gimbal-angle set defined by a set of constraint functions [10], [18]–[20]. These steering laws are computationally tractable. Additionally, for some arrays, these steering laws provide guaranteed singularity avoidance, guaranteeing a non-zero TC . Furthermore, these methodologies can offer performance guarantees that dictate the performance of the array during operation *a priori*. However, these steering laws are only applicable to a small number of array architectures.

Singularity-robust steering laws are distinct from the methods listed above because in addition to dictating U , these methods also manipulate the desired torque to nudge the system away from singularities [21]–[24]. These methods do not produce the desired motion of the body and so are not appropriate for missions requiring high pointing accuracy, greatly limiting their applicability.

2.4 Limitations

Currently, none of the developed methods achieve the four desired performance characteristics. Constraint-based steering laws achieve many of these desired characteristics; they are not computationally intensive, can guarantee singularity-free operation thus non-zero TC , and can

provide performance guarantees, but they often achieve a low level of TC [1], [12], [19]. Additionally, they are not broadly applicable. This dissertation aims to increase the generality and performance of constraint-based steering laws, with the goal of developing a steering law that meets the four desired performance characteristics.

2.5 Constraint-Based Steering Laws

CB steering laws progress the array to a gimbal-angle set that satisfies a set of constraint functions through the selection of U . There are two main parts to a CB steering law: the constraint functions and the implementation method. The constraints dictate the desired gimbal-angle set of the array during operation. The user can define any number of constraint functions. However, to fully resolve the redundancy of the array, often $n - m$ independent constraint functions are specified, where n is the number of CMGs and m is the number of rotational DOFs of the body [1], [25]. The general formulation considered in this dissertation of the constraint functions, F_i , is shown below, where F_i represents the i^{th} constraint function.

$$F_i(\delta_1, \delta_2, \dots, \delta_n) = 0 \quad (11)$$

The implementation method dictates the gimbal-rate sets to progress the array to the gimbal-angle state dictated by the constraint functions. There are two main implementation methods: the augmented Jacobian method [25]–[27] and the feedback control method [10]. The augmented Jacobian method progresses the array to a constrained gimbal-angle set by augmenting the array's Jacobian with the constraint functions' Jacobian, J_c , as shown in Eq. (12) [25].

$$\begin{bmatrix} \dot{\delta}_1 \\ \dot{\delta}_2 \\ \vdots \\ \dot{\delta}_n \end{bmatrix} = J_t^{-1} \begin{bmatrix} T \\ h \\ 0 \\ \vdots \\ 0 \end{bmatrix} \quad (12)$$

$$J_t = \begin{bmatrix} J \\ J_c \end{bmatrix}$$

$$J_c = \begin{bmatrix} \frac{\partial F_1}{\partial \delta_1} & \frac{\partial F_1}{\partial \delta_2} & \cdots & \frac{\partial F_1}{\partial \delta_n} \\ \frac{\partial F_2}{\partial \delta_1} & \frac{\partial F_2}{\partial \delta_2} & & \frac{\partial F_2}{\partial \delta_n} \\ \vdots & & \ddots & \vdots \\ \frac{\partial F_{n-m}}{\partial \delta_1} & & & \frac{\partial F_{n-m}}{\partial \delta_n} \end{bmatrix}$$

When the array starts at a gimbal-angle set that satisfies the constraint function and the control system implementing the gimbal-rate commands is perfect, the array always remains at a gimbal-angle set that satisfies the constraint function. In practice, the control system that implements the gimbal rates is not perfect. For these practical applications, a low-bandwidth control scheme is required to trim the array's gimbal-angle set to track the gimbal-angle sets specified by the constraint functions. For the purposes of this study, it is assumed that the gimbal rates are perfectly achieved.

The main benefit of the augmented Jacobian method is that if the constraint function enables the performance of the array to be resolved for each angular-momentum state, then the array's performance can be computed analytically for any angular-momentum state, eliminating the need for inexact numerical methods, like Monte Carlo simulations, to determine the performance of the array during operation. The main problem with the augmented Jacobian method is the presence of algorithmic singularities, which occur when the constraint functions result in J_t being singular

[25]. At an algorithmic singularity, the array behaves as if Ω are equal to zero, resulting in the array being unable to produce torque in one or more directions. The main difficulty of developing constraint functions is ensuring that the array does not encounter an algorithmic singularity. Most developed constraint functions are capable of avoiding singularities but have algorithmic singularities within the angular-momentum envelope of the array [10], [11], [18], [19], [25].

The feedback control method eliminates these algorithmic singularities by progressing the array to a constrained gimbal-angle set using feedback control methodologies in the array's null space. One example of using linear feedback control is shown in Eq. (13), where δ_{i_d} is the desired constrained gimbal angle of the i^{th} CMG [10].

$$\begin{bmatrix} \dot{\delta}_1 \\ \dot{\delta}_2 \\ \vdots \\ \dot{\delta}_n \end{bmatrix} = \begin{bmatrix} J \\ N(J) \end{bmatrix}^{-1} \begin{bmatrix} T \\ \overline{h} \\ D \end{bmatrix} \quad (13)$$

$$D = N(J)K \begin{bmatrix} \delta_{1_d} - \delta_1 \\ \delta_{2_d} - \delta_2 \\ \vdots \\ \delta_{n_d} - \delta_n \end{bmatrix}$$

K is a user-selected square gain matrix with n rows. Care needs to be taken when selecting K in practical problems. If the values in K are too large, the gimbal rate limits can be exceeded when the array is simultaneously applying a torque and conditioning itself. If the values in K are too small, the array will not reorient fast enough and may become singular. Monte Carlo simulations for the estimated operation environments can be used to bound K [1], [10].

The feedback control method eliminates algorithmic singularities by enabling the array to deviate from the constrained gimbal-angle set at algorithmic singularities. However, because the

feedback control method results in the array deviating from the constraint configuration, it is difficult to guarantee the performance of the steering law.

2.5.1 Past work

Most work on constraint-based methods have focused on the development of constraint functions. Two research communities have explored developing constraints: roboticists and the CMG community. The robotics community has explored developing constraints for manipulators. Due to the kinematic similarities between CMGs and manipulators, constraints developed for manipulators can be used for CMG arrays, and vice versa. The production of torque for an array of CMGs is analogous to a serial manipulator's production of end-effector velocity.

In the CMG community, constraints have been developed for five different array architectures, as shown in Figure 3: any array with two identical planar CMGs (i.e., both gimbal axes are parallel) [18], any array with three identical planar CMGs [10], a six-CMG roof of identical CMGs [10], a pyramid of four identical CMGs [19], and any array with three orthogonal sets of two identical CMGs [1], [20]. In the robotics community, constraints have been developed for many different manipulator architectures. A general set of constraint functions has been developed for a spherical wrist to enable singularity-free motion as well as maximize output torque of the end-effector [28]. A general circular-backbone constraint has been developed for any planar serial manipulator [29], [30]. The circular-backbone constraint restricts the links of a planar serial manipulator to approximate a circular arc, avoiding all internal singularities. However, unlike the above listed constraints, which use the analytical implementations discussed in Section 2.5, the circular-backbone constraint is not closed-form and requires a numerical solver when implemented,

creating indeterminacy that can result in risk that is unacceptable in high-stakes implementations such as spacecraft.

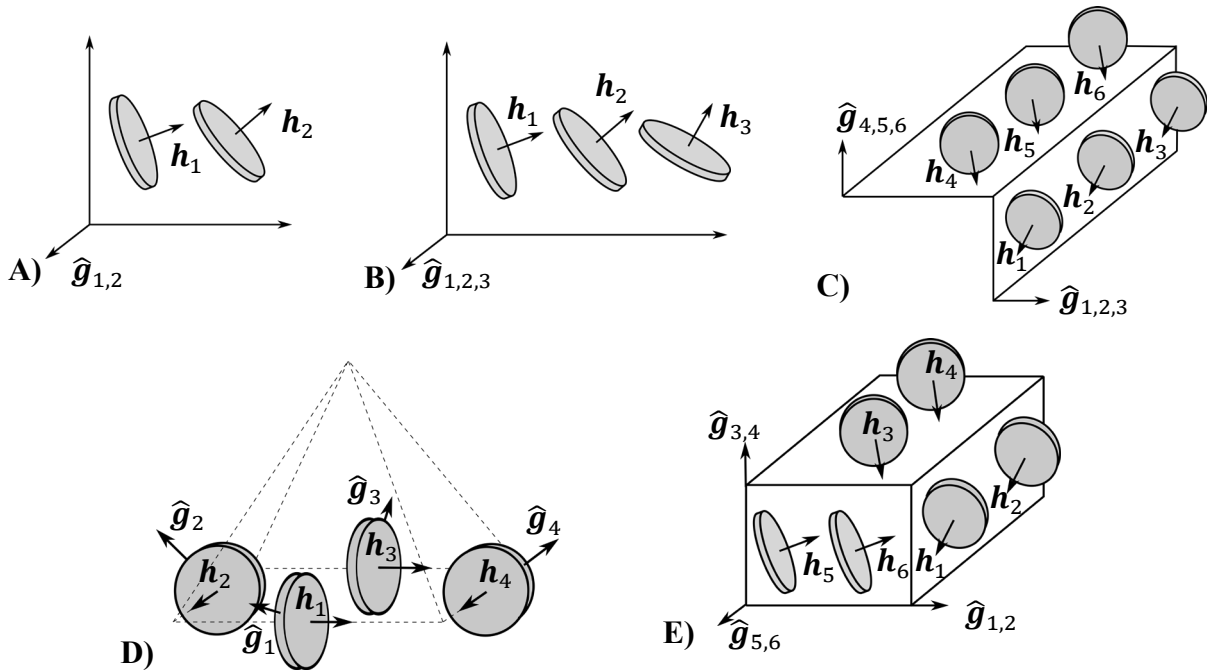


Figure 3. The five arrays for which a known constraint function avoids all singularities: **A)** two planar CMGs, **B)** three planar CMGs, **C)** six-CMG roof array, **D)** a pyramid of four CMGs, and **E)** an array with three orthogonal sets of two CMGs. \hat{g} represents the gimbal axis of each CMG, and h represents an arbitrary angular-momentum direction.

CHAPTER 3 PLANAR ARRAY

The planar array is the simplest architecture, consisting of CMGs whose gimbal axes are all parallel. Past work, discussed in Section 2.5.1, has developed a constraint for the simplest of these arrays, three planar CMGs, which contains the minimum number of CMGs while still remaining redundant. The previously developed circular-backbone constraint enables singularity avoidance for any redundant planar array architectures. However, this constraint is not closed form, complicating the development of performance guarantees and decreasing the predictability of the CB steering law [29], [30].

This chapter improves upon the circular-backbone constraint by providing a general set of closed-form constraints for planar arrays with four or more CMGs that globally maximizes the torque capability. These constraints, in conjunction with previously developed constraint for three planar CMGs, results in a general set of closed-form constraints for any number of redundant planar CMGs. To better understand the performance of the provided constraint functions, for arrays with four, five, six, seven, eight, and nine planar CMGs, the performance of the developed constraint functions is compared to the previously developed, non-closed-form circular-backbone constraint. The performance comparison shows that the provided constraint functions improve torque capability by as much as 35%.

3.1 Torque Capability Optimization

The constraints are developed with the goal of maximizing the torque capability of the array, which is the maximum amount of torque the array can produce in any direction given its mechanical limitations, normalized by the maximum torque magnitude any one CMG can produce.

The general optimization problem to maximize TC for any array, a prescribed U , and a given angular momentum is shown in Eq. (14), where τ is the magnitude of the output torque, τ_x , τ_y , and τ_z are scalars that specify the direction of the torque, $H(\delta_1, \delta_2, \dots, \delta_n)$ is a function that maps the gimbal angles to a matrix representing the array's angular momentum, $\dot{\delta}_{max}$ is the maximum gimbal-rate magnitude a CMG can achieve, and H_d is a matrix representing the desired array angular momentum.

$$\max_{\delta_1, \delta_2, \dots, \delta_n} TC \quad (14)$$

subject to:

$$\left\| J^+ \frac{T}{h} + N(J)^T U \right\|_{\infty} \leq \dot{\delta}_{max} \forall \{\tau_x, \tau_y, \tau_z\} \left\| \begin{bmatrix} \tau_x \\ \tau_y \\ \tau_z \end{bmatrix} \right\|_2 = 1,$$

$$H(\delta_1, \delta_2, \dots, \delta_n) = H_d$$

$$TC = \frac{\tau}{h \dot{\delta}_{max}}$$

$$T = \begin{bmatrix} \tau_x \\ \tau_y \\ \tau_z \end{bmatrix} \tau$$

The optimization assumes that the steering law is known. For a constraint-based steering law, U is dependent on the constraint functions and the implementation method, which greatly complicates the optimization. To simplify the optimization, this chapter assumes that the steering law is a Moore-Penrose pseudoinverse, and thus U is selected to be the zero matrix. The Moore-Penrose pseudoinverse is given close attention in this study because it likely represents a close approximation of most implementations of the constraint functions. In practical applications, it is often desirable to minimize null motion activity for two reasons: excess null motion can result in

greater energy consumption, and large null motions can result in unwanted torque being applied to the body due to torque effects (such as misalignments) that are not modeled by Jacobian. Thus, it is assumed that for most applications U is selected to be a matrix with values that are close to zero, resulting in the Moore-Penrose being a good estimate of these steering laws.

Assuming Moore-Penrose pseudoinverse, TC for any array architecture can be simplified to Eq. (15). A detailed derivation of the simplified metric is provided in Section 7.1.1.

$$TC = \frac{1}{\|W_{MP}\|_\infty} \quad (15)$$

$$W_{MP} = \frac{1}{\det(JJ^T)} \begin{bmatrix} \sqrt{A(1,1)^2 + A(1,2)^2 + A(1,3)^2} \\ \sqrt{A(2,1)^2 + A(2,2)^2 + A(2,3)^2} \\ \vdots \\ \sqrt{A(n,1)^2 + A(n,2)^2 + A(n,3)^2} \end{bmatrix}$$

$$A = J^T \text{adj}(JJ^T)$$

Substituting Eq. (15) into Eq. (14) results in the simplified optimization shown in Eq. (16)

$$\begin{aligned} & \max_{\delta_1, \delta_2, \dots, \delta_n} TC \quad (16) \\ & \text{subject to: } H(\delta_1, \delta_2, \dots, \delta_n) = H_d \end{aligned}$$

The optimization shown in Eq. (16) is further simplified to Eq. (17).

$$\begin{aligned} & \min_{\delta_1, \delta_2, \dots, \delta_n} \|W_{MP}\|_\infty \quad (17) \\ & \text{subject to: } H(\delta_1, \delta_2, \dots, \delta_n) = H_d \end{aligned}$$

A set of gimbal-angle constraint functions that globally optimizes Eq. (17) for all angular-momentum states globally maximizes the array's TC assuming U is equal to zero. These globally optimal constraints can then be implemented using the implementation methodologies discussed

in Section 2.5. The optimization shown in Eq. (17) is difficult to perform analytically for general array architectures. However, for planar array architectures, Eq. (17) can be simplified and analytically maximized.

3.1.1 Planar Array Simplifications

The optimization shown in Eq. (17), for planar arrays, is shown in Eq. (18).

$$\begin{aligned} & \min_{\delta_1, \delta_2, \dots, \delta_n} \|W_{MP}\|_{\infty} & (18) \\ & \text{subject to: } H(\delta_1, \delta_2, \dots, \delta_n) = H_d \\ & W_{MP} = \frac{1}{\det(JJ^T)} \begin{bmatrix} \sqrt{A(1,1)^2 + A(1,2)^2} \\ \sqrt{A(2,1)^2 + A(2,2)^2} \\ \vdots \\ \sqrt{A(n,1)^2 + A(n,2)^2} \end{bmatrix} \end{aligned}$$

The Jacobian of a planar array is shown in Eq. (19). This form can be used for any planar array.

$$J = \begin{bmatrix} -\sin(\delta_1) & -\sin(\delta_2) & \cdots & -\sin(\delta_n) \\ \cos(\delta_1) & \cos(\delta_2) & \cdots & \cos(\delta_n) \end{bmatrix} \quad (19)$$

The planar Jacobian is substituted into the expressions within W_{MP} , yielding simplified expressions shown in Eqs. (20, 21).

$$\sqrt{A(i,1)^2 + A(i,2)^2} = \sqrt{CC^T(CC^T - 2nc_i^2) + n^2c_i^2 + SC^T(SC^T - 2ns_i c_i)} \quad (20)$$

$$\det(JJ^T) = CC^T(n - CC^T) - SC^TSC^T \quad (21)$$

$$C = [c_1 \quad c_2 \quad \cdots \quad c_n]$$

$$S = [s_1 \quad s_2 \quad \cdots \quad s_n]$$

$$c_i = \cos(\delta_i)$$

$$s_i = \sin(\delta_i)$$

3.2 Planar Array Constraints

The gimbal-angle constraint functions provided here globally optimize Eq. (18) for any planar array of CMGs with four or more CMGs. The provided gimbal-angle constraint functions are not unique; the functions represent one set of constraint functions of an infinite number. For the constraint functions, the array's angular momentum is assumed to lie on one axis, $\hat{\mathbf{x}}$ and be positive, so for the remainder of the chapter, unless otherwise stated, H_d is scalar and not a matrix. This simplification does not reduce the generality of the solutions, as the axis can be rotated to achieve any angular momentum in the plane. The gimbal angles are referenced from the $\hat{\mathbf{x}}$ axis. In each gimbal-angle constraint function, the indexing of the CMGs is arbitrary and can be changed as desired. The angular-momentum values denoted with a tilde above the value indicate a normalized angular-momentum value, calculated by dividing the angular-momentum value by h .

Four sets of gimbal-angle constraint functions are provided: gimbal-angle constraint functions for arrays with an even number of CMGs greater than three, gimbal-angle constraint functions for arrays with five CMGs, gimbal-angle constraint functions for arrays with seven CMGs, and gimbal-angle constraint functions for arrays with an odd number of CMGs greater than seven CMGs. Each set of gimbal-angle constraint functions has two solutions, corresponding to two different angular-momentum regions. For each set of gimbal-angle constraint functions, there is continuity of the gimbal angles between the two angular-momentum regions. The angular momentum at which the solution switches is referred to as the critical angular momentum, H_c . H_c for arrays with an even and odd number of CMGs is shown in Eqs. (22, 23), respectively.

$$\tilde{H}_{c\text{even}} = \frac{n}{\sqrt{2}} \quad (22)$$

$$\tilde{H}_{c_{odd}} = 1 + \frac{\sqrt{(n-1)(n-2)}}{2} \quad (23)$$

The angular-momentum region corresponding to angular-momentum states from zero to the critical angular momentum is referred to as the static region. In the static angular-momentum region, the magnitudes of the rows of W_{MP} are all equal to a constant value of $\frac{2}{n}$, and $\det(JJ^T)$ is equal to a constant, global maximum of $\frac{n^2}{4}$. The angular-momentum region corresponding to angular-momentum states equal to or greater than the critical angular momentum is referred to as the declining region. In the declining angular-momentum region, the value of $\det(JJ^T)$ strictly monotonically decreases from the global maximum of $\frac{n^2}{4}$ to zero, as the array approaches saturation, resulting in the rows of W_{MP} tending from $\frac{2}{n}$ towards ∞ in the limit. Figure 4 shows a visual representation of the values of $\|W_{MP}\|_\infty$ with respect to the array's angular momentum for arrays with an even and odd number of CMGs.

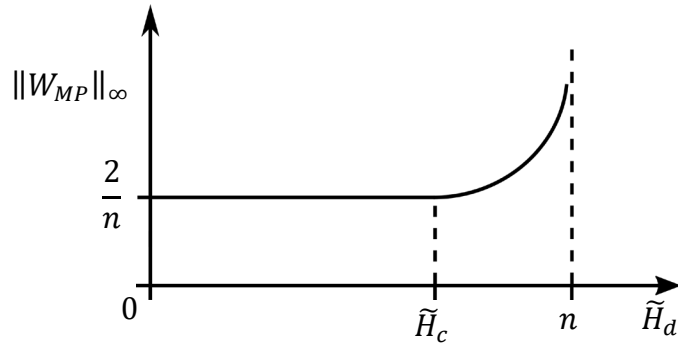


Figure 4. Values of $\|W_{MP}\|_\infty$ with respect to normalized angular momentum.

3.2.1 Arrays with an Even Number of CMGs Greater Than Three

The globally optimal gimbal-angle constraint functions for any array with an even number of CMGs greater than three are shown in Eqs. (24 - 28). In the solutions, $\lceil s \rceil$ denotes the integer that results from rounding s up, $\lfloor s \rfloor$ denotes the integer that results from rounding s down.

$$\delta_{1,2,\dots,k_1} = \begin{cases} \cos^{-1} \left(\frac{\tilde{H}_d}{n} - \frac{\sqrt{k_1(n-2k_1)(-2\tilde{H}_d^2 + n^2)}}{2nk_1} \right), & 0 \leq \tilde{H}_d < \tilde{H}_c \\ \cos^{-1} \left(\frac{\tilde{H}_d}{n} \right), & \tilde{H}_c \leq \tilde{H}_d \leq n \end{cases} \quad (24)$$

$$\delta_{k_1+1,k_1+2,\dots,\frac{n}{2}} = \begin{cases} \cos^{-1} \left(\frac{\tilde{H}_d}{n} + \frac{\sqrt{k_1(n-2k_1)(-2\tilde{H}_d^2 + n^2)}}{n(n-2k_1)} \right), & 0 \leq \tilde{H}_d < \tilde{H}_c \\ \cos^{-1} \left(\frac{\tilde{H}_d}{n} \right), & \tilde{H}_c \leq \tilde{H}_d \leq n \end{cases} \quad (25)$$

$$\delta_{\frac{n}{2}+1,\frac{n}{2}+2,\dots,k_2} = -\delta_{k_1+1,k_1+2,\dots,\frac{n}{2}} \quad (26)$$

$$\delta_{k_2+1,k_2+2,\dots,n} = -\delta_{1,2,\dots,k_1} \quad (27)$$

$$\tilde{H}_c = \frac{n}{\sqrt{2}} \quad (28)$$

$$k_1 = \left\lfloor \frac{n}{4} \right\rfloor$$

$$k_2 = \frac{n}{2} + \left\lceil \frac{n}{4} \right\rceil$$

The resulting array configurations for the static and declining angular-momentum regions are shown in Figure 5. In the static angular-momentum region, the gimbal-angle constraint functions constrain the gimbal angles to four different angles, two of which are the negative of the other two. In the declining angular-momentum region, the gimbal angles are constrained to two different angles that are the negative of one another.

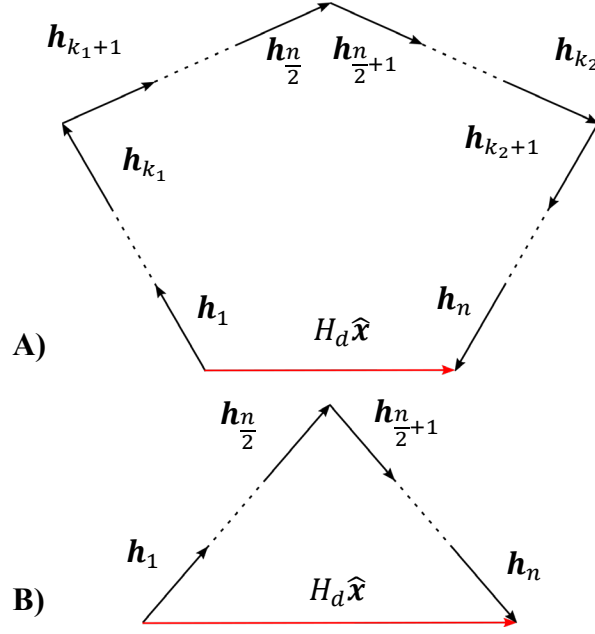


Figure 5. A) represents the constrained array orientation for the static angular-momentum region. B) represents the constrained array orientation for the declining angular-momentum region.

3.2.2 Arrays with Five CMGs

The gimbal-angle constraint functions that globally optimize torque capability for five CMGs are shown in Eqs. (29 - 34).

$$\delta_1 = \begin{cases} \cos^{-1} \left(\frac{\tilde{H}_d - 1}{4} - \frac{\sqrt{-\tilde{H}_d^2 + 2\tilde{H}_d + 5}}{4} \right), & 0 \leq \tilde{H}_d < \tilde{H}_c \\ \cos^{-1} \left(\frac{\tilde{H}_d - 1}{4} \right), & \tilde{H}_c \leq \tilde{H}_d \leq 5 \end{cases} \quad (29)$$

$$\delta_2 = \begin{cases} \cos^{-1} \left(\frac{\tilde{H}_d - 1}{4} + \frac{\sqrt{-\tilde{H}_d^2 + 2\tilde{H}_d + 5}}{4} \right), & 0 \leq \tilde{H}_d < \tilde{H}_c \\ \cos^{-1} \left(\frac{\tilde{H}_d - 1}{4} \right), & \tilde{H}_c \leq \tilde{H}_d \leq 5 \end{cases} \quad (30)$$

$$\delta_3 = 0 \quad (31)$$

$$\delta_4 = -\delta_2 \quad (32)$$

$$\delta_5 = -\delta_1 \quad (33)$$

$$\tilde{H}_c = 1 + \sqrt{6} \quad (34)$$

The resulting constrained array configurations for the static and declining angular-momentum regions are shown in Figure 6. In the declining angular-momentum region, the five gimbal angles are constrained to three different angles, resulting in the trapezoidal shape shown in Fig. (6).

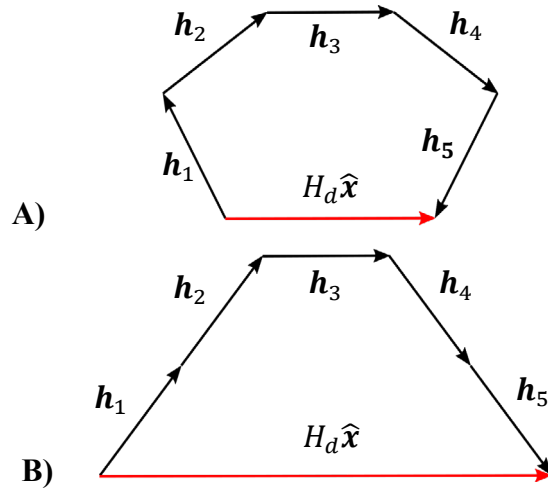


Figure 6. A) represents the constrained array orientation for the static angular-momentum region. B) represents the constrained array orientation for the declining angular-momentum region.

3.2.3 Arrays with Seven CMGs

The gimbal-angle constraint functions that globally optimize torque capability for seven CMGs are shown in Eqs. (35 - 42).

$$\delta_1 = \begin{cases} \cos^{-1} \left(\frac{\tilde{H}_d - 1}{6} - \frac{5\sqrt{-\frac{1}{2}\tilde{H}_d^2 + 7 + \tilde{H}_d}}{6\sqrt{7}} \right), & 0 \leq \tilde{H}_d < \tilde{H}_c \\ \cos^{-1} \left(\frac{\tilde{H}_d - 1}{6} \right), & \tilde{H}_c \leq \tilde{H}_d \leq 7 \end{cases} \quad (35)$$

$$\delta_2 = \begin{cases} \cos^{-1} \left(\frac{\tilde{H}_d - 1}{6} + \frac{\sqrt{-\frac{1}{2}\tilde{H}_d^2 + 7 + \tilde{H}_d}}{6\sqrt{7}} \right), & 0 \leq \tilde{H}_d < \tilde{H}_c \\ \cos^{-1} \left(\frac{\tilde{H}_d - 1}{6} \right), & \tilde{H}_c \leq \tilde{H}_d \leq 7 \end{cases} \quad (36)$$

$$\delta_3 = \begin{cases} \cos^{-1} \left(\frac{\tilde{H}_d - 1}{6} + \frac{2\sqrt{-\frac{1}{2}\tilde{H}_d^2 + 7 + \tilde{H}_d}}{3\sqrt{7}} \right), & 0 \leq \tilde{H}_d < \tilde{H}_c \\ \cos^{-1} \left(\frac{\tilde{H}_d - 1}{6} \right), & \tilde{H}_c \leq \tilde{H}_d \leq 7 \end{cases} \quad (37)$$

$$\delta_4 = 0 \quad (38)$$

$$\delta_5 = -\delta_3 \quad (39)$$

$$\delta_6 = -\delta_2 \quad (40)$$

$$\delta_7 = -\delta_1 \quad (41)$$

$$\tilde{H}_c = 1 + \sqrt{15} \quad (42)$$

The resulting constrained array configurations for the static and declining angular-momentum regions are shown in Figure 7. Similar to the constraints for arrays with five CMGs, in the declining

angular-momentum region, the seven gimbal angles are constrained to three angles, resulting in the trapezoidal shape shown in Figure 7.

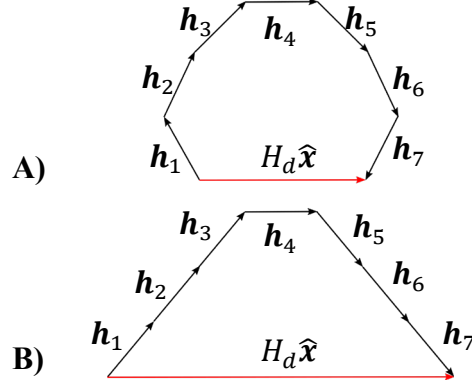


Figure 7. A) represents the constrained array orientation for the static angular-momentum region. B) represents the constrained array orientation for the declining angular-momentum region.

3.2.4 Arrays with an Odd Number of CMGs Greater Than Seven

The globally optimal gimbal-angle constraint functions for any array with an odd number of CMGs greater than seven are shown in Eqs. (43 - 48).

$$\delta_{1,2,\dots,k_1} = \begin{cases} \cos^{-1} \left(\frac{\tilde{H}_d - 1}{n - 1} - \frac{\sqrt{k_1(n - 2k_1 - 1)(-2\tilde{H}_d^2 + 4\tilde{H}_d + n(n - 3))}}{2k_1(n - 1)} \right), & 0 \leq \tilde{H}_d < \tilde{H}_c \\ \cos^{-1} \left(\frac{\tilde{H}_d - 1}{n - 1} \right), & \tilde{H}_c \leq \tilde{H}_d \leq n \end{cases}, \quad (43)$$

$$\delta_{k_1+1, k_1+2, \dots, k_2} = \begin{cases} \cos^{-1} \left(\frac{\tilde{H}_d - 1}{n - 1} + \frac{\sqrt{k_1(n - 2k_1 - 1)(-2\tilde{H}_d^2 + 4\tilde{H}_d + n(n - 3))}}{(n - 1 - 2k_1)(n - 1)} \right), \\ 0 \leq \tilde{H}_d < \tilde{H}_c \\ \cos^{-1} \left(\frac{\tilde{H}_d - 1}{n - 1} \right), \tilde{H}_c \leq \tilde{H}_d \leq n \end{cases} \quad (44)$$

$$\delta_{k_3} = 0 \quad (45)$$

$$\delta_{k_3+1, k_3+2, \dots, k_4} = -\delta_{k_1+1, k_1+2, \dots, k_2} \quad (46)$$

$$\delta_{k_4+1, k_4+2, \dots, n} = -\delta_{1, 2, \dots, k_1} \quad (47)$$

$$\tilde{H}_c = 1 + \sqrt{\frac{(n - 1)(n - 2)}{2}} \quad (48)$$

$$k_1 = \left\lfloor \frac{n - 1}{4} \right\rfloor$$

$$k_2 = \frac{n - 1}{2}$$

$$k_3 = k_2 + 1$$

$$k_4 = k_3 + \left\lfloor \frac{n - 1}{4} \right\rfloor$$

The configurations of the array in both the static and declining angular-momentum regions are shown in Figure 8. In the static angular-momentum region, the gimbal-angle constraints constrain the gimbal angles to five angles, two of which are the negative of the other two, resulting in a similar configuration created by the constraints for five CMGs. In the declining angular-momentum region, the gimbal-angle constraint functions constrain the array to a trapezoidal shape, similarly to the other constraints for arrays with an odd number of CMGs.

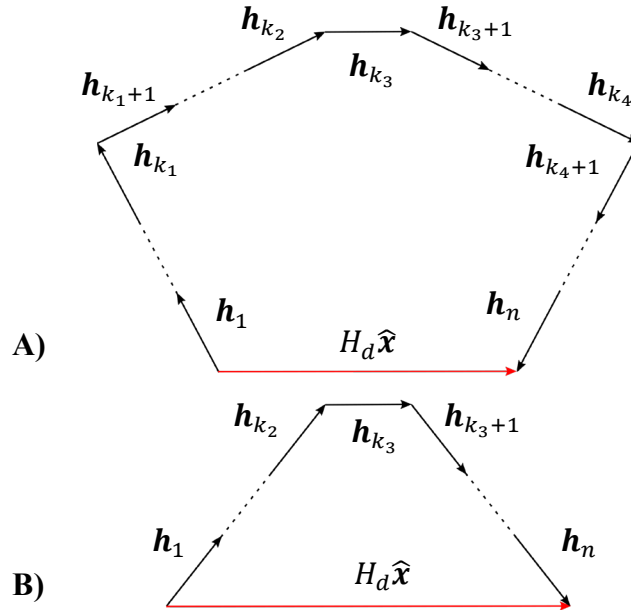


Figure 8. A) represents the constrained array orientation for the static angular-momentum region. B) represents the constrained array orientation for the declining angular-momentum region.

The gimbal-angle constraint functions for seven CMGs in the static region are distinct from the other constraints. Unlike arrays with an odd number of CMGs greater than seven, the array with seven CMGs cannot be constrained to five angles, while still maximizing TC .

An analytical proof is provided in Section 7.2 that verifies the global optimality of the solutions for an even number of CMGs greater than three for any angular-momentum state. For arrays with an odd number of CMGs, a proof of global optimality is provided for the static angular-momentum region. For the declining angular-momentum region, numerical evidence of optimality is provided for planar arrays with five, seven, nine, and eleven CMGs, but optimality is not proven.

3.2.5 Implementation

Similar to all other previously developed planar constraints, the constraint functions provided have algorithmic singularities. One such algorithmic singularity occurs at the zero angular-momentum state. To pass through the zero angular-momentum state, infinite gimbal rate is required to continue to track the constraint, as shown in Figure 9 for three planar CMGs. In Figure 9, at time t_1 , the array produces the angular momentum \mathbf{H}_{t_1} . The array then progresses along $\hat{\mathbf{x}}$ to \mathbf{H}_{t_2} at time t_2 . At the zero-momentum point, the array will need to rotate along the green arrow instantaneously to continue to track the constraint. The same phenomenon occurs for all of the constraints provided in this chapter. To eliminate these algorithmic singularities the feedback control method must be used to implement the constraints. Implementing the constraints using the feedback control method complicates the development of performance guarantees, because it necessarily allows the array to progress away from the constrained orientation.

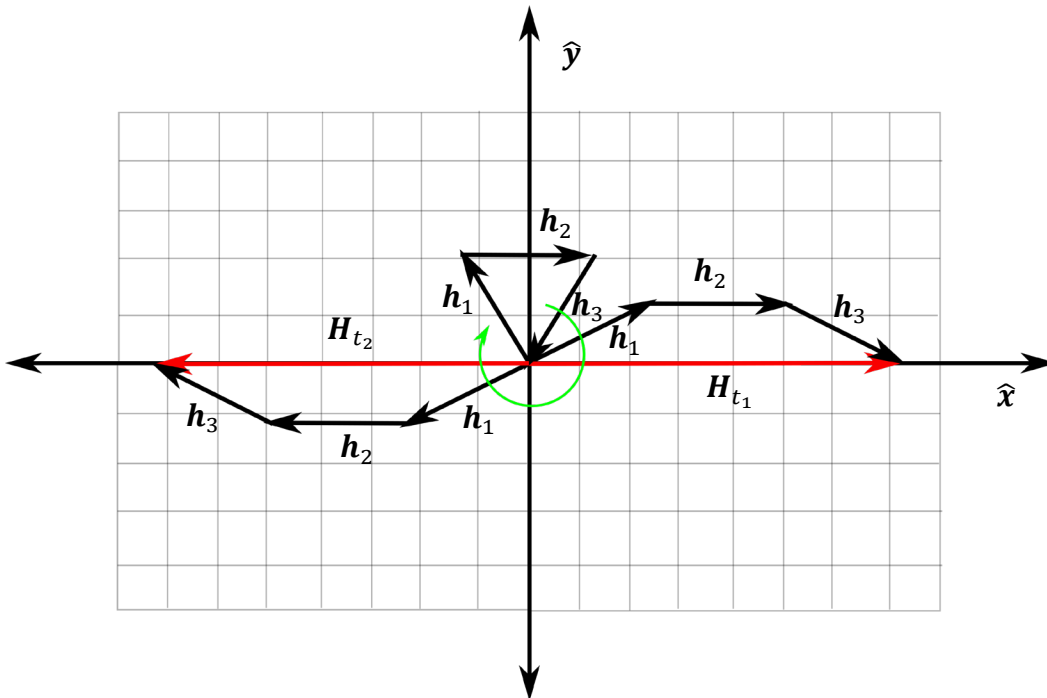


Figure 9. Three CMG algorithmic singularity.

3.3 Comparison

To illustrate the performance of the provided gimbal-angle constraint functions, the provided constraint functions are compared to the circular-backbone constraint [29], [30]. The circular-backbone constraint is not closed-form, complicating a general comparison. Instead, performances for arrays with four, five, six, seven, eight, and nine CMGs are compared. Both constraints have algorithmic singularities. For the comparison, these algorithmic singularities are not considered. Instead, it is assumed the arrays continuously achieve a gimbal-angle set that satisfies the constraint functions.

Unlike the provided constraint functions, the authors do not claim that the circular-backbone constraint optimizes TC . However, the circular-backbone constraint still provides a good reference for comparison because the constraint functions represent the only other set of general constraints for planar arrays. The metric used for comparison is TC shown in Eq. (15).

Figures 10 - 15 show the value of TC versus the normalized angular momentum for the provided gimbal-angle constraint functions as well as the circular-backbone constraint for arrays with four, five, six, seven, eight, and nine planar CMGs. The angular-momentum range shown is from 0 to $0.99n$. The angular momentum of $0.99n$ represents 99% of the saturation limit. Larger angular momentums are not evaluated because at greater angular-momentum states, the arrays are too near a singularity to yield credible results.

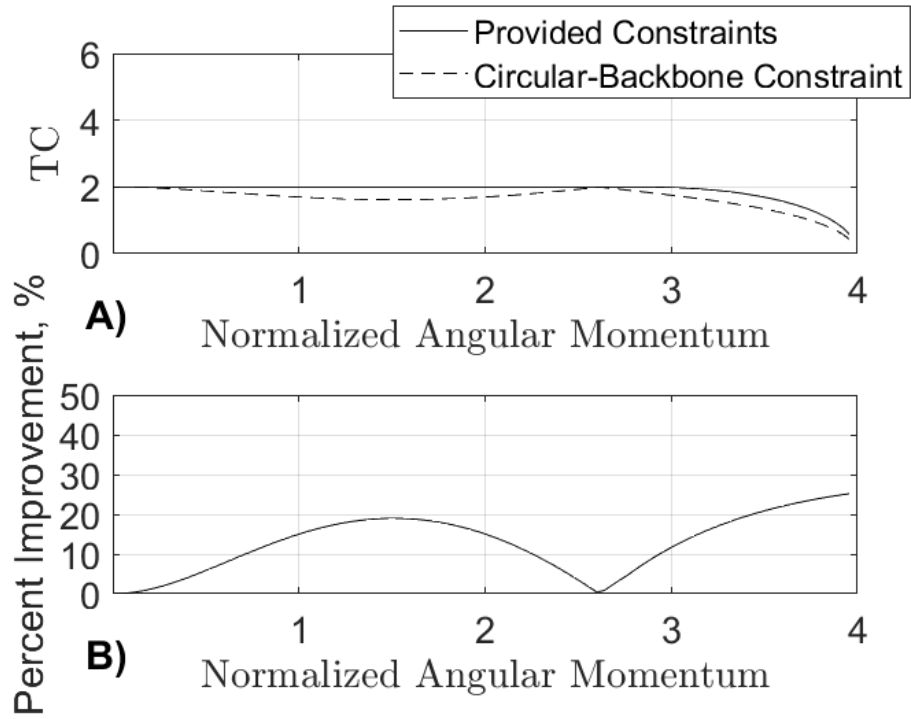


Figure 10. A) represents the values for TC calculated using the provided constraint functions and the circular-backbone constraint for arrays with four CMGs. **B)** represents the percent difference between the value of TC for both constraints.

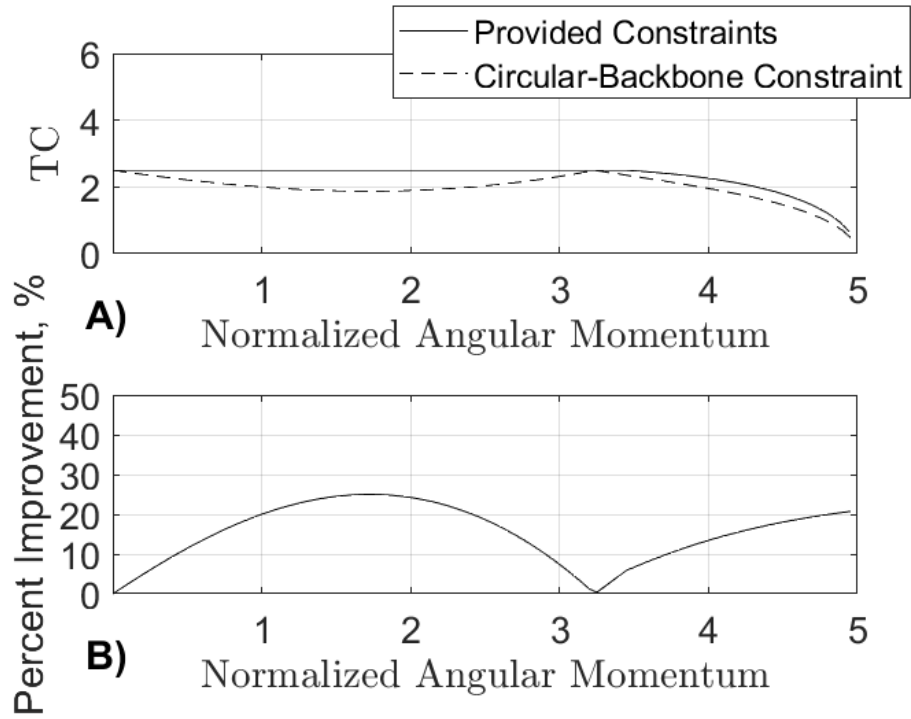


Figure 11. A) represents the values for TC calculated using the provided constraint functions and the circular-backbone constraint for arrays with five CMGs. **B)** represents the percent difference between the value of TC for both constraints.

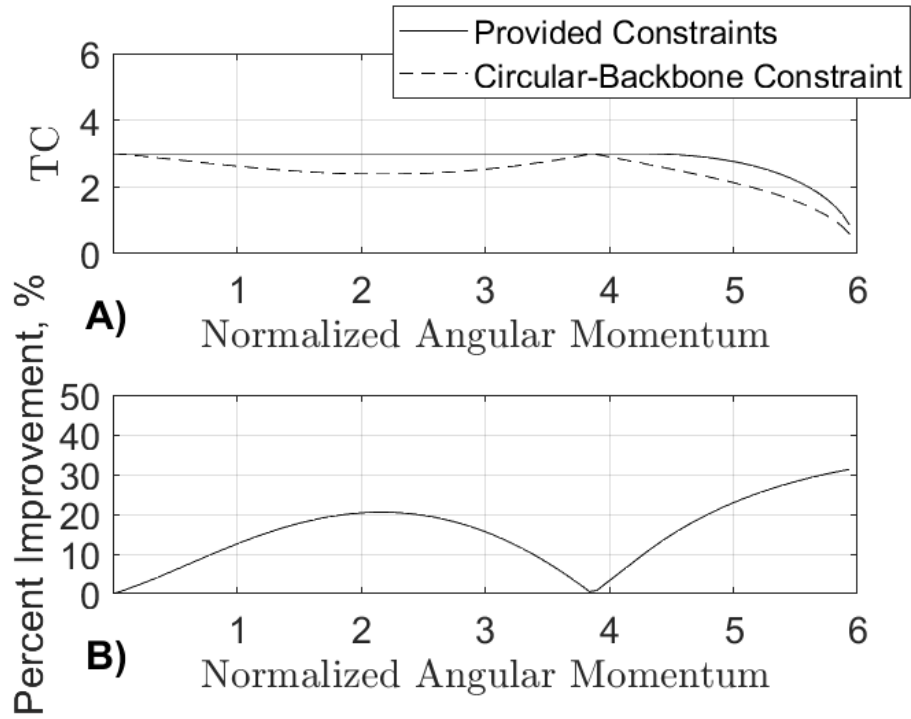


Figure 12. A) represents the values for TC calculated using the provided constraint functions and the circular-backbone constraint for arrays with six CMGs. B) represents the percent difference between the value of TC for both constraints.

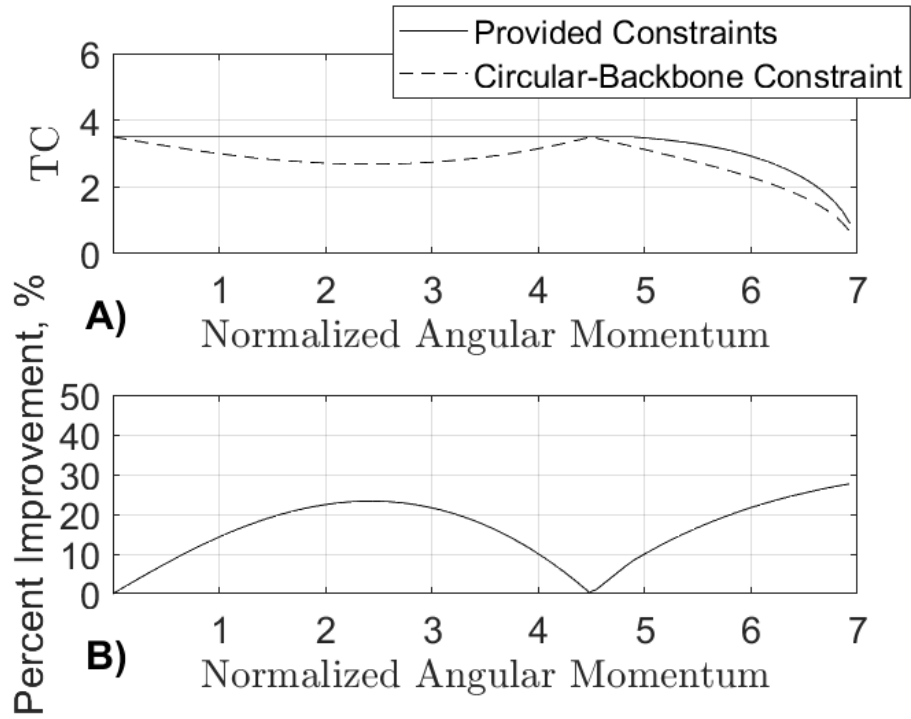


Figure 13. A) represents the values for TC calculated using the provided constraint functions and the circular-backbone constraint for arrays with seven CMGs. **B)** represents the percent difference between the value of TC for both constraints.

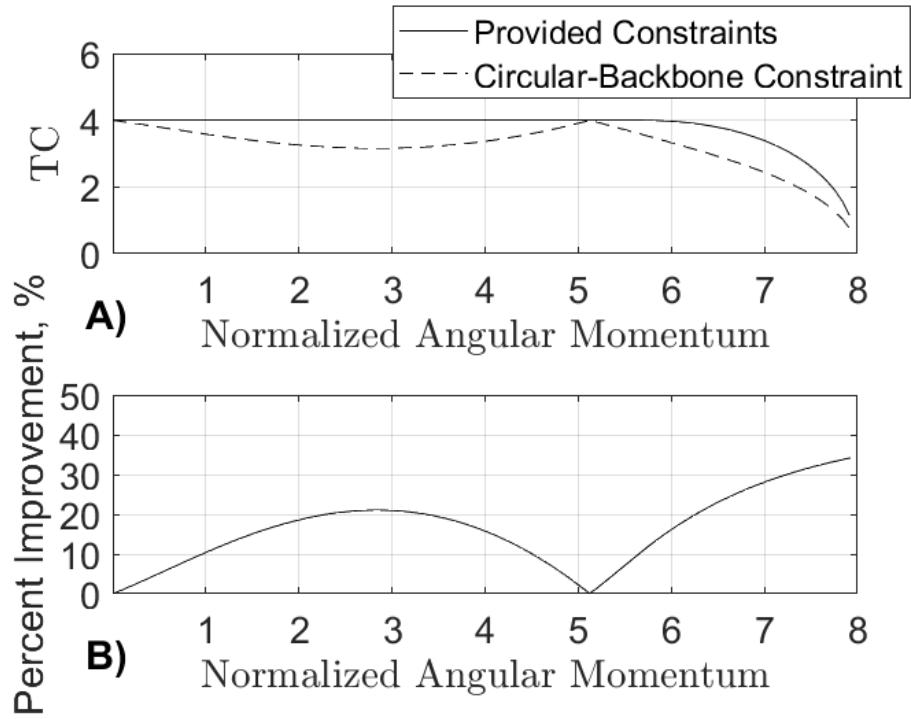


Figure 14. A) represents the values for TC calculated using the provided constraint functions and the circular-backbone constraint for arrays with eight CMGs. B) represents the percent difference between the value of TC for both constraints.

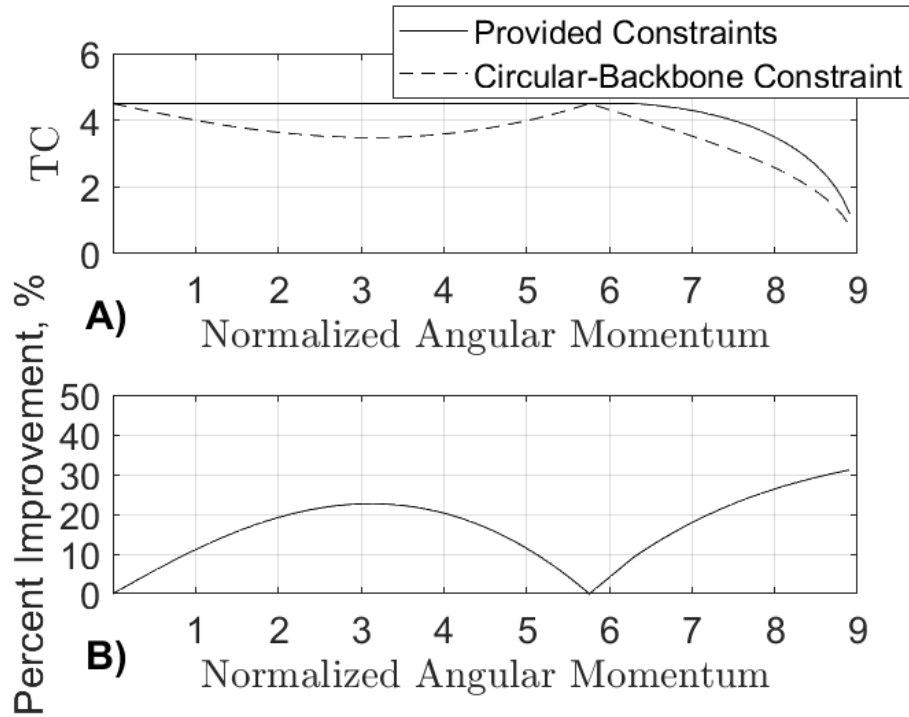


Figure 15. A) represents the values for TC calculated using the provided constraint functions and the circular-backbone constraint for arrays with nine CMGs. B) represents the percent difference between the value of TC for both constraints.

From Figures 10 - 15, the provided gimbal-angle constraint functions achieve a value for TC that is greater than or equal to the value of TC computed with the circular-backbone constraint. Additionally, because the provided constraint functions are closed form, they do not require a numerical solver when implemented, eliminating the risk of numerical instability and reducing the computation required during operation.

Figures 10 - 15 also quantify the percent improvement between the constraints, which is computed by dividing the difference in TC by the provided constraint's TC . The value of TC computed using the circular-backbone constraint is less than that computed using the provided constraint functions, by as much as approximately 25% in the static angular-momentum region

and approximately 35% percent in the declining angular-momentum region. Caution should be exercised when interpreting the percent difference near the saturation of the array because as the array approaches saturation, the numerical error that occurs due to the numerical solver error when implementing the circular-backbone constraint has a large effect on the value of TC . The numerical error in the circular-backbone constraint is less impactful when the array is further from saturation, and therefore offers a more representative comparison.

3.4 Conclusion

The general gimbal-angle constraint functions described here maximize the torque capability for any planar array of CMGs with four or more CMGs. Proofs or numerical evidence of global optimality confirm this fact for each constraint function. A performance comparison between contemporary constraint functions and the provided constraint functions illustrates the greater performance of the provided constraints for arrays with four, five, six, seven, eight, and nine planar CMGs.

The gimbal-angle constraint functions further generalize and improve the performance of constraint-based steering laws. The gimbal-angle constraint functions enable high-performance, fault-tolerant steering laws, because the constraints apply to any number of CMGs greater than four. Thus, if a CMG fails within the array, the steering law can still perform optimally for the remaining CMGs, so long as four or more CMGs remain in the plane. The gimbal-angle constraint functions are applicable to the broader aerospace and robotics fields. For example, due to the kinematic similarities between serial manipulators and CMGs, the solutions maximize the capability of a planar serial manipulator's end effector to track a velocity with joint rate limitations. Maximizing velocity tracking capability of an end effector is beneficial for many applications

where a fast-moving target needs to be tracked. Additionally, due to their generality, the solutions can also be used on hyper-redundant systems, like snake-like robots and elephant trunk robots.

There are three main limitations of these results. First, analytical proofs of optimality have not yet been developed for all angular-momentum states for arrays with an odd number of CMGs greater than three. Instead, numerical evidence of optimality is provided for arrays with five, seven, nine, and eleven CMGs. Second, the TC metric analyzed and maximized is a simplified representation of torque capability, assuming the steering law to be a Moore-Penrose pseudoinverse. Third, because of algorithmic singularities, the constraints must be implemented using the feedback control method. There does not currently exist a general methodology to develop performance guarantees for CB steering laws that use the feedback control method. Thus, performance guarantees are not offered for the provided steering law.

CHAPTER 4 FOUR-CMG BOX-90

The next simplest array architectures are the roof arrays, which consist of two orthogonal planes of CMGs. These arrays also represent one of the most common array architectures used in practice. Specifically, the four-CMG box-90 array, shown in Figure 16, is commonly used in practice because it represents a high-performance array with a minimally redundant suite of actuators and the option of a dormant spare [1], [31]–[33]. Despite the popularity, no current steering law guarantees singularity avoidance for this array while producing the desired torque, thus no steering law can guarantee non-zero torque capability. This chapter expands upon previous CB steering laws and provides a CB steering law for the four-CMG box-90 array that avoids all internal singularities. Additionally, the chapter provides performance guarantees for the steering law, enabling the performance of the array to be computed analytically for any angular-momentum state. This study offers a comparison of the LG steering law and the CB steering law, highlighting the main benefit of CB steering law: performance guarantees.

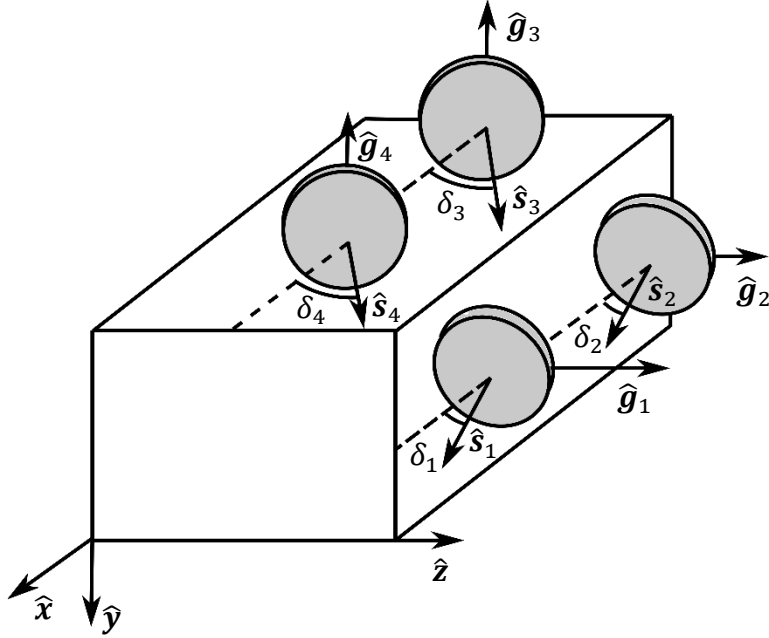


Figure 16. Four-CMG box-90 array. Shows the configuration of the CMGs within a four-CMG box-90 array.

4.1 Box-90 Singularities

Developing a steering law for the four-CMG box-90 array is particularly difficult because of the presence of unavoidable singularities. If a singularity is unavoidable, there does not exist a finite trajectory for U that avoids the singular gimbal-angle set for any finite torque trajectory. Conversely, if a singularity is avoidable, then there exists a finite trajectory for U that enables the array to avoid the singular gimbal-angle set for any possible finite torque trajectory. All external singularities are unavoidable. If the commanded torque progresses the array to saturation, no trajectory for U exists that avoids the external singularity. Internal singularities can be either avoidable or unavoidable [1], [34].

In general, there are two ways to ensure that the array does not reach an unavoidable internal singularity: 1) the array can produce a torque that is not commanded to progress the array away

from the singularity, which is the methodology employed by singularity-robust steering laws; or 2) the array's achievable angular-momentum states, i.e., its angular-momentum envelope, can be restricted, such that the unavoidable angular-momentum states are never encountered. As discussed in Section 2.3, for many practical applications, steering laws that produce a torque other than the commanded torque are not desirable because doing so results in an undesired motion of the body. For example, that motion may disturb a spacecraft's attitude and thereby compromise the performance of an earth-observation payload. The degree to which the array envelope needs to be restricted to ensure that the array does not encounter an unavoidable singularity depends on the array's architecture. Once the angular-momentum envelope is restricted, the extents of the restricted angular-momentum envelope are treated as external saturation singularities and are avoided through proper sizing of the actuators.

The four-CMG box-90 array has both avoidable and unavoidable internal singularities. To clarify the discussion of the singularities, the array is broken into two planes of CMGs. Plane 1, consisting of CMG 1 and 2 as shown in Figure 16, can produce angular momentum in the $\hat{x} - \hat{y}$ plane, but not in the \hat{z} direction. Plane 2, consisting of CMG 3 and 4, as shown in Figure 16, can produce angular momentum in the $\hat{x} - \hat{z}$ plane, but not in the \hat{y} direction. Because \hat{x} is the only common axis of both planes, if the CMGs in the $\hat{x} - \hat{y}$ plane become singular in the \hat{y} direction and/or the CMGs in the $\hat{x} - \hat{z}$ plane become singular in the \hat{z} direction, then the array will be singular.

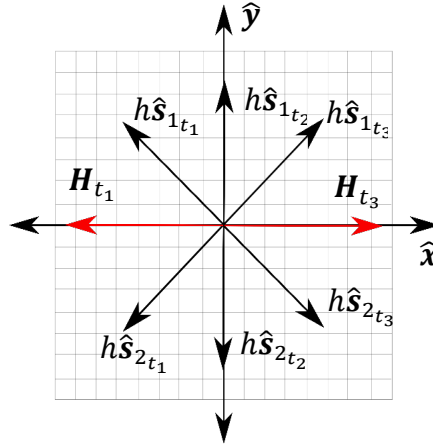


Figure 17. Unavoidable singularities for plane 1.

Unavoidable array-level singularities result from unavoidable singularities for each plane of CMGs. For each plane, angular momentum cannot progress from a positive angular momentum along \hat{x} to a negative angular momentum along \hat{x} , or *vice versa*, without infinite null motion or becoming singular in either the \hat{y} direction for the CMGs in the $\hat{x} - \hat{y}$ plane or the \hat{z} direction for the CMGs in the $\hat{x} - \hat{z}$ plane. For the CMGs in the $\hat{x} - \hat{y}$ plane, the unavoidable singularity is shown in Figure 17, where $\hat{\mathcal{S}}_{i,t_j}$ represents $\hat{\mathcal{S}}$ for the i^{th} CMG at the j^{th} time point and the vector \mathbf{H}_{t_j} represents the total angular momentum of the plane at the j^{th} time point. In Figure 17, the plane of CMGs starts at t_1 producing a negative angular momentum along \hat{x} , which is represented by \mathbf{H}_{t_1} . The array then progresses along \hat{x} to the state at t_3 . To progress from the state at t_1 to the state at t_3 the array must pass through the state at t_2 , assuming finite null motion, resulting in the array becoming singular along \hat{y} . These unavoidable singularities for each plane of CMGs, result in an unavoidable singularity for the entire array anytime a plane of the array must pass through the zero angular-momentum state along \hat{x} .

These unavoidable singularities can be encountered in many different scenarios, such as the one shown in Figure 18. Here, $\mathbf{H}_{i_{t_j}}$ represents the total angular momentum of the i^{th} CMG plane at the j^{th} time point. In Figure 18, at a time t_1 , the array's angular momentum along $\hat{\mathbf{x}}$ exceeds $2h$, and the momentum along $\hat{\mathbf{y}}$ and $\hat{\mathbf{z}}$ is zero. At this angular-momentum state, each plane of CMGs must produce a positive angular momentum along $\hat{\mathbf{x}}$ as shown in Figure 18. If at time t_1 , a continuous torque is commanded in the negative $\hat{\mathbf{x}}$ direction until the array's angular momentum along $\hat{\mathbf{x}}$ is equal to zero, which occurs at time t_2 , then one of the planes must have a negative angular momentum along $\hat{\mathbf{x}}$ (scenario shown in Figure 18), or both planes must produce zero angular momentum. In either scenario, one or both of the planes become singular in the $\hat{\mathbf{y}}$ and/or $\hat{\mathbf{z}}$, resulting in the array becoming singular in those directions. No finite trajectory for U can avoid this singularity.

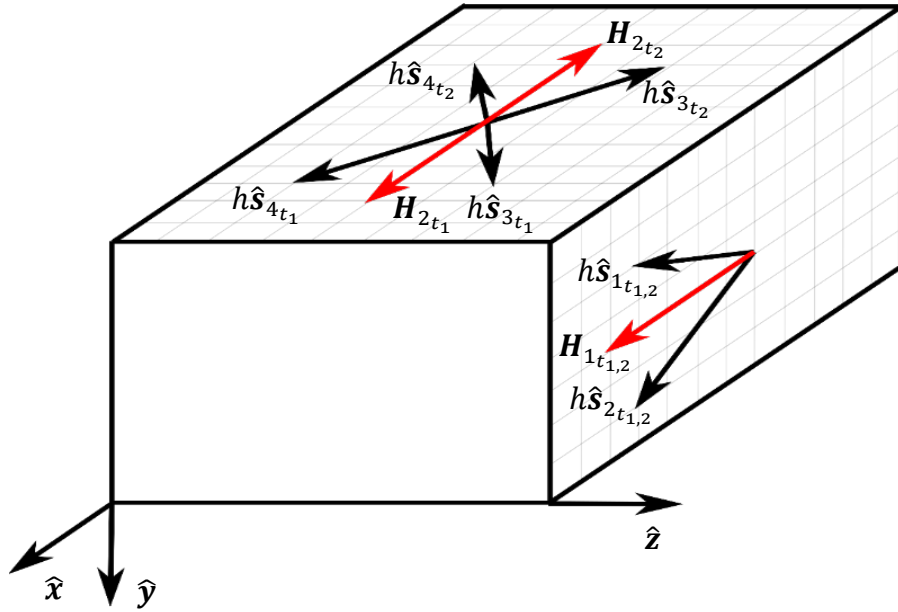


Figure 18. Unavoidable array singularities.

By restricting the angular-momentum envelope to all angular-momentum states that lie within $\pm 2h$ along \hat{x} , shown in Figure 19, all singularities internal to the restricted envelope are avoidable. This chapter provides a CB steering law that guarantees avoidance of the singularities internal to the restricted angular-momentum envelope.

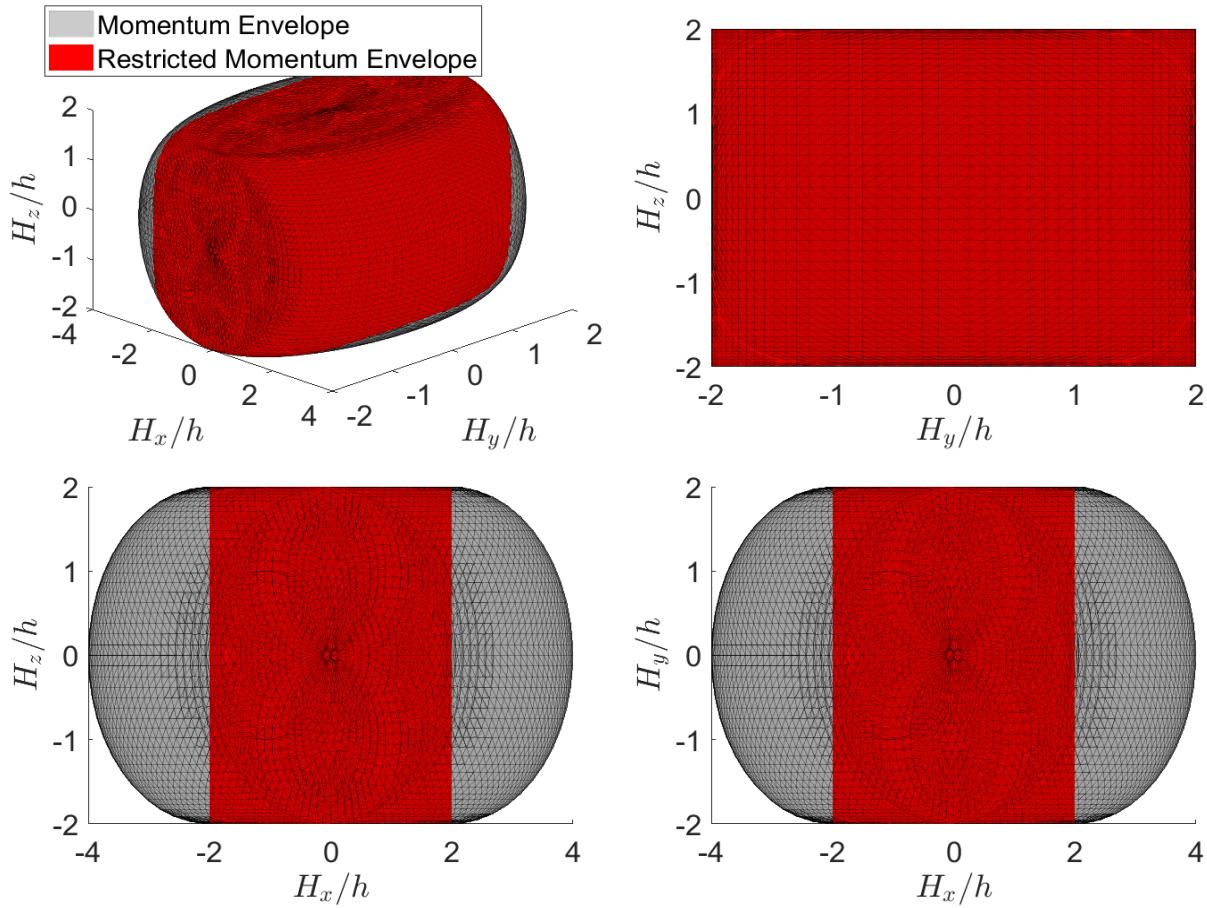


Figure 19. Restricted angular-momentum envelope.

4.2 Box-90 Constraint Function

The goal when developing the constraint function is to maximize TC of the array, thus maximizing the performance of the array. The expression for TC is dependent on the implementation of the constraint. To enable the development of performance guarantees, the

developed constraint is implemented using the augmented Jacobian method. The values of TC for the augmented Jacobian method and the four-CMG box-90 array are shown in Eq. (49), where $J_t^{-1}(i, j)$ represents the value in the i^{th} row and the j^{th} column of J_t^{-1} . A detailed derivation of Eq. (49) is provided in Section 7.1.2.

$$TC = \frac{1}{\|W_{CB}\|_{\infty}} \quad (49)$$

$$W_{CB} = \begin{bmatrix} \sqrt{J_t^{-1}(1,1)^2 + J_t^{-1}(1,2)^2 + J_t^{-1}(1,3)^2} \\ \sqrt{J_t^{-1}(2,1)^2 + J_t^{-1}(2,2)^2 + J_t^{-1}(2,3)^2} \\ \sqrt{J_t^{-1}(3,1)^2 + J_t^{-1}(3,2)^2 + J_t^{-1}(3,3)^2} \\ \sqrt{J_t^{-1}(4,1)^2 + J_t^{-1}(4,2)^2 + J_t^{-1}(4,3)^2} \end{bmatrix}$$

Developing a constraint function that maximizes TC for all angular-momentum states is difficult and may be impossible to achieve with a continuous constraint function. Instead, the goal when developing the constraint function for the four-CMG box-90 is to maximize the minimum TC at each angular-momentum magnitude, which motivates a constraint function that offers uniform capability to respond to torque command trajectories in all directions.

The developed constraint function for the four-CMG box-90 array is shown in Eqs. (50, 51).

$$\tilde{H}_{x_1} - \frac{\tilde{H}_x - \Psi}{2} = 0 \quad (50)$$

$$\Psi = b \left(1 - \left(\frac{\tilde{H}_x}{2} \right)^2 \right) \left(1 - \left(\frac{\tilde{H}_y}{2} \right)^2 \right) \left(1 - \left(\frac{\tilde{H}_z}{2} \right)^2 \right) + P(\tilde{H}_x) \quad (51)$$

$$P(\tilde{H}_x) = -\frac{67}{3840} \tilde{H}_x^8 + \frac{1}{6} \tilde{H}_x^6 - \frac{11}{24} \tilde{H}_x^4 + \frac{47}{60} \tilde{H}_x^2$$

$$\tilde{H}_x = \cos(\delta_1) + \cos(\delta_2) + \cos(\delta_3) + \cos(\delta_4)$$

$$\tilde{H}_{x_1} = \cos(\delta_1) + \cos(\delta_2)$$

$$\tilde{H}_y = \sin(\delta_1) + \sin(\delta_2)$$

$$\tilde{H}_z = \sin(\delta_3) + \sin(\delta_4)$$

$$b = \frac{4\sqrt{6}}{3}$$

The formulation of the constraint function is based on the principle that $\hat{\mathbf{x}}$ is the shared axis for both planes of CMGs. Thus, the angular momentum along $\hat{\mathbf{x}}$ for each plane of CMGs can be biased against each other, enabling the gimbal-angle set to be changed without changing the angular momentum of the array. The amount each plane is biased against one another is dictated by Ψ .

The possible formulations of Ψ are restricted to only those that enable the array to reach the extents of the restricted angular-momentum envelope along $\hat{\mathbf{x}}$, $\hat{\mathbf{y}}$ and $\hat{\mathbf{z}}$, which motivates constraint functions whose constrained angular-momentum envelope is maximized. For the array to be capable of reaching the extents of the angular-momentum envelope along $\hat{\mathbf{x}}$, $\hat{\mathbf{y}}$ and $\hat{\mathbf{z}}$, Ψ must achieve the values shown in Eqs. (52 - 54).

$$\tilde{H}_x = 0, \tilde{H}_y = \pm 2, \tilde{H}_z = 0, \Psi = 0 \quad (52)$$

$$\tilde{H}_x = 0, \tilde{H}_y = 0, \tilde{H}_z = \pm 2, \Psi = 0 \quad (53)$$

$$\tilde{H}_x = \pm 2, \tilde{H}_y = 0, \tilde{H}_z = 0, \Psi = \pm 2 \quad (54)$$

The formulation of Ψ in Eq. (51) has two main parts: a cubic constraint function and a univariate polynomial in \tilde{H}_x . The cubic constraint function satisfies Eqs. (52, 53) and results in the greatest performance of the evaluated constraint function formulations. Equations (55 - 58)

show four other constraint function formulations that perform less well, but all of which satisfy Eqs. (52, 53). Here, s and c are tuning constants.

$$\left(1 - \left(\frac{\tilde{H}_x}{c}\right)^2 - \left(\frac{\tilde{H}_y}{2}\right)^2 - \left(\frac{\tilde{H}_z}{2}\right)^2\right)^s \quad (55)$$

$$\left(1 - \left(\frac{\tilde{H}_y}{2}\right)^2 - \left(\frac{\tilde{H}_z}{2}\right)^2\right)^s \quad (56)$$

$$\left(\left(1 - \left(\frac{\tilde{H}_y}{2}\right)^2\right)\left(1 - \left(\frac{\tilde{H}_z}{2}\right)^2\right)\right)^s \quad (57)$$

$$\left(\left(1 - \left(\frac{\tilde{H}_x}{c}\right)^2\right)\left(1 - \left(\frac{\tilde{H}_y}{2}\right)^2\right)\left(1 - \left(\frac{\tilde{H}_z}{2}\right)^2\right)\right)^s \quad (58)$$

The spherical constraint function, shown in Eq. (55), offers marginally greater minimum TC at most angular-momentum magnitudes than does the cubic constraint function. However, the spherical constraint function's constrained angular-momentum envelope is considerably smaller than that of the cubic constraint function. In Section 7.3, a spherical constraint function is offered along with plots of its performance. The scalar b is selected to optimize TC at the zero angular-momentum state, at which point Ψ is equal to b .

A polynomial is added to the cubic constraint function. The polynomial is formulated such that Ψ satisfies Eq. (54). Infinitely many polynomial formulations also satisfy Eq. (54). The polynomial's coefficients and order are numerically tuned to provide the greatest minimum TC at all angular-momentum states.

4.3 Steering Law Performance

The performance of the constraint implemented with the augmented Jacobian method is evaluated at evenly distributed angular-momentum grid points within the restricted angular-momentum envelope. The discretization for the grid is $0.007 \frac{Nms}{h}$. At each grid point, the gimbal-angle sets that satisfy each angular-momentum state are computed analytically. There are multiple gimbal-angle set solutions for each angular-momentum state, because the gimbal-angle solution for a CMG within a plane can be applied to the other CMG within that plane. However, the multiple solutions at each angular-momentum state result in the same value for TC .

Figure 20A shows TC vs. the normalized angular-momentum magnitude of the array, where H represents the angular-momentum magnitude of the array. For a single value of the angular-momentum magnitude, the values of TC represent all possible TC values that would occur at that angular-momentum magnitude. The lower edge of the black band represents the minimum TC that is guaranteed at a given array angular-momentum magnitude. Figure 20B shows TC at slices of angular momentum where one of \tilde{H}_x , \tilde{H}_y or \tilde{H}_z are equal to zero. Figure 21 shows the torque zones for the CB steering law, where δ_{max} represents the maximum gimbal rate of the CMGs in the array. For a specified torque magnitude, τ , along the y axis, the green zone represents angular-momentum magnitudes that enable the specified torque magnitude to be producible in all torque directions for any angular-momentum direction. Thus, for a specified torque magnitude, the right edge of the green zone represents the radius of the largest angular-momentum sphere, within which the array is capable of producing the specified torque magnitude in all torque directions at all angular-momentum states. The black zone represents the angular-momentum magnitudes, where a specified torque magnitude can be produced in all torque directions, but not in all angular-

momentum directions. For certain angular-momentum directions, the array is capable of producing the specified torque magnitude in all torque directions at greater angular-momentum magnitudes. The greatest angular-momentum magnitude at which the array can still produce the specified torque magnitude in all torque directions, is represented by the right most edge of the black zone. The red zone represents angular-momentum magnitudes at which the specified torque is not guaranteed to be producible in all torque directions. However, the torque magnitude may be producible in some torque directions.

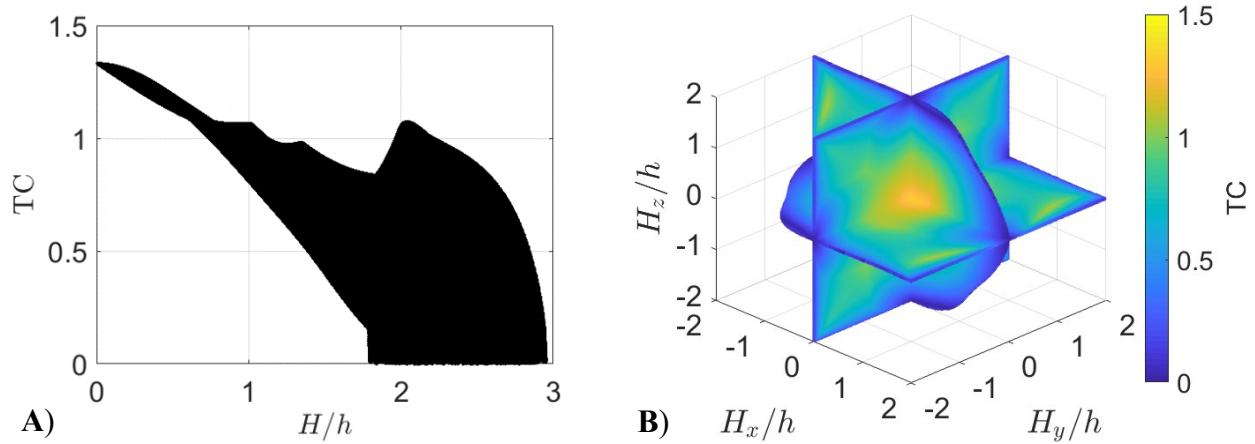


Figure 20. Torque capability of the array within the constrained angular-momentum envelope.

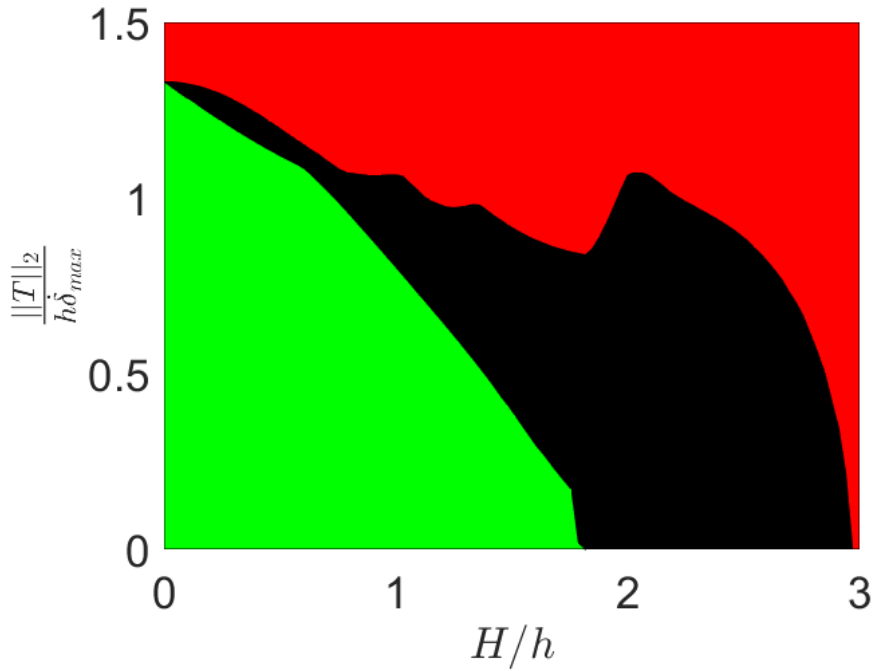


Figure 21. Producibile torque zones.

Figure 22 shows the constrained angular-momentum envelope. From Figure 22, the constrained angular-momentum envelope is nearly the same size as the restricted angular-momentum envelope. However, algorithmic singularities prevent the array from accessing the whole restricted angular-momentum envelope. The minimum angular-momentum magnitude that lies on the constrained angular-momentum envelope boundary is 1.79, which represents the radius of the largest sphere, centered on the origin, that can be inscribed within the constrained angular-momentum envelope.

Figure 23 shows the angular-momentum boundary for when TC is equal to 0.5 compared to the restricted angular-momentum envelope. All angular-momentum states within the volume have a TC of at least 0.5. Thus, all angular-momentum states that are within the volume can produce a torque of a magnitude of at least $0.5h\delta_{max}$. From Figure 23 the array has a TC of at least 0.5 for

most of the restricted angular-momentum envelope. The minimum angular-momentum magnitude that lies on the angular-momentum boundary for a TC of 0.5 is 1.39.

Figure 24 shows the angular-momentum bounds for a TC of 1 compared to the restricted angular-momentum envelope. All angular-momentum states within the volume have a TC greater than 1. Thus, all angular-momentum states within the volume can produce a torque of a magnitude of at least $h\dot{\delta}_{max}$. From Figure 24, most angular-momentum states that have a TC of at least 1 are centered around the zero angular-momentum states. There are small clusters of angular-momentum states that have a TC of at least 1. These small clusters are represented by the small lobe of torque capability centered at an angular-momentum magnitude of approximately 2, shown in Figure 20A. The minimum angular magnitude that lies on the angular-momentum boundary for a TC of 1 is 0.73.

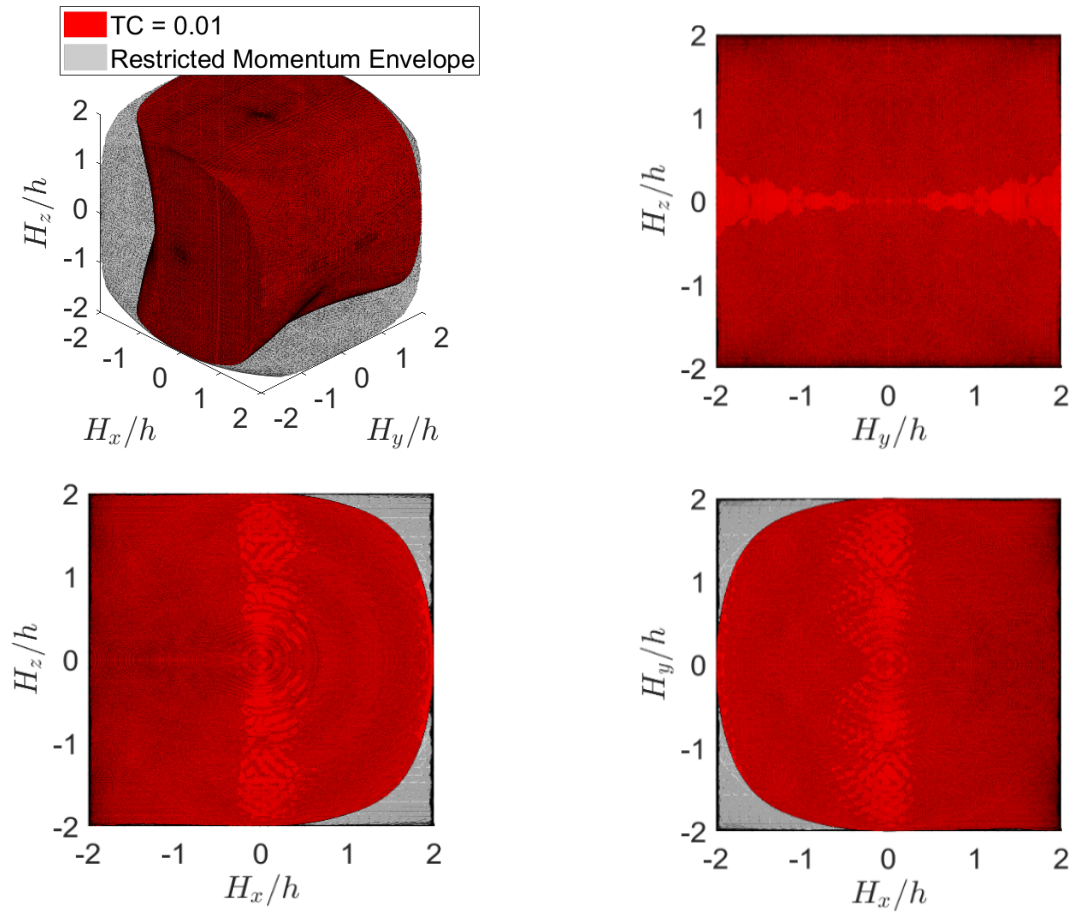


Figure 22. Constrained angular-momentum envelope.

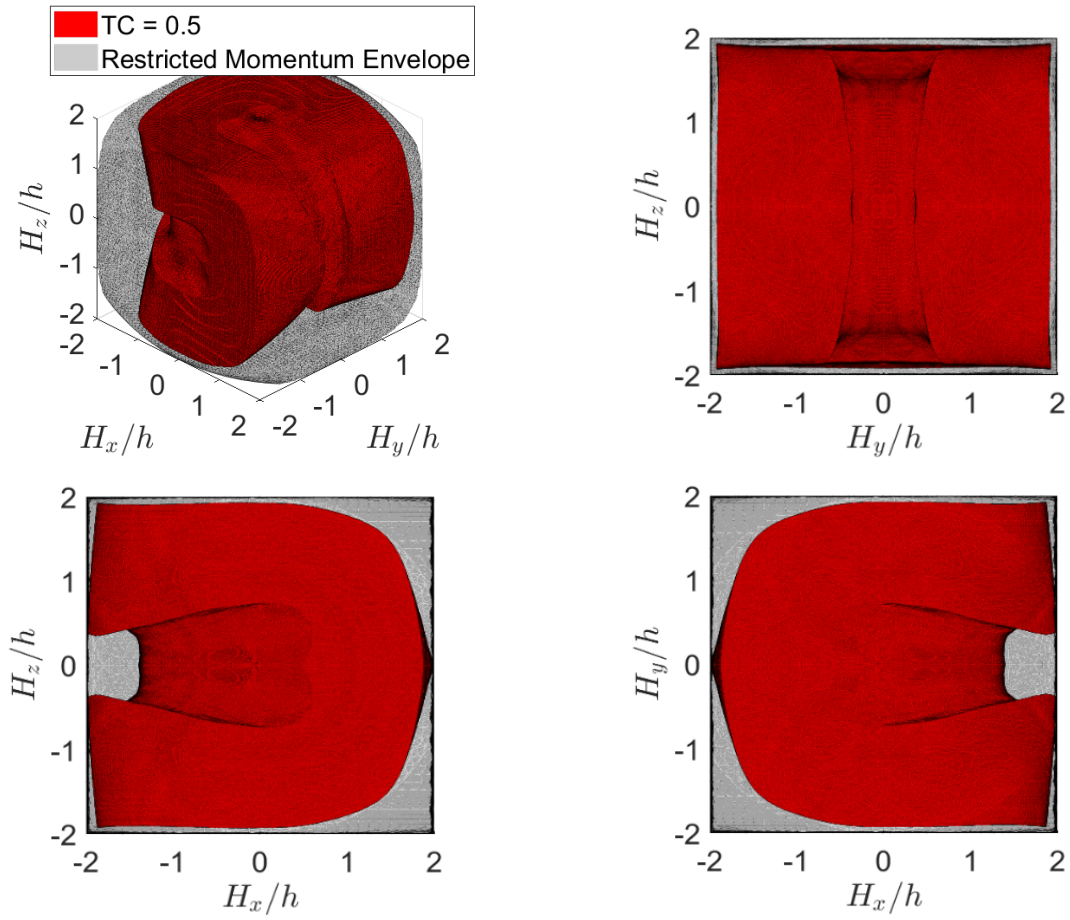


Figure 23. Angular-momentum boundary for when TC is equal to 0.5.

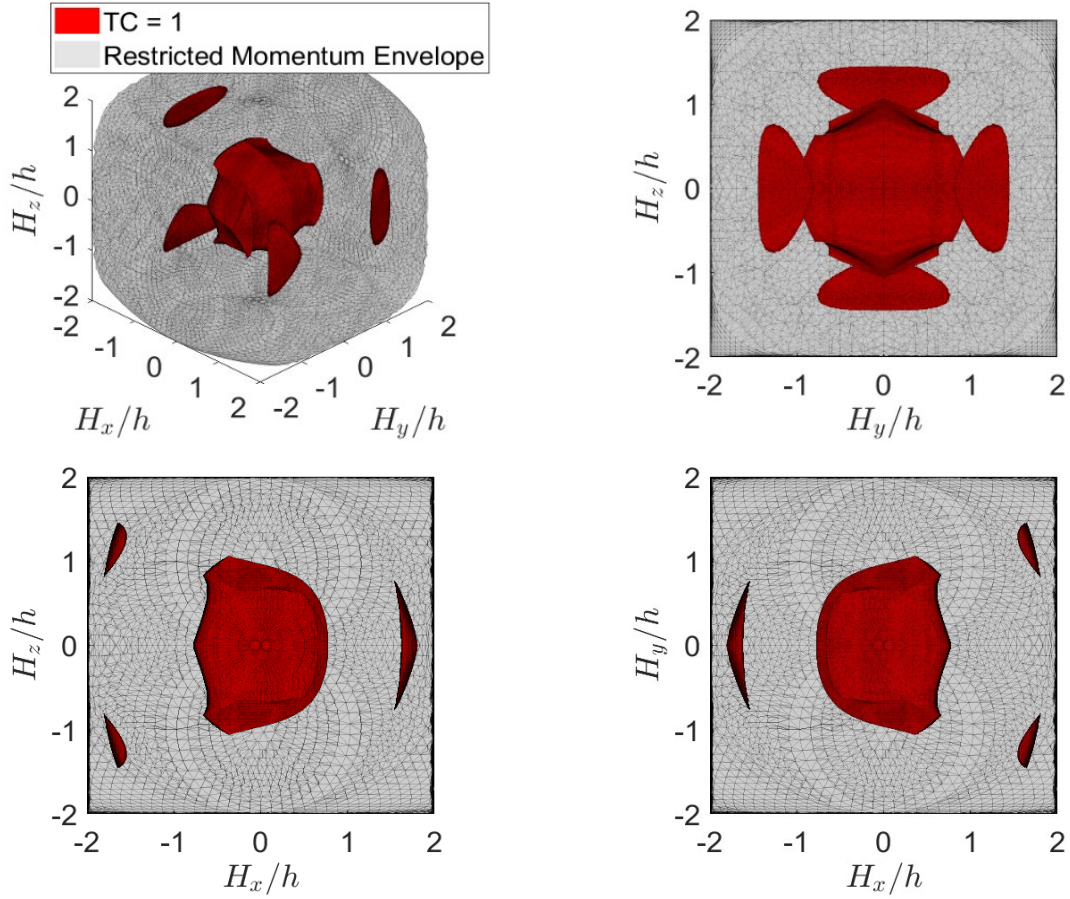


Figure 24. Angular-momentum boundary for when TC is equal to 1.

4.4 Performance Comparison

The performance of the provided steering law is compared to that of the LG steering law. The LG steering law is commonly often considered in the literature [1], [16]. The LG steering law uses the null space of the array to progress the array to a gimbal-angle set that maximizes a cost function. A common cost function, which is the one used for this comparison, is Ω [1]. The LG steering law is shown in Eq. (59), where k is a tunable scalar gain.

$$\begin{bmatrix} \dot{\delta}_1 \\ \dot{\delta}_2 \\ \dot{\delta}_3 \\ \dot{\delta}_4 \end{bmatrix} = J^+T + \dot{\Delta}_n \quad (59)$$

$$\dot{\Delta}_n = k(I_{4 \times 4} - J^+J)d^T$$

$$d = \begin{bmatrix} \frac{\partial \Omega}{\partial \delta_1} & \frac{\partial \Omega}{\partial \delta_2} & \frac{\partial \Omega}{\partial \delta_3} & \frac{\partial \Omega}{\partial \delta_4} \end{bmatrix}$$

The column matrix $\dot{\Delta}_n$ represent the null motion of the array used to avoid singularities. The gain, k , is application dependent. Care needs to be taken when selecting k for practical applications. If k is too large, the gimbal rate limits of the CMG array can be exceeded when the array is simultaneously applying a torque and progressing to a gimbal-angle set that maximizes a cost function. If k is too small, the array cannot progress fast enough to a gimbal-angle set that maximizes the cost function and may become singular. Monte Carlo simulations are often used to determine which values of k enable the greatest performance for a particular application [1]. This analysis considers k values of 0.2, 0.4, 0.6, 0.8, and 1.

TC is the metric used to compare the steering laws. TC for the LG steering law and the four-CMG box-90 array is shown in Eq. (60).

$$TC = \min \left(\begin{array}{c} \frac{1 - \frac{1}{\delta_{\max}} |\dot{\Delta}_n(1, 1)|}{\sqrt{J^+(1,1)^2 + J^+(1,2)^2 + J^+(1,3)^2}} \\ \frac{1 - \frac{1}{\delta_{\max}} |\dot{\Delta}_n(2, 1)|}{\sqrt{J^+(2,1)^2 + J^+(2,2)^2 + J^+(2,3)^2}} \\ \frac{1 - \frac{1}{\delta_{\max}} |\dot{\Delta}_n(3, 1)|}{\sqrt{J^+(3,1)^2 + J^+(3,2)^2 + J^+(3,3)^2}} \\ \frac{1 - \frac{1}{\delta_{\max}} |\dot{\Delta}_n(4, 1)|}{\sqrt{J^+(4,1)^2 + J^+(4,2)^2 + J^+(4,3)^2}} \end{array} \right) \quad (60)$$

A derivation of TC for the LG steering law is provided in Section 7.1.3. TC for the LG steering law depends on the maximum gimbal rate of the CMGs within the array. For this comparison, the maximum gimbal rate is chosen to be 1 rad/s, which represents a common maximum gimbal rate for practical applications. The maximum gimbal-rate is only used for normalization and is not applied to the array during operation.

4.4.1 Methodology

Unlike the CB steering law provided, the performance of the LG steering law cannot be computed for a given angular momentum *a priori*, requiring an iterative simulation to evaluate its performance. The same simulation is used to validate the performance of the provide CB steering law. The simulation has two main parts. The first part computes TC for each steering law at each steering law's current gimbal-angle set. The second part propagates the gimbal-angles forward in time using Eqs. (61, 62), where Δ_{LG_t} and Δ_{CB_t} represent the gimbal-angle sets of the LG steering law and the CB steering law, respectively at time t , and $\dot{\Delta}_{LG_t}$ and $\dot{\Delta}_{CB_t}$ represent the gimbal-rate sets of the LG steering law and the CB steering law, respectively at time t , and dt is 0.001 s.

$$\Delta_{LG_{t+1}} = \Delta_{LG_t} + \dot{\Delta}_{LG_t} dt \quad (61)$$

$$\Delta_{CB_{t+1}} = \Delta_{CB_t} + \dot{\Delta}_{CB_t} dt \quad (62)$$

The two parts of the simulation are run during each iteration of simulation. The performance of each steering law depends in the initial gimbal-angle set for each steering law and the commanded torque at each iteration.

The performance of both steering laws is evaluated while tracking 50 different angular-momentum trajectories, which dictate the initial gimbal-angle set and the torque command at each iteration of the simulation. Each angular-momentum trajectory consists of four angular-momentum waypoints. The first and starting waypoint is selected as the zero angular-momentum state for the array. There is an infinite number of starting gimbal-angle sets that achieve zero angular momentum. For the comparison, the initial gimbal-angle set for both arrays is shown in Eqs. (63 - 66), which satisfies the constraint function.

$$\delta_1 = \cos^{-1}\left(-\frac{b}{4}\right) \quad (63)$$

$$\delta_2 = -\delta_1 \quad (64)$$

$$\delta_3 = \cos^{-1}\left(\frac{b}{4}\right) \quad (65)$$

$$\delta_4 = -\delta_3 \quad (66)$$

The gimbal-angle sets of the steering laws are not defined at any other angular-momentum state. Instead the gimbal-angle sets of each steering law are dictated by Eqs. (61, 62).

The second and third waypoints of the angular-momentum trajectory are randomly selected from a uniform distribution of angular-momentum states that lie within the constrained angular-

momentum envelope. The fourth waypoint is again the zero angular-momentum state. Once the steering laws reach the fourth waypoint of a trajectory, the gimbal-angle sets for both steering laws are set to the initial gimbal-angle sets of the next trajectory.

The path that each steering law takes to get from one angular-momentum waypoint to the next is dictated by the torque command at each iteration. At each iteration, the direction of the torque is selected to progress the array in a straight line to the next angular-momentum waypoint. The magnitude of the torque command at each iteration is randomly selected from a uniform distribution ranging from 0 to $h \frac{1}{s}$. For each gain, k , the torque commanded at each iteration is the same. All 50 randomly selected angular-momentum trajectories are shown in Figure 25.

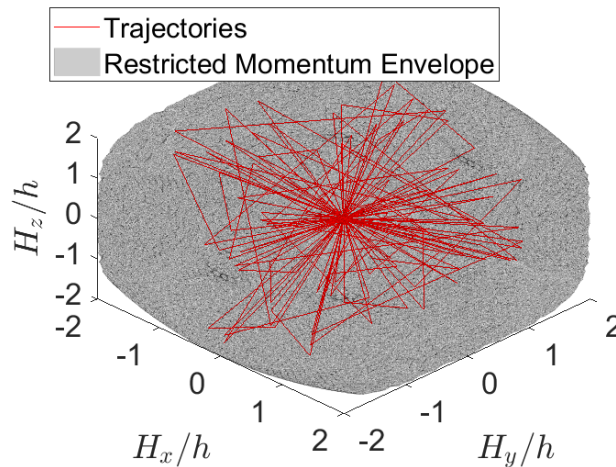


Figure 25. Angular-momentum trajectories.

4.4.2 Results

Figure 26 shows the TC for the CB steering law for all 50 trajectories and predicted TC for the CB steering law for all reachable angular-momentum states. From Figure 26, the array always

remains within the predicted TC of the array, which supports the analytically computed performance results discussed in Section 4.3.

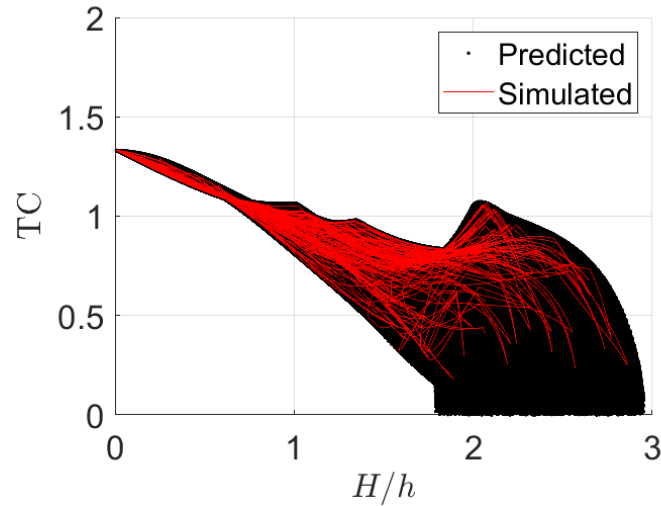


Figure 26. CB steering law's TC for all 50 trajectories.

Figure 27 shows the TC of LG steering law for all angular-momentum trajectories for each tested gain. Figure 27 also shows the predicted TC for the CB steering law for all angular-momentum states. From Figure 27 the LG steering law achieves greater TC than is possible for the CB steering law at some angular-momentum magnitudes. Figure 27 also shows that at some angular-momentum magnitudes, TC for the LG steering law is near zero or negative.

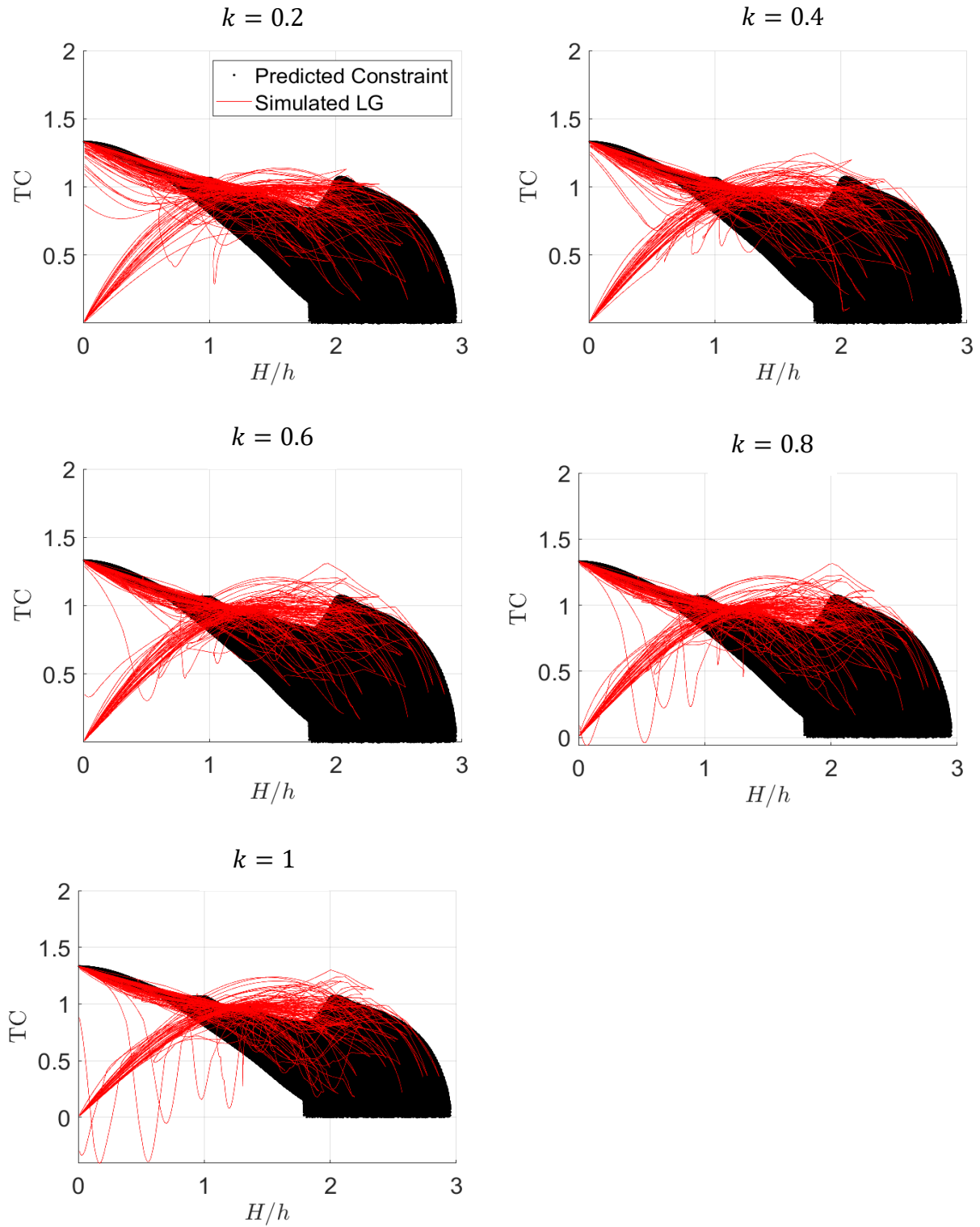


Figure 27. LG steering law's TC for all 50 trajectories.

There are two reasons that the TC may be near zero or negative. First, the magnitudes of the gimbal rates progressing the array to a gimbal-angle set, $\dot{\Delta}_n$, which maximizes Ω , are too large. If the gimbal rates that progress the array to a gimbal-angle set are too large, resulting in $\|\dot{\Delta}_n\|_\infty$ being greater than or equal to the maximum gimbal rate, the numerator of Eq. (60) is less than or equal to zero, resulting in TC being less than or equal to zero. $\|\dot{\Delta}_n\|_\infty$ is reduced by reducing the gain k . There always exists a value of k that results in $\|\dot{\Delta}_n\|_\infty$ being less than the maximum gimbal rate. Thus, through proper selection of k , the value of $\|\dot{\Delta}_n\|_\infty$ can be guaranteed to remain less than or equal to the maximum gimbal rate for any angular-momentum state. Second, the steering law's proximity to a singularity can also cause TC to be near zero. If the steering law is singular, the denominator of Eq. (60) is infinite, resulting in TC being zero. Determining how k should be modified to guarantee the array does not become singular is difficult and currently no general method exists for doing so.

To determine why the TC values are near zero, whether it is due to the array becoming singular or $\|\dot{\Delta}_n\|_\infty$ being too large, Ω is plotted with respect to the normalized angular-momentum magnitude of the array for all 50 trajectories for each tested gain, as shown in Figure 28. Ω is not dependent on $\|\dot{\Delta}_n\|_\infty$. If the value of Ω is near zero, the array is near a singularity. Figure 28 also shows the determinant of J_t for all reachable angular-momentum states. From Figure 28, the LG steering law does become singular at the origin for many of the trajectories. None of the gains tested result in the array remaining non-singular for all of the trajectories. The same is not true for the CB steering law, which remains non-singular for all angular-momentum states within the constrained angular-momentum envelope.

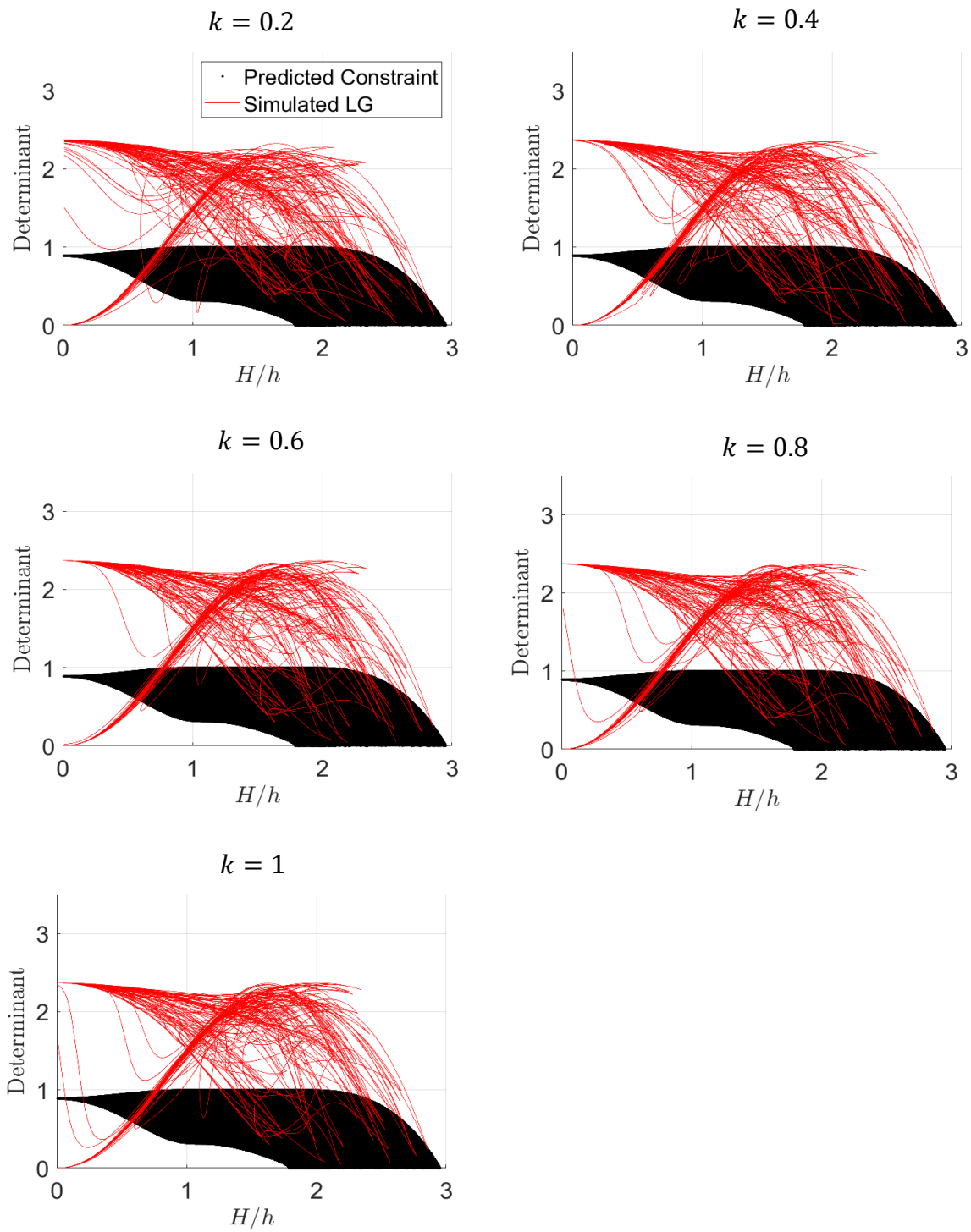


Figure 28. LG steering law's Ω for all 50 trajectories.

These plots highlight the main advantage of the provided control method: performance guarantees. For the provided steering law, at any angular-momentum state, the performance of the array can be predicted *a priori*. These performance guarantees dictate a maximum torque magnitude the array can produce in all directions. No such performance guarantees are offered by the LG steering law. With proper selection of k , the array may remain non-singular for the selected trajectories. However, another set of trajectories may result in the array becoming singular and in general, there is no guarantee of singularity avoidance for the LG steering law.

The comparison between the two steering laws comes down to whether or not the array needs to be capable of accessing the entire angular-momentum envelope. The LG steering law offers access to the entire array angular-momentum envelope shown in Figure 19, which the provided steering law does not. However, the LG steering law may become singular while operating. Thus, the LG steering law is a preferable steering law for applications where it is not critical to remain non-singular and the size of the CMGs is greatly limited, requiring the array to access the entire angular-momentum envelope. However, if it is critical that the array remain non-singular and the CMGs can be sized appropriately, enabling the array to remain in the constrained angular-momentum envelope, the provided CB steering law is likely preferable.

4.5 Conclusion

This chapter provides a CB steering law that enables singularity-free motion for the four-CMG box-90 array. For the provided CB steering law, performance guarantees are provided that specify the maximum torque magnitude that the array can produce in all directions at all reachable angular-momentum states. The chapter then compares the predicted performance of the CB steering law to that of the common LG steering law.

The comparison between the steering laws highlights the main benefit of the provided steering law over the LG steering law and other steering laws: performance guarantees. These performance guarantees not only guarantee singularity avoidance, ensuring that the array cannot actuate the body in all possible directions, but also specify the maximum torque magnitude that the array can always produce in all directions. These guarantees result in a robust control architecture by enabling desired maneuvers to be designed such that the required torque remains less than the guaranteed torque. Additionally, the performance guarantees enable the CMGs in the array to be more easily sized for a particular application by scaling the performance of the CMGs in the array, such that torque commands during operation are equal to or less than the torque magnitude that is guaranteed.

The main limitation of the steering laws is that it only applied to the four-CMG box-90 array. However, the idea of biasing the angular momentum of the planes of CMGs against one another can be employed in a similar manner to develop a general steering law for roof arrays.

CHAPTER 5 POLYHEDRAL EXTREME TERRAIN EXPLORATION ROVER

The previous chapters are focused on developing steering laws for CMGs that efficiently use the CMGs within the array. This chapter focuses on a rover architecture that exploits the torque efficiency of CMGs to enable efficient locomotion on extreme terrain.

Exploration of celestial bodies is challenging because the terrains vary wildly in topography (roughness) and composition: their surfaces can be icy, rocky, sandy, etc. However, for many applications, including exploration of celestial bodies and search and rescue, exploring these types of terrain is critical. Cornell University is currently developing a rover called Polyhedral Extreme Terrain Exploration Rover (PETER), designed to effectively navigate these terrains. PETER uses a single CMG to impart torque to roll across a surface. The polyhedral chassis and a single CMG offer two main benefits: 1) because PETER uses reactions to internal actuation for its mobility, the rover can be sealed and does not require joints that would be exposed with fine and abrasive regolith, eliminating the risk of actuator failure from interactions with the terrain; and 2) due to the torque efficiency of CMGs, small CMGs can produce large torques [1], enabling more massive rovers and efficient navigation of bodies with high gravitational field strengths.

This chapter investigates how the interaction between PETER and the ground can be exploited through morphology and control design, resulting in just one CMG being required to fully actuate PETER. Specifically, PETER's dynamics, including the interaction with the surface, are derived, informing PETER's morphology and the creation of a control system that enables PETER to locomote efficiently over extreme terrain. PETER's performance is evaluated using a dynamics simulation and compared to two rover architectures that use RWs for their mobility. The results of

the comparison show that PETER promises greater locomotion efficiency than the RW-actuated rovers due to the torque efficiency of PETER's CMG.

5.1 Previous Research

CMG-actuated polyhedral rovers expand the emerging field of internally-actuated surface mobility to bodies with higher gravity, compared to current internally-actuated rovers, which are primarily designed for exploration of microgravity bodies. Examples of the latter include the MINERVA [35], [36] and Hedgehog rovers [37], [38]. These rover architectures use RWs for hopping/tumbling mobility in microgravity environments. A third related concept is the iceCube rover, which uses CMGs but has a spherical body [39]. This otherwise versatile approach does not offer the benefit of polyhedral edges that constrain the motion, which implies that iceCube cannot stop permanently on a sloped surface.

5.2 Rover Design

The current design of PETER is shown in Figure 29. To locomote, PETER takes steps. To step, PETER rotates about any of its three edges that are formed by the three points that contact the ground. PETER uses spikes at each vertex (not shown in Figure 29) to lift the platform off the ground. Therefore, the effective edges are the lines that connect the spike tips. A step is defined as a positive rotation about an axis, \hat{r} , which passes through the tips of two adjacent spikes that are in contact with the ground until an adjacent spike contacts the ground. During normal operation, only the spikes are in contact with the ground, which is the situation considered here. In practice, for example, on very rocky terrain, a surface feature may contact the rover structure somewhere other than these spikes. However, less extreme topographies or judicious waypoint selection would

help prevent such contact. In principle, PETER can flip over a vertex or about an axis perpendicular to the surface, but these maneuvers are not the focus of this chapter.

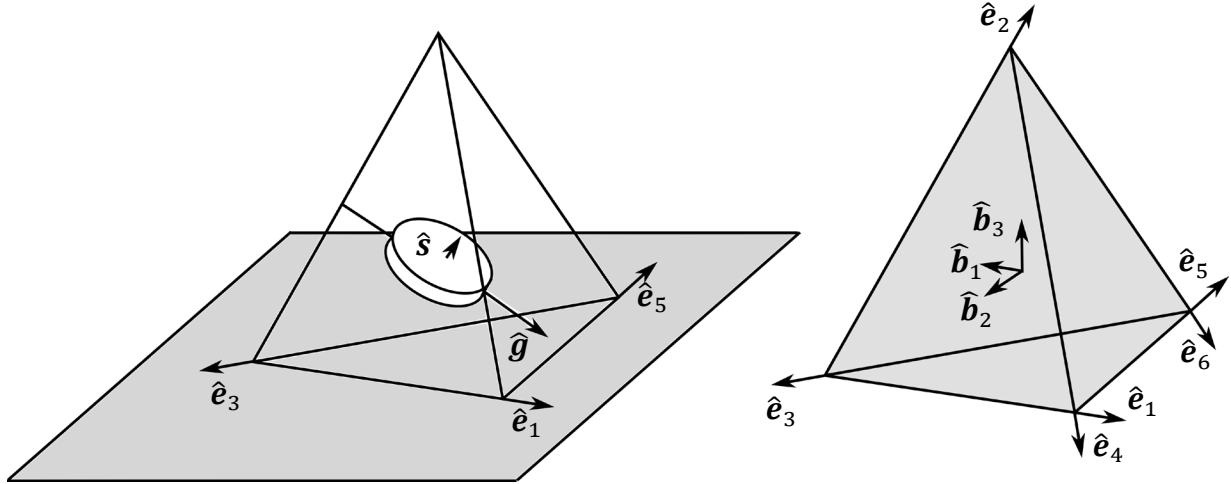


Figure 29. Current rover architecture.

PETER's chassis shape is selected to be a regular tetrahedron because it offers the greatest stability and robustness to disturbance torques during operation, while requiring little torque from the CMG to locomote. Details on the chassis selection are discussed in Section 7.4. The rover is actuated by a single CMG, which enables the rover to step about any of the six edges of the chassis. The orientation of the CMG within the chassis is shown in Figure 29 and in Eq. (67), where ${}^B\hat{g}$ is the matrix representation of \hat{g} in the body's fixed coordinate system, represented by \hat{b}_1 , \hat{b}_2 , and \hat{b}_3 . The gimbal axis is chosen to maximize the control authority of the CMG about each edge, allowing the greatest uniformity in all stepping directions. More specifically, the gimbal axis, \hat{g} , shown in Figure 29, minimizes Eq. (68), where \hat{e}_j is a vector that is parallel with the j^{th} edge of the tetrahedron.

$${}^B\hat{g} = \begin{bmatrix} 1 \\ -\frac{1}{\sqrt{2}} \\ 1 \\ -\frac{1}{\sqrt{2}\sqrt{3}} \\ 1 \\ -\frac{1}{\sqrt{3}} \end{bmatrix} \quad (67)$$

$$\min_{\hat{g}} \left\| \begin{bmatrix} \hat{e}_1 \cdot \hat{g} \\ \hat{e}_2 \cdot \hat{g} \\ \vdots \\ \hat{e}_6 \cdot \hat{g} \end{bmatrix} \right\|_{\infty} \quad (68)$$

The rows of Eq. (68) represent the gimbal axis projected onto each edge. A greater projection of the gimbal axis onto an edge results in reduced capability of the CMG to produce torque about that edge. Thus, minimizing the maximum projection of the gimbal axis onto each edge maximizes the minimum torque that the CMG can apply about each edge of the chassis. Due to the geometry of the chassis, the gimbal axis shown in Figure 29 results in the CMG having an equal control authority about four edges (\hat{e}_1 , \hat{e}_3 , \hat{e}_4 , and \hat{e}_6) and a greater torque authority about the remaining two edges (\hat{e}_2 and \hat{e}_5). Alternative gimbal axes enable greater torque performance about five edges, while having diminished capability to apply torque about one edge. However, if the rover cannot step about one edge, the rover is limited to a small portion of the environment, as shown in Figure 30. Additionally, traversing up inclines becomes difficult if the incline is aligned with the edge that corresponds to the reduced torque capability.

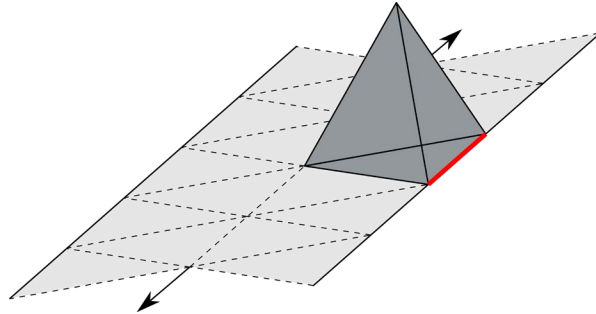


Figure 30. Accessible portion of the environment. *If the rover cannot step about the edge marked in red, then the rover can only access the shaded area of the environment.*

5.3 PETER's Dynamics

Unlike a RW, a CMG can change the direction of its output torque. As such, it can generate torque in different directions by controlling the gimbal trajectory, including the initial and final gimbal angles. However, with one CMG, a desired torque cannot be solely produced in a desired direction continuously. Thus, it is not possible to make a step where the CMG only produces torque along \hat{r} . To enable the rover to make a step when torque cannot be solely produced along \hat{r} , the contact between the surface and the chassis is exploited. The planetary surface continuously applies reaction forces onto the body. These forces can oppose some component of torque from the CMG, creating an effective null space, a direction where the CMG's torque is constrained to do no work. Past some limit, of course, the rover's point of contact may slip or the spikes may lift off the ground. However, if the CMG torque remains small enough, such that the surface can react the torque, the rover's chassis will remain static.

The effective null space has two main benefits for the rover's operations. First, when the rover is not making a step, the effective null space enables the CMG to produce a bounded non-zero torque while reorienting to a desired configuration without affecting the orientation of the rover.

The torque magnitude that the CMG cannot exceed while reorienting is called the static threshold torque, τ_{ST} . Second, if the CMGs torque about an edge corresponding to the desired step axis \hat{r} , is high enough to allow PETER to step, while the projected torque on the other edges is small enough such that the surface can react those torques, then PETER can make a desired step. Essentially, the effective null space enables the CMG to produce a bounded torque error in directions other than \hat{r} without affecting the rover's ability to make a step. The maximum torque magnitude that can be applied in the directions other than \hat{r} while stepping is referred to as the dynamic threshold, τ_{DT} .

The static and dynamic threshold torques enable a single CMG to actuate the rover, offering two main performance benefits. First, the torque output magnitude of a CMG, τ , scales with the rotor's radius r raised to the fourth power, if the rotor is a disc, as shown in Eq. (69), where I_r represents the rotors rotational inertia about its rotation axis, ρ represents its density, w represents its width, and ω represents its rotational rate. The mass of the rotor scales with r^2 , as shown in Eq. (70). Thus, if all else is the same, one larger CMG is more torque-efficient with respect to mass and volume than many small CMGs.

$$\tau = h\dot{\delta} = I_r\omega\dot{\delta} = \frac{1}{2}\pi\rho wr^4\omega\dot{\delta} \quad (69)$$

$$M_{rotor} = V\rho = \pi r^2 w\rho \quad (70)$$

Second, the mechanical and electrical systems are simplified. With one CMG, PETER requires just two motors: a gimbal motor and a rotor motor, with only the former directly responsible for locomotion.

This chapter primarily focuses on the dynamic threshold and how it enables a single CMG to actuate the system. PETER's dynamics are derived, quantifying the dynamic threshold and

providing equations of motion for the rover while stepping, enabling the development of a controller that exploits the dynamic threshold.

5.3.1 Dynamics Derivation

The derived dynamics describe the following simple case: 1) the center of mass of PETER is at the geometric centroid of the chassis and 2) each spike perfectly constrains position and permits three-axis rotation when in contact with the surface, resulting in the rotational acceleration about the surface normal $\hat{\mathbf{p}}$ being constrained to be zero if two or more spikes are in contact with the surface. Thus, the dynamic threshold only needs to be quantified about $\hat{\mathbf{N}}$, shown in Figure 31.

For the derivation, the CMG's fixed frame of reference is referred to as \mathcal{N} , and is shown in Figure 1. The coordinate system associated with the body's fixed frame of reference, B, is shown in Figure 31. The N and R frames are not shown, but they represent an inertial frame of reference and a rotor-fixed frame of reference, respectively.

$$\begin{aligned}
\boldsymbol{\tau}_e = & \underline{\mathbf{I}}_b \cdot \frac{B_d}{dt} \boldsymbol{\omega}^{B/N} + \boldsymbol{\omega}^{B/N} \times (\underline{\mathbf{I}}_b \cdot \boldsymbol{\omega}^{B/N}) + \mathbf{r}^{cm/o} \times M_P \frac{N_d^2}{dt^2} \mathbf{r}^{cm/o} \\
& + (\underline{\mathbf{I}}_r + \underline{\mathbf{I}}_g) \cdot \frac{G_d}{dt} \boldsymbol{\omega}^{G/B} + (\underline{\mathbf{I}}_r + \underline{\mathbf{I}}_g) \cdot \frac{B_d}{dt} \boldsymbol{\omega}^{B/N} + \boldsymbol{\omega}^{G/N} \times (\underline{\mathbf{I}}_r \cdot \boldsymbol{\omega}^{R/N} + \underline{\mathbf{I}}_g \cdot \boldsymbol{\omega}^{G/N}) \\
& - (\underline{\mathbf{I}}_r + \underline{\mathbf{I}}_g) \cdot (\boldsymbol{\omega}^{G/B} \times \boldsymbol{\omega}^{B/N})
\end{aligned} \tag{72}$$

The dynamics of the rover about the desired rotation axis are derived by dotting Eq. (72) with $\hat{\mathbf{r}}$.

$$\begin{aligned}
\boldsymbol{\tau}_e \cdot \hat{\mathbf{r}} = & (\mathbf{r}^{cm/o} \times M_P \mathbf{g}) \cdot \hat{\mathbf{r}} = \left(\underline{\mathbf{I}}_b \cdot \frac{B_d}{dt} \boldsymbol{\omega}^{B/N} \right) \cdot \hat{\mathbf{r}} + \left(\mathbf{r}^{cm/o} \times M_P \frac{N_d^2}{dt^2} \mathbf{r}^{cm/o} \right) \cdot \hat{\mathbf{r}} \\
& + \left((\underline{\mathbf{I}}_r + \underline{\mathbf{I}}_g) \cdot \frac{G_d}{dt} \boldsymbol{\omega}^{G/B} \right) \cdot \hat{\mathbf{r}} + \left((\underline{\mathbf{I}}_r + \underline{\mathbf{I}}_g) \cdot \frac{B_d}{dt} \boldsymbol{\omega}^{B/N} \right) \cdot \hat{\mathbf{r}} \\
& + \left(\boldsymbol{\omega}^{G/B} \times (\underline{\mathbf{I}}_r \cdot \boldsymbol{\omega}^{R/N} + \underline{\mathbf{I}}_g \cdot \boldsymbol{\omega}^{G/N}) \right) \cdot \hat{\mathbf{r}} \\
& - \left((\underline{\mathbf{I}}_r + \underline{\mathbf{I}}_g) \cdot (\boldsymbol{\omega}^{G/B} \times \boldsymbol{\omega}^{B/N}) \right) \cdot \hat{\mathbf{r}}
\end{aligned} \tag{73}$$

Equation (73) is simplified, more clearly describing the reaction of the body to a torque generated by the CMG.

$$-\mathbf{T} \cdot \hat{\mathbf{r}} = \left(\underline{\mathbf{I}}_b \cdot \frac{B_d}{dt} \boldsymbol{\omega}^{B/N} \right) \cdot \hat{\mathbf{r}} + \left(\mathbf{r}^{cm/o} \times M_P \frac{N_d^2}{dt^2} \mathbf{r}^{cm/o} \right) \cdot \hat{\mathbf{r}} - (\mathbf{r}^{cm/o} \times M_P \mathbf{g}) \cdot \hat{\mathbf{r}} \tag{74}$$

$$\begin{aligned}
\mathbf{T} = & (\underline{\mathbf{I}}_r + \underline{\mathbf{I}}_g) \cdot \frac{G_d}{dt} \boldsymbol{\omega}^{G/B} + (\underline{\mathbf{I}}_r + \underline{\mathbf{I}}_g) \cdot \frac{B_d}{dt} \boldsymbol{\omega}^{B/N} + \boldsymbol{\omega}^{G/B} \times (\underline{\mathbf{I}}_r \cdot \boldsymbol{\omega}^{R/N} + \underline{\mathbf{I}}_g \cdot \boldsymbol{\omega}^{G/N}) \\
& - (\underline{\mathbf{I}}_r + \underline{\mathbf{I}}_g) \cdot (\boldsymbol{\omega}^{G/B} \times \boldsymbol{\omega}^{B/N})
\end{aligned} \tag{75}$$

Equation (74) represents the equation of motion of the rover about the step axis $\hat{\mathbf{r}}$. This equation is implemented into the control discussed in Section 5.4.

The dynamic threshold torque is calculated for the case where the body has not started to rotate about $\hat{\mathbf{N}}$, so there is no angular acceleration or velocity about $\hat{\mathbf{N}}$, but enough off-axis torque is being applied to the body where all the weight is being support by a single spike. Two quantities

exist for the dynamic threshold torque, both representing the cases when the spike at point a or b , as shown in Figure 31, is supporting the weight of the rover. To change the calculation from spike a to b , $\mathbf{r}^{o/a}$ is replaced with $-\mathbf{r}^{o/a}$. For brevity, the derivation is completed for the spike point a . The angular momentum of the rover about point a is shown in Eq. (76).

$$\mathbf{H}_a = \underline{\mathbf{I}}_b \cdot \boldsymbol{\omega}^{B/N} + \mathbf{r}^{cm/a} \times M_P \frac{N_d}{dt} \mathbf{r}^{cm/a} + \underline{\mathbf{I}}_r \cdot \boldsymbol{\omega}^{R/N} + \underline{\mathbf{I}}_g \cdot \boldsymbol{\omega}^{G/N} \quad (76)$$

The derivative of Eq. (76) with respect to the Newtonian frame yields an equation of motion of the rover.

$$\begin{aligned} \boldsymbol{\tau}_e = & \underline{\mathbf{I}}_b \cdot \frac{B_d}{dt} \boldsymbol{\omega}^{B/N} + \boldsymbol{\omega}^{B/N} \times (\underline{\mathbf{I}}_b \cdot \boldsymbol{\omega}^{B/N}) + \mathbf{r}^{cm/a} \times M_P \frac{N_d^2}{dt^2} \mathbf{r}^{cm/a} \\ & + (\underline{\mathbf{I}}_r + \underline{\mathbf{I}}_g) \cdot \frac{G_d}{dt} \boldsymbol{\omega}^{G/B} + (\underline{\mathbf{I}}_r + \underline{\mathbf{I}}_g) \cdot \frac{B_d}{dt} \boldsymbol{\omega}^{B/N} + \boldsymbol{\omega}^{G/N} \times (\underline{\mathbf{I}}_r \cdot \boldsymbol{\omega}^{R/N} + \underline{\mathbf{I}}_g \cdot \boldsymbol{\omega}^{G/N}) \\ & - (\underline{\mathbf{I}}_r + \underline{\mathbf{I}}_g) \cdot (\boldsymbol{\omega}^{G/B} \times \boldsymbol{\omega}^{B/N}) \end{aligned} \quad (77)$$

For this case, the acceleration $\frac{N_d^2}{dt^2} \mathbf{r}^{o/a}$ is zero. Equation (77) is projected along $\hat{\mathbf{N}}$.

$$\begin{aligned} & - \left((\underline{\mathbf{I}}_r + \underline{\mathbf{I}}_g) \cdot \frac{G_d}{dt} \boldsymbol{\omega}^{G/B} + (\underline{\mathbf{I}}_r + \underline{\mathbf{I}}_g) \cdot \frac{B_d}{dt} \boldsymbol{\omega}^{B/N} + \boldsymbol{\omega}^{G/N} \times (\underline{\mathbf{I}}_r \cdot \boldsymbol{\omega}^{R/N} + \underline{\mathbf{I}}_g \cdot \boldsymbol{\omega}^{G/N}) \right. \\ & \quad \left. - (\underline{\mathbf{I}}_r + \underline{\mathbf{I}}_g) \cdot (\boldsymbol{\omega}^{G/B} \times \boldsymbol{\omega}^{B/N}) \right) \cdot \hat{\mathbf{N}} \\ & = \left(\underline{\mathbf{I}}_b \cdot \frac{B_d}{dt} \boldsymbol{\omega}^{B/N} \right) \cdot \hat{\mathbf{N}} + \left(\boldsymbol{\omega}^{B/N} \times (\underline{\mathbf{I}}_b \cdot \boldsymbol{\omega}^{B/N}) \right) \cdot \hat{\mathbf{N}} \\ & \quad + \left(\mathbf{r}^{cm/a} \times M_P \frac{N_d^2}{dt^2} \mathbf{r}^{cm/a} \right) \cdot \hat{\mathbf{N}} - \left(\mathbf{r}^{cm/a} \times M_P \mathbf{g} \right) \cdot \hat{\mathbf{N}} \end{aligned} \quad (78)$$

The left side of Eq. (78) represents the off-axis CMG torque, τ_{off} as shown in Eq. (79). The right side of Eq. (78) represents the dynamic threshold, τ_{DT} torque as shown in Eq. (80). Equation (81)

is made into an inequality, bounding the amount of torque the CMG can apply onto the off-axes of the rover while still having two spikes in contact with the surface for the analysis about spike tip a .

$$\begin{aligned} \tau_{off} = & - \left((\underline{\mathbf{I}}_r + \underline{\mathbf{I}}_g) \cdot \frac{G_d}{dt} \boldsymbol{\omega}^{G/B} + (\underline{\mathbf{I}}_r + \underline{\mathbf{I}}_g) \cdot \frac{B_d}{dt} \boldsymbol{\omega}^{B/N} \right. \\ & \left. + \boldsymbol{\omega}^{G/N} \times (\underline{\mathbf{I}}_r \cdot \boldsymbol{\omega}^{R/N} + \underline{\mathbf{I}}_g \cdot \boldsymbol{\omega}^{G/N}) \right. \\ & \left. - (\underline{\mathbf{I}}_r + \underline{\mathbf{I}}_g) \cdot (\boldsymbol{\omega}^{G/B} \times \boldsymbol{\omega}^{B/N}) \right) \cdot \hat{\mathbf{N}} \end{aligned} \quad (79)$$

$$\begin{aligned} \tau_{DTa} = & \left(\underline{\mathbf{I}}_b \cdot \frac{B_d}{dt} \boldsymbol{\omega}^{B/N} \right) \cdot \hat{\mathbf{N}} + \left(\boldsymbol{\omega}^{B/N} \times (\underline{\mathbf{I}}_b \cdot \boldsymbol{\omega}^{B/N}) \right) \cdot \hat{\mathbf{N}} \\ & + \left(\mathbf{r}^{cm/a} \times M_P \frac{N_d^2}{dt^2} \mathbf{r}^{cm/o} \right) \cdot \hat{\mathbf{N}} - \left(\mathbf{r}^{cm/a} \times M_P \mathbf{g} \right) \cdot \hat{\mathbf{N}} \end{aligned} \quad (80)$$

$$\tau_{off} \leq \tau_{DTa} \quad (81)$$

For the analysis about spike tip b , the inequality bounding the amount of off-axis torque for the CMG is shown in Eq. (82).

$$-\tau_{off} \leq -\tau_{DTb} \quad (82)$$

$$\begin{aligned} \tau_{DTb} = & \left(\underline{\mathbf{I}}_b \cdot \frac{B_d}{dt} \boldsymbol{\omega}^{B/N} \right) \cdot \hat{\mathbf{N}} + \left(\boldsymbol{\omega}^{B/N} \times (\underline{\mathbf{I}}_b \cdot \boldsymbol{\omega}^{B/N}) \right) \cdot \hat{\mathbf{N}} \\ & + \left(\mathbf{r}^{cm/b} \times M_P \frac{N_d^2}{dt^2} \mathbf{r}^{cm/o} \right) \cdot \hat{\mathbf{N}} - \left(\mathbf{r}^{cm/b} \times M_P \mathbf{g} \right) \cdot \hat{\mathbf{N}} \end{aligned} \quad (83)$$

5.4 Control Architecture

The dynamics of the effective null space must be included in the control system to enable the rover to locomote with one CMG. PETER’s control system has four main parts, as shown in Figure 32: 1) a path planner, which determines a series of steps such that the rover can traverse from the starting location to the desired end location, while avoiding obstacles; 2) a step trajectory planner, which computes a body and CMG trajectory for PETER to follow, so that PETER can complete the next step dictated by the path planner; 3) an initializing controller, which gimbals the CMG to the starting orientation specified by the step trajectory planner; and 4) a step tracking controller, which is a closed loop controller that computes gimbal rates that enable PETER to track the trajectory computed by the step trajectory planner. Step trajectory planner and the step trajectory tracker are the focus of this chapter.

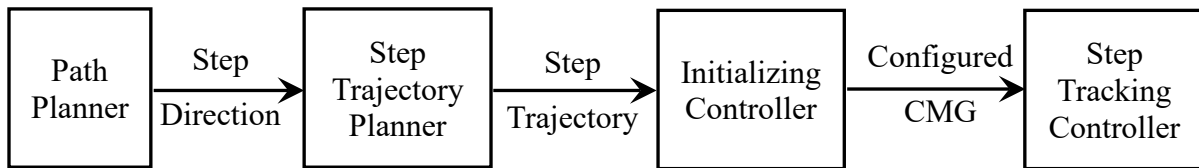


Figure 32. PETER’s control architecture.

5.4.1 Step Trajectory Planner

The step trajectory planner computes a trajectory for the body and CMG using an optimizer such that the rover can make a desired step. The goal of the optimizer is to compute a trajectory that maximizes the probability of successfully completing the desired step. Maximizing probability of completing the step successfully has two main benefits: 1) it reduces the complexity and computation of the path planner because the position of the rover can be forecast more accurately after multiple steps; and 2) it reduces the risk of unexpectedly stepping in hazardous directions, which could result in damage to the rover.

To maximize the probability of successfully completing the desired step, the robustness of the rover to disturbance torques during the steps is maximized. Of the three axes, $\hat{\mathbf{r}}$, $\hat{\mathbf{p}}$, and $\hat{\mathbf{N}}$, about which disturbances can be applied, the disturbances about $\hat{\mathbf{N}}$ have the greatest effect on the probability of successfully completing a step. If the disturbance torques about $\hat{\mathbf{N}}$ cause one of the two spikes to no longer remain in contact with the surface during a step, the predictability of the motion is greatly reduced because the effective null space is zero, which is essential for reacting the torques produced by the CMG that do not align with $\hat{\mathbf{r}}$. Disturbance torques about $\hat{\mathbf{p}}$ are unlikely to affect the rover's capability to make a step as long as two spikes remain in contact with the surface, because the expected friction between the spikes and the rover's spikes would likely require large disturbance torques to appreciably perturb away from the desired step. Disturbances about $\hat{\mathbf{r}}$ likely will not affect the completion of the step significantly because these disturbances are reacted by the trajectory tracking controller, as discussed in Section 5.4.2. Thus, to maximize the probability of successfully completing a desired step, robustness about $\hat{\mathbf{N}}$ is maximized by the trajectory optimizer.

To maximize the robustness of the rover about $\hat{\mathbf{N}}$, the minimum difference between the off-axes torque shown in Eq. (79) and the dynamic threshold torques shown in Eqs. (80, 83) is maximized. The optimization method implemented to maximize this difference is direct collocation [40], [41], which optimizes a trajectory at evenly spaced points in time along the trajectory, called collocation points. The optimization problem is shown in Eq. (84), where δ_o is the initial gimbal angle, $\dot{\delta}_o$ is the initial gimbal rate, $\ddot{\delta}$ is the gimbal acceleration trajectory, m is the number of collocation points for the optimization, and $\tau_{DT_{a_i}}$ and $\tau_{DT_{b_i}}$ represent the dynamic threshold at the i^{th} collocation point for spike contacts with the surface at points a and b , respectively. The initial gimbal rate is

a manipulatable parameter and is not constrained to be zero, resulting in a more stable optimization because large gimbal accelerations are mitigated in the beginning of the trajectory. During operation, the initial gimbal rate is constrained to be zero and the CMG has a finite maximum gimbal acceleration, resulting in a difference between the optimal trajectory and the rover's true trajectory during operation. The step tracking controller mitigates the effects of this difference through feedback control.

Direct collocation does not guarantee the computation of globally optimal solutions. Due to the complexity of the dynamics of the rover, the trajectory optimization likely yields locally optimal solutions and not globally optimal. Non-globally optimal solutions are acceptable as long as the resulting step trajectory enables the rover to step successfully.

$$\max_{\delta, \delta_o, \delta_o} (\min(C)) \quad (84)$$

$$C = \begin{bmatrix} \tau_{DTa_1} - \tau_{off_1} \\ -\tau_{DTb_1} + \tau_{off_1} \\ \tau_{DTa_2} - \tau_{off_2} \\ -\tau_{DTb_2} + \tau_{off_2} \\ \vdots \\ \tau_{DTa_m} - \tau_{off_m} \\ -\tau_{DTb_m} + \tau_{off_m} \end{bmatrix}$$

The manipulatable variables and the constraints for the optimization are shown in Table 1. The first two constraints shown in Table 1 ensure that the dynamic threshold is not exceeded. The third constraint bounds the time of the step to ensure that the step does not progress to infinite time. The gimbal rate limitation shown in the fourth constraint is derived from the limitation of the CMG hardware. Section 5.5.1 discusses the limitations of a prototype being developed at Cornell. The gimbal acceleration limit is specified to be a small value, less than is specified in Section 5.5.1.

The limitation on the gimbal acceleration promotes smoother trajectories, enabling a more stable computation of optimal trajectories. The sixth constraint ensures that the CMG remains sufficiently far from a singular state in the $\hat{\mathbf{r}}$ direction, enabling the CMG to apply output torque about the rotation axis and react to disturbances. The seventh and eighth constraints ensure that the rover starts at the desired initial state and ends at the desired final state. q represents the quaternion of the rover, q_o represents the desired initial quaternion of the rover, q_f represents the desired final quaternion of the rover. The final body rate of the rover is constrained to be zero, ensuring that the rover will not be harmed when hitting the ground after taking a step. The last constraint limits the magnitude of the bodies rotation rate about the rotation axis, reducing the risk of the rover contacting a surface at a high rate if there is a failure.

Inevitably, there are differences between the true rover dynamics and the dynamics implemented into the trajectory optimizer. Furthermore, the terra-mechanical properties in the actual environment will not result in zero translation of the spike points, as assumed in the optimization. These differences preclude the ability to track the trajectory using open loop control. Instead the closed-loop step tracking controller is implemented to enable PETER to track the trajectory.

Table 1. Optimization parameters.

Manipulatable Values		
1.	Initial gimbal angle (δ_o)	δ_o
2.	Initial gimbal rate ($\dot{\delta}_o$)	$\dot{\delta}_o$
3.	Gimbal acceleration ($\ddot{\delta}$)	$\ddot{\delta}$
Constraints		
1.	Off-axis torque	$\min(C) \geq 0$
2.	Dynamic threshold	$0 \leq \tau_{DT_{a_{1,2,\dots,m}}}, 0 \leq -\tau_{DT_{b_{1,2,\dots,m}}}$

3.	Final time (t_f)	$0 \leq t_f \leq 10\text{s}$
4.	Maximum gimbal rate ($\dot{\delta}$)	$ \dot{\delta} \leq \dot{\delta}_{max}$
5.	Maximum gimbal acceleration ($\ddot{\delta}$)	$ \ddot{\delta} \leq 5 \text{ rad/s}^2$
6.	Singular orientation	$(\hat{\mathbf{o}} \cdot \hat{\mathbf{r}})^2 \geq 0.1^2$
7.	Rover state at $t = 0$	$q = q_o, \boldsymbol{\omega}^{B/N}(t = 0) \cdot \hat{\mathbf{r}} = 0$
8.	Rover state at $t = t_f$	$q = q_f, \boldsymbol{\omega}^{B/N}(t = t_f) \cdot \hat{\mathbf{r}} = 0$
9.	Rover rotation rate	$ \boldsymbol{\omega}^{B/N} \cdot \hat{\mathbf{r}} \leq 2 \text{ rad/s}$

5.4.2 Step Tracking Controller

The step tracking controller computes a CMG gimbal rate, so that the body can accurately track the trajectory specified by the step trajectory planner. The single CMG can only control the motion of the rover about one axis instantaneously. The step tracking controller only regards the motion of the body about the rotation axis, $\hat{\mathbf{r}}$. The step controller is a computed torque controller [25], [42], a common control architecture for robotic systems.

The dynamics of the body about $\hat{\mathbf{r}}$ are shown in Eq. (74) above. The dynamics of the rover are simplified to enable a controller to be formulated. The simplifications of the CMG dynamics discussed in Chapter 2 are used to simplify Eq. (74), yielding Eq. (85).

$$\mathbf{T} \cdot \hat{\mathbf{r}} = \left(\underline{\mathbf{I}}_b \cdot \frac{d}{dt} \boldsymbol{\omega}^{B/N} \right) \cdot \hat{\mathbf{r}} + \left(\mathbf{r}^{cm/o} \times M_P \frac{d^2}{dt^2} \mathbf{r}^{cm/o} \right) \cdot \hat{\mathbf{r}} - \left(\mathbf{r}^{cm/o} \times M_P \mathbf{g} \right) \cdot \hat{\mathbf{r}} \quad (85)$$

$$\mathbf{T} = \delta h \hat{\mathbf{o}}$$

For normal operations where the rover is rotating only about $\hat{\mathbf{r}}$, Eq. (85) is simplified to Eq. (86), where $\ddot{\theta}$ is the angular acceleration of the rover about $\hat{\mathbf{r}}$.

$$\mathbf{T} \cdot \hat{\mathbf{r}} = \left(\underline{\mathbf{I}}_b \cdot \hat{\mathbf{r}} \right) \cdot \hat{\mathbf{r}} \ddot{\theta} + \left(\mathbf{r}^{cm/o} \times M_P (\hat{\mathbf{r}} \times \mathbf{r}^{cm/o}) \right) \cdot \hat{\mathbf{r}} \ddot{\theta} - \left(\mathbf{r}^{cm/o} \times M_P \mathbf{g} \right) \cdot \hat{\mathbf{r}} \quad (86)$$

$$\mathbf{T} = \delta \dot{h} \hat{\mathbf{o}}$$

The resulting computed torque controller is shown in Eq. (87), where k_p and k_d represent the proportional and derivative gains in a proportional derivative (PD) controller, respectively. θ is the angle of rotation of the rover about $\hat{\mathbf{r}}$ with respect to the starting orientation of the rover, θ_r is the desired angle of rotation of the rover about $\hat{\mathbf{r}}$ with respect to the starting orientation of the rover, $\dot{\theta}$ is the rotational rate of the rover about $\hat{\mathbf{r}}$, $\dot{\theta}_r$ is the desired rotational rate of the rover about $\hat{\mathbf{r}}$, and $\ddot{\theta}_r$ is the desired rotational acceleration of the rover about $\hat{\mathbf{r}}$,

$$\delta_c = \frac{N(k_p \theta_e + k_d \dot{\theta}_e + \ddot{\theta}_r) - (\mathbf{r}^{cm/o} \times M_p \mathbf{g}) \cdot \hat{\mathbf{r}}}{h \hat{\mathbf{o}} \cdot \hat{\mathbf{r}}} \quad (87)$$

$$N = \left(\mathbf{I}_b \cdot \hat{\mathbf{r}} + \mathbf{r}^{cm/o} \times M_p (\hat{\mathbf{r}} \times \mathbf{r}^{cm/o}) \right) \cdot \hat{\mathbf{r}}$$

$$\theta_e = \theta_r - \theta$$

$$\dot{\theta}_e = \dot{\theta}_r - \dot{\theta}$$

If the output axis $\hat{\mathbf{o}}$ is perpendicular to $\hat{\mathbf{r}}$, the gimbal rate is infinity. As discussed above, to mitigate the effects of these singularities, the trajectories are computed to avoid singularities. The step trajectory planner in conjunction with the step tracking controller enable PETER to make a step about any edge.

5.5 PETER's Predicted Performance

To compare the effectiveness of PETER's mobility, the control performance is evaluated in simulation. The mobility performance metric for the rover used here is the energy per meter traveled per kilogram of the rover, which is referred to as the cost of travel. Lower cost of travel enables greater coverage in exploration and more energy for payload instruments rather than mobility actuators. The energy is normalized for distance traveled and mass of the rovers, so that

rovers with varying physical specifications can be compared. To simplify assessing the cost of travel, energy is calculated for only the CMG gimbal motor and rotor motor, which represents the energy required by the CMG for actuation. The analysis does not account for friction or electronic losses.

PETER's performance is evaluated for the case of traversing inclines in Martian gravity. Inclines are given close attention because they represent a common extreme terrain that the rover will likely traverse during operation. Additionally, other terrains can be approximated by inclines, including rocky terrain where the rover must traverse over large rocks. Assuming adequate friction and stable slopes, the inclines tested range from zero to 55 degrees, which represents the greatest incline PETER can traverse without requiring continuous actuator input to remain static after a step is complete. Steeper inclines are not considered because these inclines would need to be avoided in case of power failure or control failure, which would result in PETER rolling uncontrolled, potentially harming the rover.

5.5.1 Experimental Rover Specifications

Table 2 lists the parameters used for PETER and the environment. PETER's specifications are derived from a preliminary prototype design of the rover that is being built at Cornell University. The design of PETER is ongoing. Thus, these numbers should be considered as estimates of PETER's final properties. For the purposes of the work, the design is not discussed in detail. Instead, only the design characteristics needed for the analysis are reported. The mass of the rover does not include a payload. Instead the mass represents the mass of the chassis, CMG, and power system. The inertia value assumes equal distribution of the mass throughout the tetrahedral chassis.

Table 2. PETER's and the environment's parameters.

PETER	Mass (M_p)	47 kg
	Chassis edge length (L)	1 m
	Inertia matrix of chassis about the center of mass (${}^B I_b$)	$\left(\frac{1}{20}\right) M_p L^2 I_{3 \times 3}$
	Inertia matrix of CMG's rotor about its center of mass (${}^G I_r$)	$\begin{bmatrix} 0.14 & 0 & 0 \\ 0 & 0.08 & 0 \\ 0 & 0 & 0.08 \end{bmatrix} \text{kgm}^2$
	Inertia matrix of CMG about its center of mass (${}^G I_r + {}^G I_g$)	$\begin{bmatrix} 0.55 & 0 & 0 \\ 0 & 0.45 & 0 \\ 0 & 0 & 0.36 \end{bmatrix} \text{kgm}^2$
	CMG angular momentum (h)	115 Nms
	CMG rotor rotation rate	800 rad/s
	CMG maximum gimbal rate	2 rad/s
	CMG maximum gimbal acceleration	20 rad/s ²
Environment	Mars' gravity (g)	3.711 m/s ²

5.5.2 Analysis Techniques

A dynamic simulation is used to evaluate PETER's performance, which comprises three major elements: 1) the controller that enables the rover to step, which is presented in Section 5.4; 2) a model of the body and CMG dynamics, which integrates the complete governing equations, including environmental effects such as collisions and gravity; and 3) a simulation of the power system for the CMG that computes the energy used by the gimbal and rotor motors throughout the step.

The model of the dynamics incorporates all the CMG effects shown in Eq. (75), the rigid-body effects of PETER's chassis, and the collision between the surface spike points. The collision of the body with the surface is modeled as a unidirectional spring and damper in the direction normal of the surface and as a bidirectional damper in the direction parallel with the surface as shown in Figure 33. The values for the spring and damper system are shown in Table 3. The values are

selected to represent a stiff surface, where the sliding friction between the corners of the chassis and surface is high. The stiffness of the surface and the friction are chosen to be large because it is assumed that on rocky Martian terrain, the spikes contact with the surface would result in a stiff interaction.

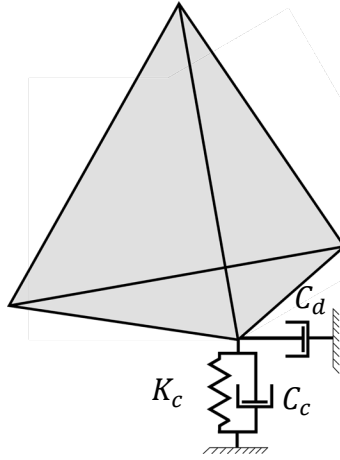


Figure 33. Model of the terra-mechanical properties implemented in the dynamic simulation. *The damper parallel with the surface acts opposite of the motion of the spikes in contact with the surface.*

Table 3. Terra-mechanical properties for the simulation.

Terra-mechanical Properties	Value
K_c	1×10^5 N/m
C_c	1×10^6 Ns/m
C_d	1×10^5 Ns/m

The energy used by the gimbal motor and rotor motor are calculated using Eq. (88), which represents the integral of the absolute value of the mechanical power required for the step.

$$E = \int_0^{t_f} |T_r \cdot \omega^{R/G}| + |T_g \cdot \omega^{G/B}| dt \quad (88)$$

$$\mathbf{T}_r = - \left(\underline{\mathbf{I}}_r \cdot \frac{G_d}{dt} \boldsymbol{\omega}^{G/B} + \underline{\mathbf{I}}_r \cdot \frac{B_d}{dt} \boldsymbol{\omega}^{B/N} + \boldsymbol{\omega}^{G/N} \times (\underline{\mathbf{I}}_r \cdot \boldsymbol{\omega}^{R/N}) - \underline{\mathbf{I}}_r \cdot (\boldsymbol{\omega}^{G/B} \times \boldsymbol{\omega}^{B/N}) \right)$$

$$\mathbf{T}_g = - \left((\underline{\mathbf{I}}_r + \underline{\mathbf{I}}_g) \cdot \frac{G_d}{dt} \boldsymbol{\omega}^{G/B} + (\underline{\mathbf{I}}_r + \underline{\mathbf{I}}_g) \cdot \frac{B_d}{dt} \boldsymbol{\omega}^{B/N} + \boldsymbol{\omega}^{G/N} \times (\underline{\mathbf{I}}_r \cdot \boldsymbol{\omega}^{R/N} + \underline{\mathbf{I}}_g \cdot \boldsymbol{\omega}^{G/N}) \right. \\ \left. - (\underline{\mathbf{I}}_r + \underline{\mathbf{I}}_g) \cdot (\boldsymbol{\omega}^{G/B} \times \boldsymbol{\omega}^{B/N}) \right)$$

Due to the symmetry in the design of PETER, a optimal trajectory that enables PETER to step about $\hat{\mathbf{e}}_1$ also enables PETER to step about the $\hat{\mathbf{e}}_3$, $\hat{\mathbf{e}}_4$, and $\hat{\mathbf{e}}_6$ axis. The only difference between the steps is the initial gimbal angle. The same is true for steps about $\hat{\mathbf{e}}_2$ and $\hat{\mathbf{e}}_5$. Thus, PETER's performance is only reported for steps about $\hat{\mathbf{e}}_1$ and $\hat{\mathbf{e}}_2$.

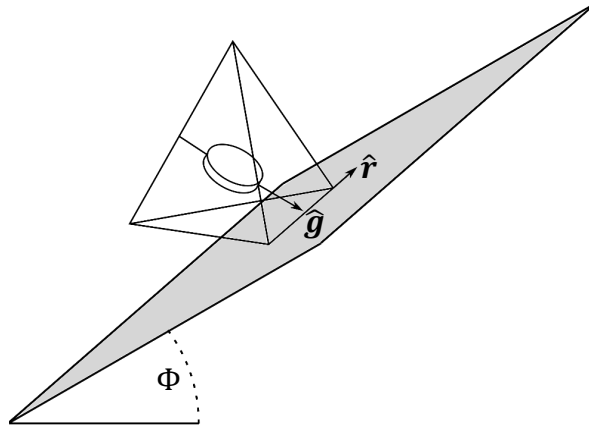


Figure 34. PETER stepping up an incline.

5.5.3 Results

Figures 35 and 36 show steps about $\hat{\mathbf{e}}_1$ and $\hat{\mathbf{e}}_2$ on each Φ , as shown in Figure 34. The cost of travel of PETER for steps about $\hat{\mathbf{e}}_1$ and $\hat{\mathbf{e}}_2$ on each incline are shown in Table 4. The average cost of travel shown is the average for steps about all edges.

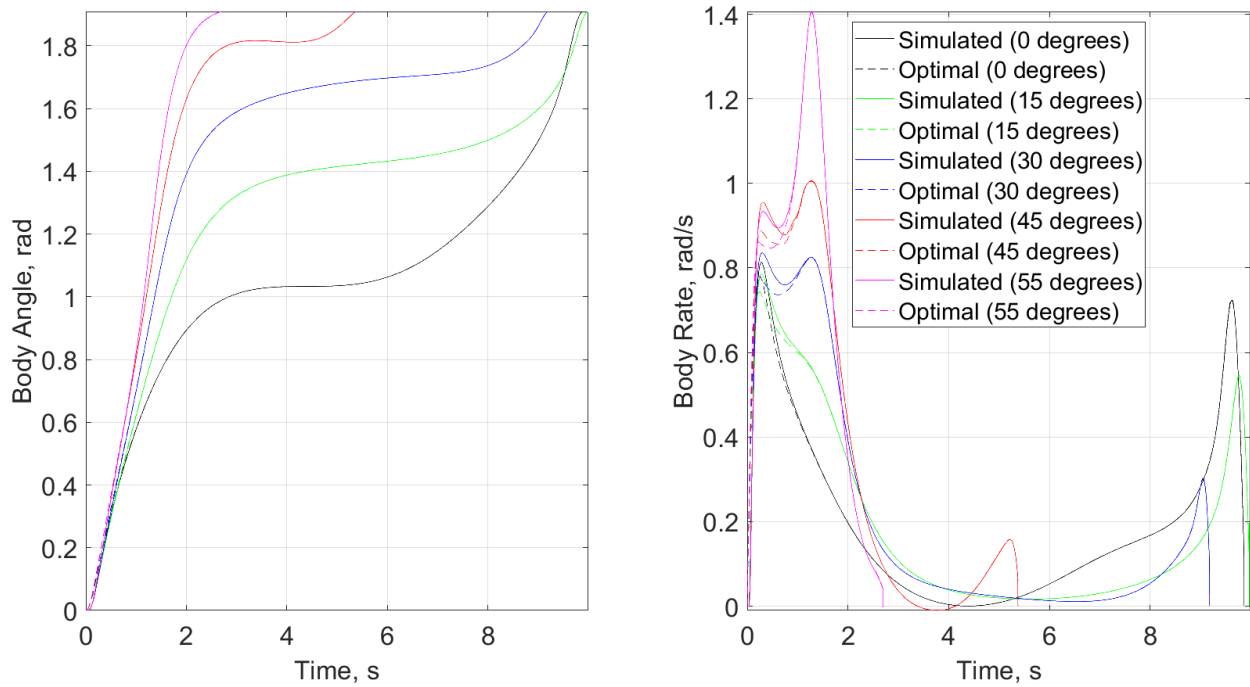


Figure 35. Body angle and body rate with respect to time for steps about \hat{e}_1 . *The dashed lines represent the optimal trajectories computed by the step trajectory planner. The solid lines represent the trajectory of the rover in the simulation.*

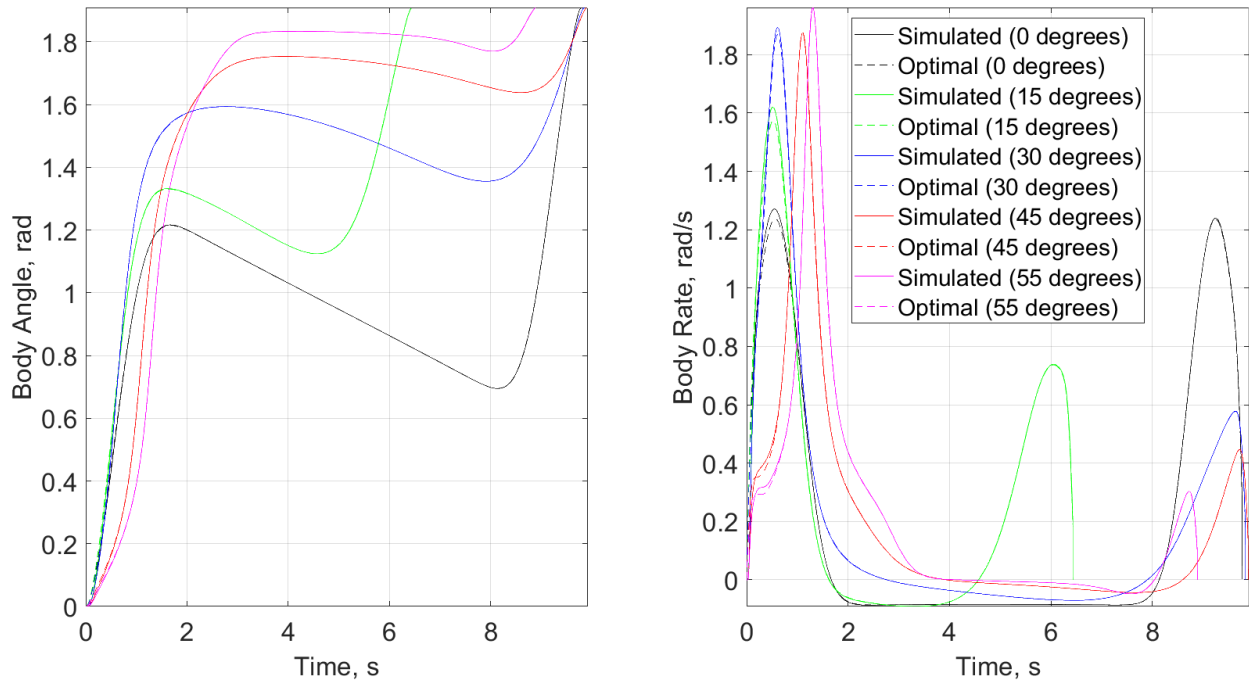


Figure 36. Body angle and body rate with respect to time for steps about \hat{e}_2 . The dashed lines represent the optimal trajectory computed by the step trajectory planner. The solid lines represent the trajectory of the rover in the simulation.

Table 4. PETER’s performance.

Incline Angle (degrees)	\hat{e}_1 (J/kg/m)	\hat{e}_2 (J/kg/m)	Average (J/kg/m)
0	5.6	19.2	9.8
15	6.7	18.0	10.5
30	6.6	16.5	9.9
45	8.3	13.6	10.1
55	10.7	12.3	11.3

5.5.4 Discussion

Figures 35 and 36 show that with just one CMG, the control system discussed in Section 5.4 enables the rover to step on each simulated incline with little difference between the optimal trajectory and the simulated motion of the rover during the step. There are perceivable differences

in the optimal trajectory and the simulated motion of the rover at the beginning due to a combination of the gimbal acceleration limitations and the fact that the initial gimbal rate for the CMG is not constrained to be zero when computing the optimal trajectories, as discussed above in Section 5.4.1. Table 4 shows PETER's cost of travel increases with incline for steps about \hat{e}_1 and decreases for steps about \hat{e}_2 , resulting in an approximately constant average cost of travel.

5.6 Contextualization of Performance

To provide context for PETER's cost of travel, PETER's performance is compared to two other rover architectures: the Hedgehog rover [37], [38] and a Hedgehog variant that uses a tetrahedral chassis to eliminate variations that result from the rovers' geometry. The Hedgehog variant is referred to as the hypothesized rover. The Hedgehog rover is chosen for comparison because among current mobility concepts, Hedgehog is closest to PETER in its mobility modality: both use reactions to angular momentum for locomotion. Hedgehog is a cubic rover actuated by RWs designed to hop or roll on bodies with microgravity [37], [38]. Prior research in Hedgehog has investigated the use of reaction wheels for hopping/tumbling mobility in microgravity environments. This work investigates a different mechanism for internal actuation – CMGs. The continued research in planetary mobility furthers our understanding of different mobility modalities including their robustness, efficiency and ability to handle the unknown and harsh environments of space. These efforts are steps toward such goals to be able to respond to new discoveries and science needs.

The cost of travel for both RW actuated rovers is computed by evaluating the energy used by the RWs during a step. The Hedgehog specifications used in this comparison are shown in Table 5 [37]. Similar to the mass of PETER, the mass of Hedgehog only incorporates the mechanical

assembly, the actuators, and the power system, and does not include the mass of the payload. Additionally, because the rover's inertia is not offered in the literature, the inertia of the rover is calculated assuming equal distribution of the mass throughout the cubic chassis.

Table 5. Hedgehog's specification.

Mass (M_h)	18.75 kg
Chassis edge length (L_h)	0.25 m
Inertia matrix (${}^B I_h$)	$\frac{1}{6} M_h L_h^2 I_{3 \times 3}$
Reaction wheel inertia (I_{RW})	0.00095 kg m ²

The specifications of the hypothesized rover are chosen to be identical to Hedgehog's current specifications, except for the chassis edge length and inertia. The tetrahedral chassis edge length is selected as 0.61 m, resulting in the tetrahedral chassis and Hedgehog's cubic chassis having an inscribed sphere of the same size. It is assumed that most of the hardware of both rovers would be contained within this inscribed sphere, thus comparing rovers with the same inscribed sphere is analogous to comparing rovers with the same capabilities of housing actuators and payloads.

5.6.1 Evaluated Steps

Rovers with RWs generate motion through a reaction to the angular momentum that is generated by accelerating or decelerating its RWs. Two types of locomotion for the RW actuated rovers are explored in this chapter: an impulsive step and a versine step. During an impulsive step, the rover spins up a RW to a specified speed, with a controlled acceleration to prevent motion. When a step in a given direction is desired, the rotor is stopped instantaneously by applying a brake [37]. The angular momentum of the rotor is then largely transferred to the body, with some losses

that result from rotor's energy converted to heat. For this step, the rotor uses energy to spin to the desired speed prior to each step.

Four assumptions are made to simplify the analysis of the impulsive step: 1) there is no loss in momentum between pre- and post-brake, *i.e.* the momentum of the rover an instant after the rotors are impulsively braked is equal to the momentum of the rover an instant before the rotors are impulsively braked; 2) the electronics are lossless and there is no drag acting on the RWs; 3) the inertia values of the rotors about axes other than the rotation axis are assumed to be sufficiently small such that they can be excluded from the analysis (off-axis inertia is not available for this platform in the literature); 4) the contact between the spikes and the surface do not slip (*i.e.* the motion at the contact points are purely rotational with zero translation); and 5) the energy of the rover after the rotors are impulsively braked is (optimistically) the same as the change in potential energy of the rover from when the rover is on the ground to when it has rotated to the point where the center of mass is at its highest. This change in potential energy is represented by Eq. (89), where pitch angle of the incline is represented as Φ as shown in Figure 34 and the value for α is described by Eq. (91) and Eq. (92) for tetrahedral and cubic chassis, respectively. The resulting equation for the energy used by the RWs during an impulsive step is shown in Eq. (90), which reflects the ideal minimum energy required for the rover to step specified in previous analyses [37].

$$U = M_h g \sqrt{{}^{B_r} \mathbf{cm}/o^T {}^{B_r} \mathbf{cm}/o} (1 - \cos(\alpha + \Phi)) \quad (89)$$

$$E = \frac{\left({}^{B_r} \mathbf{T} {}^{B_r} \mathbf{I}_h {}^{B_r} + M_h {}^{B_r} \mathbf{cm}/o^T {}^{B_r} \mathbf{cm}/o \right) U}{I_{RW}} \quad (90)$$

$$\alpha_{tetrahedral} = \frac{\pi}{2} - \sin^{-1}\left(\frac{1}{\sqrt{3}}\right) \quad (91)$$

$$\alpha_{cube} = \frac{\pi}{4} \quad (92)$$

The value of E shown in Eq. (90) represents the lower bound of the energy needed to step. If the value is matched, the rover will stop at the highest point in the step. Any more energy and the rover will complete the step. For practical applications where terra-mechanical properties are considered, E would need to be increased to react any energy losses due to terra-mechanical effects.

The versine step is evaluated for two reasons: it represents a common continuous trajectory used for other aerospace applications, and it provides a reference for the performance of the RW actuated rovers when implementing a continuous step. The versine step is shown in Eqs. (93 - 95), where θ_r represents the angle of rotation of the body about \hat{r} from the starting static orientation.

$$\theta_r = \alpha(1 - \cos(At)) \quad (93)$$

$$\dot{\theta}_r = A\alpha \sin(At) \quad (94)$$

$$\ddot{\theta}_r = A^2\alpha \cos(At) \quad (95)$$

A is chosen to limit the maximum body rate to 2 rad/s, which is also the limit applied to the optimization used to compute PETER's steps, as discussed in Section 5.4.1. The performance of the versine steps is evaluated using a dynamic simulation that includes the rigid body dynamics of the chassis and the RWs.

The equation used to compute the energy expended by the RWs is shown in Eq. (96), where \mathbf{T}_{RW_i} represents the torque produced by the i^{th} RW, and $\boldsymbol{\omega}^{R_i/B}$ is the rate of rotation of the i^{th} RW with respect to the body.

$$E = \int_0^{t_f} \sum_{i=1}^3 |\mathbf{T}_{RW_i} \cdot \boldsymbol{\omega}^{R_i/B}| dt \quad (96)$$

$$\mathbf{T}_{RW_i} = - \left(\mathbf{I}_{RW_i} \cdot \frac{B_d}{dt} \boldsymbol{\omega}^{R_i/N} + \boldsymbol{\omega}^{B/N} \times (\mathbf{I}_{RW_i} \cdot \boldsymbol{\omega}^{R_i/N}) \right)$$

5.6.2 Results

Table 6 shows the average performance for all edges of the chassis at different inclines for PETER, Hedgehog, and the hypothesized rover. The performance of Hedgehog on a 55-degree slope is not provided, because the cubic chassis does not permit the rover to remain static on a 55-degree slope after the step without actuator input.

Table 6. Energy used by each rover for a step on inclines.

	PETER	Hedgehog		Hypothesized Rover	
Incline Angle (degrees)	Average (J/kg/m)	Impulsive (J/kg/m)	Versine (J/kg/m)	Impulsive (J/kg/m)	Versine (J/kg/m)
0	9.8	632.1	5844.6	1086.1	11070.3
15	10.5	1079.0	9129.1	1679.7	16261.0
30	9.9	1599.4	11331.4	2333.9	19470.4
45	10.1	2158.0	12834.2	3004.2	20984.0
55	11.3	NA	NA	3426.2	21407.6

The operation of PETER is fundamentally different from Hedgehog and the hypothesized rover in two ways. First, the CMG rotor is continuously spinning, even if the rover is static. Thus, at all times during the mission the CMG is consuming power to overcome aerodynamic drag and bearing drag. Most CMGs operate in a vacuum, which is assumed here, resulting in near zero aerodynamic drag. For the prototype being developed at Cornell University, the estimated power required to react both the aerodynamic drag and the bearing drag is 50 Watts, which matches similar quiescent power draw values reported for similarly sized CMGs [43], [44]. Second, the rover must spin up

the rotor prior to the start of the mission. This spin-up is conducted only once. Thus, the longer the CMG operates, the less effect the spin-up has on the rover's total efficiency. The energy required to spin up the rotor is dependent on the time it takes to spin up the rotor and the amount of drag acting on the rotor. From the preliminary analysis of the prototype rover, it takes approximately 30 minutes to spin up the rotor. However, the spin-up can only be accomplished in that time assuming the batteries have enough capacity to spin up the rotor without being recharged. Thus, it is expected that the rover would need to recharge the batteries during the spin-up using either solar panels on the chassis or another source. For these reasons, the spin-up will likely take significantly longer than 30 minutes. For this study, it is assumed that it will take 24 hours to spin the rotor up, which is more conservative than other reported spin-up times [1], [43]. For simplicity, it is assumed that the rotor must continuously exert 50 Watts to overcome drag forces during the spin-up.

Incorporating these effects, PETER's efficiency is analyzed for missions traveling 50 m, 78 m, 100 m, 1000 m, and 10000 m. For the analysis, three simplifications are made about the mission: 1) PETER uses on average the average energy it takes to step about all edges and inclines (i.e., the average of Column 2 in Table 6); 2) the time required to step is equal to the average time required to step for steps about all edges on all inclines; 3) PETER is assumed to pause for 1 minute between each step to enable the CMG to be configured for the next step and to compute the next optimal step trajectory; and 4) zero energy is required by the gimbal motor to reconfigure the CMG between steps. The configuration of the CMG is a relatively slow process and likely will require little energy.

With these simplifications, the cost of travel for missions travelling 50 m, 78 m, 100 m, 1000 m, and 10000 m, are shown in Table 7. Table 7 also shows the average cost of travel for Hedgehog

and the hypothesized rover's impulsive steps for the same missions, which is equal to the average of Columns 3 and 5 in Table 6 for Hedgehog and the hypothesized rover, respectively. for Hedgehog and the hypothesized rover, respectively. The distance traveled 78 m is included because it approximately represents the point at which Hedgehog and PETER have the same cost of travel.

Table 7. Energy efficiency during three different missions.

Distance Traveled (m)	PETER (J/kg/m)	Hedgehog (J/kg/m)	Hypothesized Rover (J/kg/m)
50	2038.1	1367.1	2306.0
78	1367.1	1367.1	2306.0
100	1109.7	1367.1	2306.0
1000	273.5	1367.1	2306.0
10000	190.0	1367.1	2306.0

5.6.3 Discussion

Table 6 shows that the versine step is less efficient than the impulsive step, and so is unlikely to be used during operation. Table 7 shows that the energy efficiency of PETER is highly dependent on the distance traveled during the mission. For short distances, PETER has approximately equal energy efficiency to Hedgehog. However, as the distance increases, PETER's energy efficiency is greatly increased, resulting in a cost of travel that is significantly less than the RW-actuated rovers. The results in Table 6 and Table 7 also suggest that this increase in performance is due to the actuation method and not the chassis shape. These results are congruent with other applications of CMGs, where CMGs are often more torque efficient with respect to power than RWs [1], [6].

This preliminary analysis shows great promise for energy-efficient mobility architectures that use rolling as their primary means of surface locomotion. The CMG offers additional benefits

to the low-energy rolling. The dynamics of CMG are such that the final velocity of the step can be controlled to reduce the impact velocity with the ground, which would increase reliability, especially on bodies with larger gravity. Moreover, the torque scaling for robots that use CMG actuators allows for larger and more massive rovers. These two aspects, along with the fact that the PETER becomes more efficient as distance traveled increases, make the rover appropriate for missions where PETER can slowly locomote during a long-mission lifetime. RW-based rovers such as Hedgehog would be better suited for short duration missions or missions on lower gravity bodies, where smaller rovers that can efficiently cover the surface of the body through a combination of hopping and rolling.

5.7 Conclusion

This work represents the first steps in understanding the performance of a CMG-driven polyhedral rover. A key result is that a single CMG is sufficient to control a rolling rover. The control approach can use the interaction with the ground to direct the movement, due to the polyhedral shape of the rover. The chapter provides design parameters and a control architecture that exploits the interaction between the surface and the rover, enabling the rover to locomote. Simulation results provide a preliminary confirmation that the rover and control architecture are suitable for planetary surface applications. These simulation results show that PETER, with one CMG, locomotes more efficiently than RW-actuated rovers during long lifetime mission on bodies with high gravity and on terrain with steep inclines. Additionally, the simulation results suggest that this performance increase is due to the energy efficiency of CMGs and not the chassis shape.

There are three main limitations to this study. First, the evaluation of PETER's performance is limited to traversing directly up an incline with a firm surface. Because the rover is intended to be

used in extreme terrain, more complex topographies and terra-mechanical properties should be explored.

Second, PETER's control system relies on the terra-mechanical properties of the surface being approximated by no-slip conditions at each spike point. With sufficient deviation between the true terra-mechanical properties and the assumed terra-mechanical properties, the rover's motion may be less predictable and less efficient. To enable more predictable and robust motion of the rover, the terra-mechanical properties of the environment must be included in PETER's control system. Past research has explored methodologies for learning terra-mechanical properties online using machine learning approaches for Ackerman steering vehicles [45]–[47]. These methodologies can be implemented into PETER's control system. Specifically, using these methodologies, a learned model of the terra-mechanical properties can be incorporated into the step trajectory planner, discussed in Section 5.4.1, enabling more accurate and robust computation of step trajectories. These methodologies could then be used to compute optimal gains for the step tracking controller discussed in Section 5.4.2, to enable robust tracking of the step trajectory.

Third, this work does not discuss the selection of chassis size or CMG size. While CMGs do scale up well, small CMGs lose many of the performance benefits compared to RWs due to mechanical limitations [1], [6]. Thus, small rovers with small CMGs likely have poorer performance than larger rovers with larger CMGs.

CHAPTER 6 CONCLUSION

The work in dissertation advances the field of momentum control systems and their applications in robotic systems. Specifically, this work offers high-performance and robust steering laws for CMGs. The dissertation offers a general steering law for planar CMGs that achieves globally optimal performance in closed form. The generality of the steering law enables fault-tolerant operation. The closed-form formulation eliminates the issues associated with numerical implementations, which can result in instabilities. The steering law for planar arrays is further generalized to the four-CMG Box-90 array, which represents one of the most common arrays in practice. The resulting steering law achieves a high level of performance and predictability in the form of performance guarantees. The performance guarantees dictate the performance of the array during operation, increasing the robustness of the array by enabling maneuvers to be planned that are guaranteed to be achievable. The dissertation then offers a novel implementation of CMGs that exploits their torque efficiency. Specifically, design principles and a control system for the rover are offered for a CMG actuated rover. Through exploitation of the contact between the rover and the surface in conjunction with the torque efficiency of CMG, the rover architecture is capable of high-performance and energy-efficient locomotion on extreme terrain. The performance of the rover enables exploration of currently unexplored environments, including Martian riverbeds and craters. Additionally, the rover enables efficient exploration of rubble, enabling the rover to be used for search and rescue missions.

The work offered in this dissertation can be expanded upon in many ways. Specifically, CB steering laws have shown a lot of promise. However, many implementations have algorithmic singularities, necessitating the feedback control method for the implementation to access the full

angular-momentum space. It is difficult to develop performance guarantees for feedback control methods because they necessarily enable the array to progress away from a constrained gimbal-angle sets. Developing a general methodology to compute performance guarantees using modern verification methods, like barrier certificates [48]–[50], would greatly increase the robustness and applicability of CB steering laws. Furthermore, the dynamics that most steering laws consider, which is the dynamics considered here, is a simplified model of the CMG’s true dynamics. Developing steering laws for a more accurate model of the CMG’s dynamics, potentially by including the base rate effect, would greatly increase the torque accuracy of CMG arrays, increasing the accuracy in which the body can track a trajectory. Lastly, most of this work explores developing CB steering laws for CMG arrays that are commonly used in practice. However, the performance of arrays and the difficulty of developing CB steering laws are greatly dependent on the array’s architecture. Exploring how the array architecture can be manipulated to promote high performance and easy development of CB steering laws could greatly increase the applicability of these methodologies and potentially lead to high-performance implementations of CMGs.

APPENDIX

7.1 Torque Capability Derivation

Torque capability (TC) is a normalized representation of the maximum torque the array can produce in all directions given the gimbal rate limitations of the CMGs in the array. The derivation of TC depends on the steering law and the array's architecture. This section provides a derivation of TC for three cases: 1) the Moore-Penrose pseudoinverse and an arbitrary array architecture; 2) the augmented Jacobian CB steering law with an arbitrary constraint formulation and the four-CMG Box-90 array; and 3) the LG steering law with an arbitrary cost function and the four-CMG Box-90 array.

For the derivations it is assumed that the gimbal rate limitations of the array are equal for all CMGs in the array and that each CMG has an equal capability of producing a positive or negative gimbal rate. The derivation of TC has four steps. First, the maximum gimbal-rate magnitude for one CMG that could result from producing an arbitrary finite torque in any direction is derived. Second, the maximum gimbal-rate magnitude of any CMG in the array resulting from producing an arbitrary finite torque in any direction is derived. Third, the maximum torque magnitude the array can produce in all directions is derived. Lastly, the maximum torque magnitude the array can produce in all directions is normalized by the maximum torque magnitude each CMG in the array can produce.

7.1.1 Moore-Penrose pseudoinverse

Assuming the Moore-Penrose pseudoinverse, the gimbal rates that result from producing an arbitrary finite torque, T , are shown in Eq. (97).

$$\begin{bmatrix} \dot{\delta}_1 \\ \dot{\delta}_2 \\ \vdots \\ \dot{\delta}_n \end{bmatrix} = J^+ \frac{T}{h} \quad (97)$$

The torque, T , is separated into the three components, τ_x , τ_y , and τ_z , specifying a torque direction, and a torque magnitude, τ , enabling Eq. (97) to be simplified to Eq. (98).

$$\begin{bmatrix} \dot{\delta}_1 \\ \dot{\delta}_2 \\ \vdots \\ \dot{\delta}_n \end{bmatrix} = J^+ \begin{bmatrix} \tau_x \\ \tau_y \\ \tau_z \end{bmatrix} \frac{\tau}{h} \quad (98)$$

$$T = \begin{bmatrix} \tau_x \\ \tau_y \\ \tau_z \end{bmatrix} \tau$$

The gimbal rate for the i^{th} CMG in the array is shown in Eq. (99).

$$\dot{\delta}_i = [J^+(i, 1) \quad J^+(i, 2) \quad J^+(i, 3)] \begin{bmatrix} \tau_x \\ \tau_y \\ \tau_z \end{bmatrix} \frac{\tau}{h} \quad (99)$$

The gimbal rate is scaled linearly with the magnitude of the torque divided by the magnitude of the angular momentum of the CMGs in the array. For an arbitrary finite torque magnitude, the direction of torque that maximizes the magnitude of $\dot{\delta}_i$ is computed by solving the optimization problem shown in Eq. (100).

$$\max_{\tau_x, \tau_y, \tau_z} \left| [J^+(i, 1) \quad J^+(i, 2) \quad J^+(i, 3)] \begin{bmatrix} \tau_x \\ \tau_y \\ \tau_z \end{bmatrix} \right| \quad (100)$$

subject to: $\left\| \begin{bmatrix} \tau_x \\ \tau_y \\ \tau_z \end{bmatrix} \right\|_2 = 1$

Only the magnitude of δ_i is considered and not the direction, because it is assumed the CMGs have equal gimbal-rate capabilities in the positive and negative directions. The optimization is simplified by squaring the inner expression instead of taking the absolute value and by simplifying the l^2 -norm as shown in Eq. (101).

$$\max_{\tau_x, \tau_y, \tau_z} \left([J^+(i, 1) \quad J^+(i, 2) \quad J^+(i, 3)] \begin{bmatrix} \tau_x \\ \tau_y \\ \tau_z \end{bmatrix} \right)^2 \quad (101)$$

subject to: $\tau_x^2 + \tau_y^2 + \tau_z^2 = 1$

The optimization problem is solved using Lagrange multipliers. The Lagrange equation is shown in Eq. (102).

$$L = F(\tau_x, \tau_y, \tau_z) - \lambda g(\tau_x, \tau_y, \tau_z) \quad (102)$$

$$F(\tau_x, \tau_y, \tau_z) = \left([J^+(i, 1) \quad J^+(i, 2) \quad J^+(i, 3)] \begin{bmatrix} \tau_x \\ \tau_y \\ \tau_z \end{bmatrix} \right)^2$$

$$g(\tau_x, \tau_y, \tau_z) = \tau_x^2 + \tau_y^2 + \tau_z^2 - 1$$

From the Lagrange optimization, the maximum value of F is shown in Eq. (103).

$$F_{max} = J^+(i, 1)^2 + J^+(i, 2)^2 + J^+(i, 3)^2 \quad (103)$$

The stationary points that correspond to that maximum value are shown in Eqs. (104 - 109). Equations (104 - 106) correspond to one solution set. Equations (107 - 109) correspond to a second solution set.

$$\tau_{x_1} = \frac{J^+(i, 1)}{\sqrt{J^+(i, 1)^2 + J^+(i, 2)^2 + J^+(i, 3)^2}} \quad (104)$$

$$\tau_{y_1} = \frac{J^+(i, 2)}{\sqrt{J^+(i, 1)^2 + J^+(i, 2)^2 + J^+(i, 3)^2}} \quad (105)$$

$$\tau_{z_1} = \frac{J^+(i, 3)}{\sqrt{J^+(i, 1)^2 + J^+(i, 2)^2 + J^+(i, 3)^2}} \quad (106)$$

$$\tau_{x_2} = -\frac{J^+(i, 1)}{\sqrt{J^+(i, 1)^2 + J^+(i, 2)^2 + J^+(i, 3)^2}} \quad (107)$$

$$\tau_{y_2} = -\frac{J^+(i, 2)}{\sqrt{J^+(i, 1)^2 + J^+(i, 2)^2 + J^+(i, 3)^2}} \quad (108)$$

$$\tau_{z_2} = -\frac{J^+(i, 3)}{\sqrt{J^+(i, 1)^2 + J^+(i, 2)^2 + J^+(i, 3)^2}} \quad (109)$$

The torque directions defined by Eqs. (104 - 109) produce the largest gimbal-rate magnitude for a given torque magnitude. Both sets of solutions produce the same gimbal-rate magnitude. Thus, either can be chosen for the torque directions. For this derivation, the set shown in Eqs. (104 - 106) is chosen. The solutions from the Lagrange optimization for the i^{th} CMG are substituted into Eq. (99), yielding Eq. (110), where $\dot{\delta}_{i_{max}}$ represents the maximum gimbal-rate magnitude of the i^{th} CMG that can result from producing a finite torque in any direction.

$$\dot{\delta}_{i_{max}} = \frac{\tau}{h} \sqrt{J^+(i, 1)^2 + J^+(i, 2)^2 + J^+(i, 3)^2} \quad (110)$$

Using the same methodology, the maximum gimbal rate magnitudes for all CMGs in the array that can result from producing a torque in any direction are computed and shown in Eq. (111).

$$\dot{\Delta}_{max} = \frac{\tau}{h} W_{MP} \quad (111)$$

$$W_{MP} = \begin{bmatrix} \sqrt{J^+(1,1)^2 + J^+(1,2)^2 + J^+(1,3)^2} \\ \sqrt{J^+(2,1)^2 + J^+(2,2)^2 + J^+(2,3)^2} \\ \vdots \\ \sqrt{J^+(n,1)^2 + J^+(n,2)^2 + J^+(n,3)^2} \end{bmatrix}$$

Equation (111) is simplified by pulling the determinant out of the matrix W_{MP} .

$$W_{MP} = \frac{1}{\det(JJ^T)} \begin{bmatrix} \sqrt{A(1,1)^2 + A(1,2)^2 + A(1,3)^2} \\ \sqrt{A(2,1)^2 + A(2,2)^2 + A(2,3)^2} \\ \vdots \\ \sqrt{A(n,1)^2 + A(n,2)^2 + A(n,3)^2} \end{bmatrix} \quad (112)$$

$$A = J^T \text{adj}(JJ^T)$$

The maximum possible gimbal rate for any CMG that can result from producing a finite torque in any direction is $\|\dot{\Delta}_{max}\|_{\infty}$. The maximum torque the array can produce in any direction given the gimbal rate limitations is shown in Eq. (113).

$$T_{max} = \frac{\delta_{max}}{\|\dot{\Delta}_{max}\|_{\infty}} \tau = \frac{h\delta_{max}}{\|W_{MP}\|_{\infty}} \quad (113)$$

Equation (113) is normalized by the maximum torque magnitude any one CMG in the array can produce, yielding Eq. (114), which is TC for the case an arbitrary array architecture and the Moore-Penrose pseudoinverse steering law.

$$TC = \frac{1}{\|W_{MP}\|_{\infty}} \quad (114)$$

7.1.2 Four-CMG Box-90 and the Augmented Jacobian Method

The gimbal rates that result from producing an arbitrary finite torque, T , are shown in Eq. (115) for the case of the four-CMG box-90 and the augmented Jacobian steering law.

$$\begin{bmatrix} \dot{\delta}_1 \\ \dot{\delta}_2 \\ \dot{\delta}_3 \\ \dot{\delta}_4 \end{bmatrix} = J_t^{-1} \begin{bmatrix} \tau_x \\ \tau_y \\ \tau_z \\ 0 \end{bmatrix} \frac{\tau}{h} \quad (115)$$

$$T = \begin{bmatrix} \tau_x \\ \tau_y \\ \tau_z \end{bmatrix} \tau$$

The gimbal rate for the i^{th} CMG in the array is shown in Eq. (116).

$$\dot{\delta}_i = [J_t^{-1}(i, 1) \quad J_t^{-1}(i, 2) \quad J_t^{-1}(i, 3) \quad J_t^{-1}(i, 4)] \begin{bmatrix} \tau_x \\ \tau_y \\ \tau_z \\ 0 \end{bmatrix} \frac{\tau}{h} \quad (116)$$

The direction of torque that maximizes the magnitude of $\dot{\delta}_i$ is computed by solving Eq. (117).

$$\max_{\tau_x, \tau_y, \tau_z} \left([J_t^{-1}(i, 1) \quad J_t^{-1}(i, 2) \quad J_t^{-1}(i, 3)] \begin{bmatrix} \tau_x \\ \tau_y \\ \tau_z \end{bmatrix} \right)^2 \quad (117)$$

subject to: $\tau_x^2 + \tau_y^2 + \tau_z^2 = 1$

Using Lagrange multipliers, Eq. (117) is solved. The resulting Lagrange equation is shown in Eq. (118).

$$L = F(\tau_x, \tau_y, \tau_z) - \lambda g(\tau_x, \tau_y, \tau_z) \quad (118)$$

$$F(\tau_x, \tau_y, \tau_z) = \left([J_t^{-1}(i, 1) \quad J_t^{-1}(i, 2) \quad J_t^{-1}(i, 3)] \begin{bmatrix} \tau_x \\ \tau_y \\ \tau_z \end{bmatrix} \right)^2$$

$$g(\tau_x, \tau_y, \tau_z) = \tau_x^2 + \tau_y^2 + \tau_z^2 - 1$$

The maximum value of F is shown in Eq. (119).

$$F_{max} = J_t^{-1}(i, 1)^2 + J_t^{-1}(i, 2)^2 + J_t^{-1}(i, 3)^2 \quad (119)$$

The stationary points that correspond to that maximum value are shown in Eqs. (120 - 125). Equations (120 - 122) correspond to one solution set. Equations (123 - 125) correspond to a second solution set.

$$\tau_{x_1} = \frac{J_t^{-1}(i, 1)}{\sqrt{J_t^{-1}(i, 1)^2 + J_t^{-1}(i, 2)^2 + J_t^{-1}(i, 3)^2}} \quad (120)$$

$$\tau_{y_1} = \frac{J_t^{-1}(i, 2)}{\sqrt{J_t^{-1}(i, 1)^2 + J_t^{-1}(i, 2)^2 + J_t^{-1}(i, 3)^2}} \quad (121)$$

$$\tau_{z_1} = \frac{J_t^{-1}(i, 3)}{\sqrt{J_t^{-1}(i, 1)^2 + J_t^{-1}(i, 2)^2 + J_t^{-1}(i, 3)^2}} \quad (122)$$

$$\tau_{x_2} = -\frac{J_t^{-1}(i, 1)}{\sqrt{J_t^{-1}(i, 1)^2 + J_t^{-1}(i, 2)^2 + J_t^{-1}(i, 3)^2}} \quad (123)$$

$$\tau_{y_2} = -\frac{J_t^{-1}(i, 2)}{\sqrt{J_t^{-1}(i, 1)^2 + J_t^{-1}(i, 2)^2 + J_t^{-1}(i, 3)^2}} \quad (124)$$

$$\tau_{z_2} = -\frac{J_t^{-1}(i, 3)}{\sqrt{J_t^{-1}(i, 1)^2 + J_t^{-1}(i, 2)^2 + J_t^{-1}(i, 3)^2}} \quad (125)$$

Because the gimbal rate limitation is assumed to apply equally to positive and negative rotations, either solution set yields the same result. For this derivation, Eqs. (120 - 122) are used. Eqs. (120 - 122), are substituted in to Eq. (116), yielding Eq. (126).

$$\delta_{i_{max}} = \frac{\tau}{h} \sqrt{J_t^{-1}(i, 1)^2 + J_t^{-1}(i, 2)^2 + J_t^{-1}(i, 3)^2} \quad (126)$$

The maximum gimbal rate magnitudes for all CMGs are shown in Eq. (127).

$$\dot{\Delta}_{max} = \frac{\tau}{h} W_{CB} \quad (127)$$

$$W_{CB} = \begin{bmatrix} \sqrt{J_t^{-1}(1,1)^2 + J_t^{-1}(1,2)^2 + J_t^{-1}(1,3)^2} \\ \sqrt{J_t^{-1}(2,1)^2 + J_t^{-1}(2,2)^2 + J_t^{-1}(2,3)^2} \\ \sqrt{J_t^{-1}(3,1)^2 + J_t^{-1}(3,2)^2 + J_t^{-1}(3,3)^2} \\ \sqrt{J_t^{-1}(4,1)^2 + J_t^{-1}(4,2)^2 + J_t^{-1}(4,3)^2} \end{bmatrix}$$

The maximum torque the array can produce in any direction given the gimbal rate limitations is shown in Eq. (128).

$$T_{max} = \frac{\dot{\delta}_{max}}{\|\dot{\Delta}_{max}\|_{\infty}} \tau = \frac{h\dot{\delta}_{max}}{\|W_{CB}\|_{\infty}} \quad (128)$$

Equation (128) is normalized by the maximum torque magnitude any one CMG in the array can produce, yielding Eq. (129), which is *TC* for the case of a four-CMG box-90 array and the augmented Jacobian steering law.

$$TC = \frac{1}{\|W_{CB}\|_{\infty}} \quad (129)$$

7.1.3 Four-CMG Box-90 and the Local Gradient Steering Law

For the case of the four-CMG box-90 array and the LG steering law, the same methodology is used to derive *TC*. For the LG steering law, the gimbal rates for all of the CMGs in the array to produce an arbitrary finite torque are shown in Eq. (130).

$$\begin{bmatrix} \dot{\delta}_1 \\ \dot{\delta}_2 \\ \dot{\delta}_3 \\ \dot{\delta}_4 \end{bmatrix} = J^+ T + \dot{\Delta}_n \quad (130)$$

$$\dot{\Delta}_n = k(I_{4 \times 4} - J^+ J) d^T$$

The gimbal rate for the i^{th} CMG is shown in Eq. (131).

$$\dot{\delta}_i = [J^+(i, 1) \quad J^+(i, 2) \quad J^+(i, 3)] \begin{bmatrix} \tau_x \\ \tau_y \\ \tau_z \end{bmatrix} \frac{\tau}{h} + \dot{\Delta}_n(i, 1) \quad (131)$$

The torque direction that maximizes the magnitude of $\dot{\delta}_i$ is computed by first solving the optimization problem shown in Eq. (132).

$$\begin{aligned} \max_{\tau_x, \tau_y, \tau_z} & \left(\left\| [J^+(i, 1) \quad J^+(i, 2) \quad J^+(i, 3)] \begin{bmatrix} \tau_x \\ \tau_y \\ \tau_z \end{bmatrix} \right\| \right) \\ \text{subject to:} & \left\| \begin{bmatrix} \tau_x \\ \tau_y \\ \tau_z \end{bmatrix} \right\|_2 = 1 \end{aligned} \quad (132)$$

The optimization yields two optimal solutions sets: one corresponding to Eqs. (133 - 135) and one corresponding to Eq. (136 - 138).

$$\tau_{x_1} = \frac{J^+(i, 1)}{\sqrt{J^+(i, 1)^2 + J^+(i, 2)^2 + J^+(i, 3)^2}} \quad (133)$$

$$\tau_{y_1} = \frac{J^+(i, 2)}{\sqrt{J^+(i, 1)^2 + J^+(i, 2)^2 + J^+(i, 3)^2}} \quad (134)$$

$$\tau_{z_1} = \frac{J^+(i, 3)}{\sqrt{J^+(i, 1)^2 + J^+(i, 2)^2 + J^+(i, 3)^2}} \quad (135)$$

$$\tau_{x_2} = -\frac{J^+(i, 1)}{\sqrt{J^+(i, 1)^2 + J^+(i, 2)^2 + J^+(i, 3)^2}} \quad (136)$$

$$\tau_{y_2} = -\frac{J^+(i, 2)}{\sqrt{J^+(i, 1)^2 + J^+(i, 2)^2 + J^+(i, 3)^2}} \quad (137)$$

$$\tau_{z_2} = -\frac{J^+(i, 3)}{\sqrt{J^+(i, 1)^2 + J^+(i, 2)^2 + J^+(i, 3)^2}} \quad (138)$$

Both sets of solutions yield the same optimal value for Eq. (132). Substituting both sets of solutions into Eq. (131), yields Eq. (139) where either the first term can be positive or negative depending on the optimal solution set used.

$$\delta_{i_{max}} = \pm \frac{\tau}{h} \sqrt{J^+(i, 1)^2 + J^+(i, 2)^2 + J^+(i, 3)^2} + \dot{\Delta}_n(i, 1) \quad (139)$$

Unlike the derivation of TC for the four-CMG box-90 array and the augmented Jacobian steering law, both sets of solutions do not yield the same value for the magnitude of δ_i . Instead, due to the addition of $\dot{\Delta}_n(i, 1)$, if $\dot{\Delta}_n(i, 1)$ is not zero, then δ_i is maximized when both of the two terms in Eq. (139) have the same sign. If $\dot{\Delta}_n(i, 1)$ is zero, then the sign of the first term can be either positive or negative. Thus, Eq. (139) can be simplified to Eq. (140).

$$\delta_{i_{max}} = \frac{\tau}{h} \sqrt{J^+(i, 1)^2 + J^+(i, 2)^2 + J^+(i, 3)^2} + |\dot{\Delta}_n(i, 1)| \quad (140)$$

Using the same methodology, the maximum gimbal rate magnitude that can result from the array producing an finite torque in any direction is computed for each CMG in the array, yielding Eq. (141).

$$\dot{\Delta}_{max} = \begin{bmatrix} \frac{\tau}{h} \sqrt{J^+(1,1)^2 + J^+(1,2)^2 + J^+(1,3)^2} + |\dot{\Delta}_n(1, 1)| \\ \frac{\tau}{h} \sqrt{J^+(2, 1)^2 + J^+(2, 2)^2 + J^+(2, 3)^2} + |\dot{\Delta}_n(2, 1)| \\ \frac{\tau}{h} \sqrt{J^+(3, 1)^2 + J^+(3, 2)^2 + J^+(3, 3)^2} + |\dot{\Delta}_n(3, 1)| \\ \frac{\tau}{h} \sqrt{J^+(4, 1)^2 + J^+(4, 2)^2 + J^+(4, 3)^2} + |\dot{\Delta}_n(4, 1)| \end{bmatrix} \quad (141)$$

The maximum torque the array can produce in all possible directions is shown in Eq. (142).

$$T_{max} = \min \left(\begin{array}{c} \frac{h\dot{\delta}_{max} - h|\dot{\Delta}_n(1, 1)|}{\sqrt{J^+(1,1)^2 + J^+(1,2)^2 + J^+(1,3)^2}} \\ \frac{h\dot{\delta}_{max} - h|\dot{\Delta}_n(2, 1)|}{\sqrt{J^+(2,1)^2 + J^+(2,2)^2 + J^+(2,3)^2}} \\ \frac{h\dot{\delta}_{max} - h|\dot{\Delta}_n(3, 1)|}{\sqrt{J^+(3,1)^2 + J^+(3,2)^2 + J^+(3,3)^2}} \\ \frac{h\dot{\delta}_{max} - h|\dot{\Delta}_n(4, 1)|}{\sqrt{J^+(4,1)^2 + J^+(4,2)^2 + J^+(4,3)^2}} \end{array} \right) \quad (142)$$

Equation (142) is normalized by dividing by the maximum torque magnitude each CMG in the array can produce, yielding Eq. (143).

$$TC = \min \left(\begin{array}{c} 1 - \frac{1}{\dot{\delta}_{max}} |\dot{\Delta}_n(1, 1)| \\ \frac{1 - \frac{1}{\dot{\delta}_{max}} |\dot{\Delta}_n(1, 1)|}{\sqrt{J^+(1,1)^2 + J^+(1,2)^2 + J^+(1,3)^2}} \\ 1 - \frac{1}{\dot{\delta}_{max}} |\dot{\Delta}_n(2, 1)| \\ \frac{1 - \frac{1}{\dot{\delta}_{max}} |\dot{\Delta}_n(2, 1)|}{\sqrt{J^+(2,1)^2 + J^+(2,2)^2 + J^+(2,3)^2}} \\ 1 - \frac{1}{\dot{\delta}_{max}} |\dot{\Delta}_n(3, 1)| \\ \frac{1 - \frac{1}{\dot{\delta}_{max}} |\dot{\Delta}_n(3, 1)|}{\sqrt{J^+(3,1)^2 + J^+(3,2)^2 + J^+(3,3)^2}} \\ 1 - \frac{1}{\dot{\delta}_{max}} |\dot{\Delta}_n(4, 1)| \\ \frac{1 - \frac{1}{\dot{\delta}_{max}} |\dot{\Delta}_n(4, 1)|}{\sqrt{J^+(4,1)^2 + J^+(4,2)^2 + J^+(4,3)^2}} \end{array} \right) \quad (143)$$

7.2 Proofs of Global Optimality for Planar Array Constraints

Proofs are provided to verify the global optimality of the gimbal-angle constraint functions discussed in Section 3.2. None of the proofs provided proves uniqueness; many solutions may exist that achieve the same performance. For all proofs, angular momentum is assumed to be positive and only have a projection onto one axis. As stated in Section 3.2, this simplification does not limit the generality of the proofs. The axis that the angular momentum is projected along is

called the $\hat{\mathbf{x}}$ axis. The desired array angular momentum along the $\hat{\mathbf{x}}$ axis is referred to as H_d . For the remaining proofs, H_d is a scalar and not a matrix. The axis perpendicular to the $\hat{\mathbf{x}}$ axis that lies in the plane is referred to as the $\hat{\mathbf{y}}$ axis. The tilde above angular-momentum values indicate a normalized angular-momentum value computed by dividing the angular-momentum value by h . The projection each CMG has onto each axis is shown in Eqs. (144, 145).

$$\tilde{h}_{y_i} = \sin(\delta_i) \quad (144)$$

$$\tilde{h}_{x_i} = \cos(\delta_i) \quad (145)$$

To prove the optimality of the provided gimbal-angle constraint functions, first, the constraint functions are proven to optimize Eq. (146) for all angular-momentum states.

$$R = \min_{\delta_1, \delta_2, \dots, \delta_n} \|W_{MP}\|_2 \quad (146)$$

$$\text{subject to: } \cos(\delta_1) + \cos(\delta_2) + \dots + \cos(\delta_n) = \tilde{H}_d,$$

$$\sin(\delta_1) + \sin(\delta_2) + \dots + \sin(\delta_n) = 0$$

$$W_{MP} = \frac{1}{\det(JJ^T)} \begin{bmatrix} \sqrt{A(1,1)^2 + A(1,2)^2} \\ \sqrt{A(2,1)^2 + A(2,2)^2} \\ \vdots \\ \sqrt{A(n,1)^2 + A(n,2)^2} \end{bmatrix}$$

Substituting the Jacobian for a planar array shown in Eq. (19) into Eq. (146) yields Eq. (147).

$$R = \min_{\delta_1, \delta_2, \dots, \delta_n} \sqrt{\frac{n}{\det(JJ^T)}} \quad (147)$$

$$\text{subject to: } \cos(\delta_1) + \cos(\delta_2) + \dots + \cos(\delta_n) = \tilde{H}_d,$$

$$\sin(\delta_1) + \sin(\delta_2) + \dots + \sin(\delta_n) = 0$$

$$\det(JJ^T) = CC^T(n - CC^T) - SC^TSC^T$$

The denominator, $\det(JJ^T)$, shown in Eq. (147) is often referred to as the singularity measure of the array. The provided gimbal-angle constraint functions are proven to maximize the singularity measure, and thus minimizing Eq. (147) for all angular-momentum states. The resulting value for R represents the minimum radius of a hypersphere of the elements of W_{MP} that intersects the set W_{con} , which is the set of elements of W_{MP} that satisfies the angular-momentum constraints applied to the optimization.

The matrix W_{sol} , which results from substituting the provided gimbal-angle constraint functions into W_{MP} , is then shown to be equal to the coordinates of the vertices of a hypercube that is inscribed within a hypersphere of radius R . Because W_{sol} represents the vertices of an inscribed hypercube, reducing the infinity norm of W_{sol} is equivalent to reducing the longest edge of the hypercube. This reduction requires the magnitude of all values of W_{sol} to be reduced, resulting in a hyperrectangle that does not intersect the set W_{con} . Therefore, the provided solutions globally maximize the torque capability of the array.

The first step of the proof is to show that the provided gimbal-angle constraint functions maximize the singularity measure and thus minimize $\|W_{MP}\|_2$. The methodology for proving the provided constraint functions globally maximize the singularity measure results from there being two main expressions in the singularity measure: $CC^T(n - CC^T)$ and $-SC^TSC^T$. The following proofs verify that the provided gimbal-angle constraint functions globally optimize both $CC^T(n - CC^T)$ and $-SC^TSC^T$ independently for every angular-momentum state. Therefore, they globally optimize the singularity measure for every angular-momentum state.

The global maximum for $CC^T(n - CC^T)$ when the angular momentum is not constrained is analytically determined for CC^T and is shown in Eq. (148)

$$CC^T = \frac{n}{2} \quad (148)$$

If the gimbal-angle constraint functions achieve the equality in Eq. (148), the constraint functions globally optimize $CC^T(n - CC^T)$. However, an array is not capable of achieving the equality in Eq. (148) for all magnitudes of \tilde{H}_d . This is shown by the fact that when \tilde{H}_d is equal to n , CC^T must be equal to n , which does not satisfy Eq. (148).

The optimal solution is split into two discrete angular-momentum regions: the static region and the declining region. While the array is operating in the static angular-momentum region, the array achieves the equality shown in Eq. (148). While operating in the declining momentum region, the array maximizes $CC^T(n - CC^T)$ but is unable to achieve the equality shown in Eq. (148). The expression $CC^T(n - CC^T)$ is concave with respect to CC^T , and the value of CC^T is greater than or equal to $\frac{n}{2}$, so maximizing $CC^T(n - CC^T)$ is equivalent to minimizing CC^T .

The proof of global optimality of the singularity measure for arrays is broken into three parts. The first part of the proof verifies that the provided gimbal-angle constraint function minimizes CC^T in the declining angular-momentum region. To prove that the provided gimbal and constraint function minimize CC^T in the declining region, the gimbal-angle sets that minimize CC^T for any angular-momentum state are determined. This optimal solution has two purposes: 1) the solution enables the calculation of \tilde{H}_c by determining the angular-momentum state at which the solution results in the equality shown in Eq. (148); and 2) the solution represents the optimal gimbal-angle set for the declining angular-momentum region, so the solution should match the gimbal-angle

constraint functions provided in Section 3.2. The second part of the proof verifies that the gimbal-angle constraint functions globally optimize $CC^T(n - CC^T)$ in the static region by substituting the constraint functions into CC^T and showing that the resulting values are $\frac{n}{2}$. The third part of the proof verifies that the gimbal-angle constraint functions for both angular-momentum regions globally maximize $-SC^TSC^T$. By substituting the solutions in to $-SC^TSC^T$, the expression evaluates to zero for all provided constraint functions. The three sections of the proof verify that the gimbal-angle constraint functions globally maximize the singularity measure in each angular-momentum region.

7.2.1 Arrays with an Even Number of CMGs Greater Than Three

The gimbal-angle constraint functions for arrays with an even number of CMGs greater than three are proven to maximize torque capability. The first step of the proof is to determine the gimbal-angle sets that minimize CC^T for any angular-momentum state, which is determined by solving the optimization shown in Eq. (149) for all angular-momentum states.

$$\min_{\delta_1, \delta_2, \dots, \delta_n} CC^T \quad (149)$$

$$\text{subject to: } \cos(\delta_1) + \cos(\delta_2) + \dots + \cos(\delta_n) = \tilde{H}_d,$$

$$\sin(\delta_1) + \sin(\delta_2) + \dots + \sin(\delta_n) = 0$$

To simplify the optimization, the cosine and sine values are replaced with \tilde{h}_x and \tilde{h}_y , respectively, as shown in Eq. (150).

$$\min_{\delta_1, \delta_2, \dots, \delta_n} \tilde{h}_{x_1}^2 + \tilde{h}_{x_2}^2 + \dots + \tilde{h}_{x_n}^2 \quad (150)$$

$$\text{subject to: } \tilde{h}_{x_1} + \tilde{h}_{x_2} + \dots + \tilde{h}_{x_n} = \tilde{H}_d,$$

$$\begin{aligned}\tilde{h}_{y_1} + \tilde{h}_{y_2} + \cdots + \tilde{h}_{y_n} &= 0, \\ \tilde{h}_{x_1}^2 + \tilde{h}_{y_1}^2 &= 1, \tilde{h}_{x_2}^2 + \tilde{h}_{y_2}^2 = 1, \dots, \tilde{h}_{x_n}^2 + \tilde{h}_{y_n}^2 = 1\end{aligned}$$

The optimal gimbal-angle set is found using Lagrange multipliers. The globally minimizing, but non-unique, solution for this optimization is shown in Eqs. (151, 152), which match the provided gimbal-angle constraint functions in Section 3.2.1. In the solution, all \tilde{h}_{x_i} values are assumed to have the same sign. The same minimizing value is achieved for Eq. (150) if the assumption is not made. However, while minimizing Eq. (150), the solution should also maximize \tilde{H}_c , which is achieved by having the sign of all \tilde{h}_{x_i} values the same.

$$\delta_{1,2,\dots,\frac{n}{2}} = \cos^{-1}\left(\frac{\tilde{H}_d}{n}\right) \quad (151)$$

$$\delta_{\frac{n}{2}+1,\frac{n}{2}+2,\dots,n} = -\delta_{1,2,\dots,\frac{n}{2}} \quad (152)$$

The critical angular momentum is calculated using these solutions and is shown in Eq. (153). The critical angular momentum matches the critical angular momentum provided in Section 3.2.

$$\tilde{H}_c = \frac{n}{\sqrt{2}} \quad (153)$$

Next, the provided gimbal-angle constraint functions are shown to globally maximize $CC^T(n - CC^T)$ for the static region. Substituting the provided gimbal-angle constraint functions for the static angular-momentum region from Eqs. (24 - 28) into CC^T yields $\frac{n}{2}$, proving that the provided gimbal-angle constraint functions globally maximize $CC^T(n - CC^T)$ in the static region.

Next, the gimbal-angle constraint functions are proven to globally maximize $-SC^TSC^T$. The gimbal-angle constraint functions for the static and declining regions are substituted into

$-SC^TSC^T$, which yields zero for both regions, so the gimbal-angle constraint functions are globally optimal for both angular-momentum regions.

The proofs offered here verify that the gimbal-angle constraint functions shown in Eqs. (24 - 28) globally optimize the singularity measure for all angular-momentum states for any even number of CMGs greater than three.

Next, the provided gimbal-angle constraint functions are proven to optimize torque capability. First, the value for R is calculated for both angular-momentum regions, which is shown in Eq. (154).

$$R = \begin{cases} \sqrt{\frac{4}{n}}, 0 \leq \tilde{H}_d < \frac{n}{\sqrt{2}} \\ \sqrt{\frac{n^3}{\tilde{H}_d^2(n^2 - \tilde{H}_d^2)}}, \frac{n}{\sqrt{2}} \leq \tilde{H}_d \leq n \end{cases} \quad (154)$$

Substituting the provided gimbal-angle constraints into W_{MP} yields Eq. (155).

$$W_{sol} = \left\{ \begin{array}{l} \left[\begin{array}{c} 2 \\ n \\ 2 \\ n \\ \vdots \\ 2 \\ n \end{array} \right], 0 \leq \tilde{H}_d < \frac{n}{\sqrt{2}} \\ \left[\begin{array}{c} \sqrt{\frac{n^2}{\tilde{H}_d^2(n^2 - \tilde{H}_d^2)}} \\ \sqrt{\frac{n^2}{\tilde{H}_d^2(n^2 - \tilde{H}_d^2)}} \\ \vdots \\ \sqrt{\frac{n^2}{\tilde{H}_d^2(n^2 - \tilde{H}_d^2)}} \end{array} \right], \frac{n}{\sqrt{2}} \leq \tilde{H}_d \leq n \end{array} \right. \quad (155)$$

For each angular-momentum region, the values of W_{sol} represent a single vertex of a hypercube. However, in Section 7.1.1 it is shown that there are two possible solutions sets for each value of W_{MP} , both with the same magnitude but opposite sign. In Section 7.1.1, only the positive solutions are considered, simplifying the expression. However, because of the two solution sets, the values of W_{MP} could be positive or negative. Incorporating these negative solutions, shown in Eqs. (107 - 109), into W_{sol} results in Eq. (156).

$$W_{sol} = \left\{ \begin{array}{l} \begin{array}{l} \pm \frac{2}{n} \\ \pm \frac{2}{n} \\ \vdots \\ \pm \frac{2}{n} \end{array}, 0 \leq \tilde{H}_d < \frac{n}{\sqrt{2}} \\ \begin{array}{l} \pm \sqrt{\frac{n^2}{\tilde{H}_d^2(n^2 - \tilde{H}_d^2)}} \\ \pm \sqrt{\frac{n^2}{\tilde{H}_d^2(n^2 - \tilde{H}_d^2)}} \\ \vdots \\ \pm \sqrt{\frac{n^2}{\tilde{H}_d^2(n^2 - \tilde{H}_d^2)}} \end{array}, \frac{n}{\sqrt{2}} \leq \tilde{H}_d \leq n \end{array} \right. \quad (156)$$

For both angular-momentum regions, the values of W_{sol} represent the vertices of a hypercube. The two-norm of W_{sol} is equal to R for both angular-momentum regions, proving that the provided gimbal-angle constraint functions shown in Eqs. (24 - 28) globally optimize the torque capability of any even number of CMGs greater than three for any angular momentum.

7.2.2 Arrays with an Odd Number of CMGs More Than Three

For arrays with an odd number of CMGs greater than three, the constraints are proven to be globally optimal in the static angular-momentum region, but not in the declining angular-momentum region. For brevity, a proof of global optimality in the static region is only shown for the arrays with an odd number of CMGs greater than seven. The same methodology is used to prove optimality for the constraints for arrays with five and seven CMGs.

To prove optimality of Eqs. (43 - 48), first the provided constraint functions are shown to maximize the singularity measure and thus minimize Eq. (147). The provided gimbal-angle

constraint functions from Eqs. (43 - 48) are substituted into CC^T and $-SC^TSC^T$, yielding $\frac{n}{2}$ and zero, respectively, proving that the provided constraint function globally minimizes $\|W_{MP}\|_2$ in the static region. The corresponding value for R for the static region is shown in Eq. (157).

$$R = \sqrt{\frac{4}{n}}, 0 \leq \tilde{H}_d < 1 + \sqrt{\frac{(n-1)(n-2)}{2}} \quad (157)$$

Substituting provided constraint functions into W_{MP} yields Eq. (158).

$$W_{sol} = \begin{bmatrix} 2 \\ \frac{2}{n} \\ 2 \\ \frac{2}{n} \\ \vdots \\ 2 \\ \frac{2}{n} \end{bmatrix}, 0 \leq \tilde{H}_d < 1 + \sqrt{\frac{(n-1)(n-2)}{2}} \quad (158)$$

The values of W_{sol} represent a single vertex of a hypercube. However, the values can either be positive or negative depending on the solution set used during the derivation of W_{MP} , as show in Section 7.1.1. Thus, Eq. (158) can be rewritten as Eq. (159).

$$W_{sol} = \begin{bmatrix} \pm 2 \\ \pm \frac{2}{n} \\ \pm 2 \\ \pm \frac{2}{n} \\ \vdots \\ \pm 2 \\ \pm \frac{2}{n} \end{bmatrix}, 0 \leq \tilde{H}_d < 1 + \sqrt{\frac{(n-1)(n-2)}{2}} \quad (159)$$

The values of W_{sol} represent the vertices of a hypercube. The two-norm of W_{sol} is equal to R , proving that the provided gimbal-angle constraint functions shown in Eqs. (43 - 48) globally optimize the torque capability of any odd number of CMGs greater than seven for any angular momentum within the static region.

Numerical evidence for the global optimality of the provided gimbal-angle constraint functions for the declining angular-momentum region for arrays with five, seven, nine, and eleven CMGs is provided. For each array, the value of $\|W_{MP}\|_\infty$ computed using the provided gimbal-angle constraint function is shown to be equal to the minimum value of $\|W_{MP}\|_\infty$, computed using a numerical optimizer for a set of angular-momentum states within the declining region.

A sequential quadratic programming (SQP) optimizer is selected as the numerical optimization technique. The SQP optimizer computes a locally optimal gimbal-angle set that minimizes $\|W_{MP}\|_\infty$ for a given angular-momentum state. To find an estimate of the global minimum of $\|W_{MP}\|_\infty$, the SQP optimizer is run iteratively with different initial gimbal-angle sets. The initial gimbal-angle sets are selected from a discretized set of gimbal angles. The discretized set of gimbal angles is created by discretizing each gimbal angle, which spans from 0 to 2π , and creating a combination of all the gimbal angles. The gimbal angles are discretized into segments of 0.2 rad, 0.2 rad, 0.3 rad, and 0.5 rad for arrays with five, seven, nine, and eleven CMGs, respectively. The discretization becomes coarser as the number of CMGs increases to ensure that the optimization remains computationally tractable.

The iterative optimizer is used to compute the minimum value for $\|W_{MP}\|_\infty$ for angular momentums spanning the range shown in Eq. (160). The angular-momentum range is discretized into segments of 0.025.

$$\tilde{H}_{range} = \left[1 + \sqrt{\frac{(n-1)(n-2)}{2}}, 0.99n \right] \quad (160)$$

The maximum angular momentum tested is $0.99n$ and not n , because as the array's angular momentum increases beyond $0.99n$ towards saturation, the numerical optimizer becomes less stable, resulting in less reliable numerical solutions. The constraint tolerance and optimality tolerance for the optimization is selected as 1×10^{-6} .

Figures 37 - 40 show the numerically computed minimum value for $\|W_{MP}\|_{\infty}$ minus the value for $\|W_{MP}\|_{\infty}$ computed using the provided gimbal-angle constraint functions for arrays with five, seven, nine, and eleven CMGs.

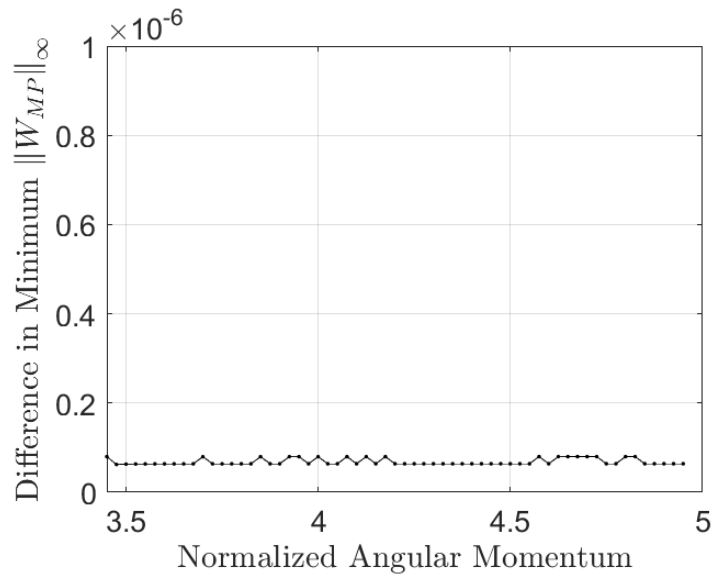


Figure 37. $\|W_{MP}\|_{\infty}$ calculated using the the SQP numerical optimizer minus $\|W_{MP}\|_{\infty}$ calculated using the provided constraint functions for arrays with five CMGs.

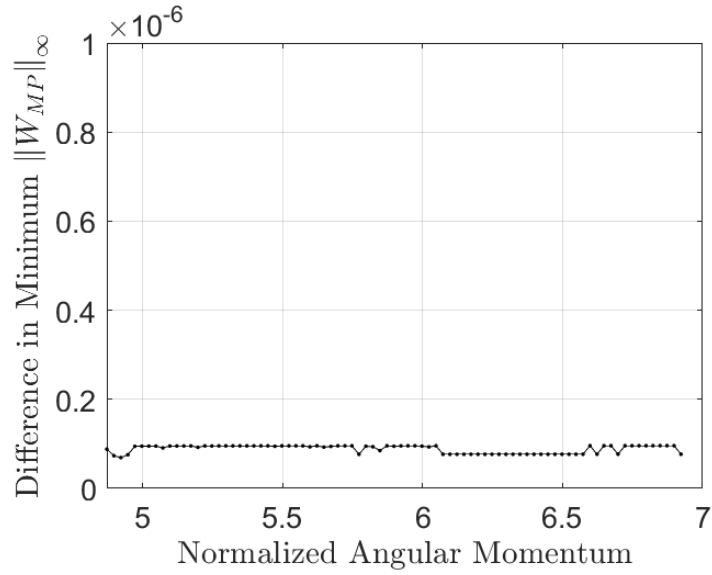


Figure 38. $\|W_{MP}\|_\infty$ calculated using the the SQP numerical optimizer minus $\|W_{MP}\|_\infty$ calculated using the provided constraint functions for arrays with seven CMGs.

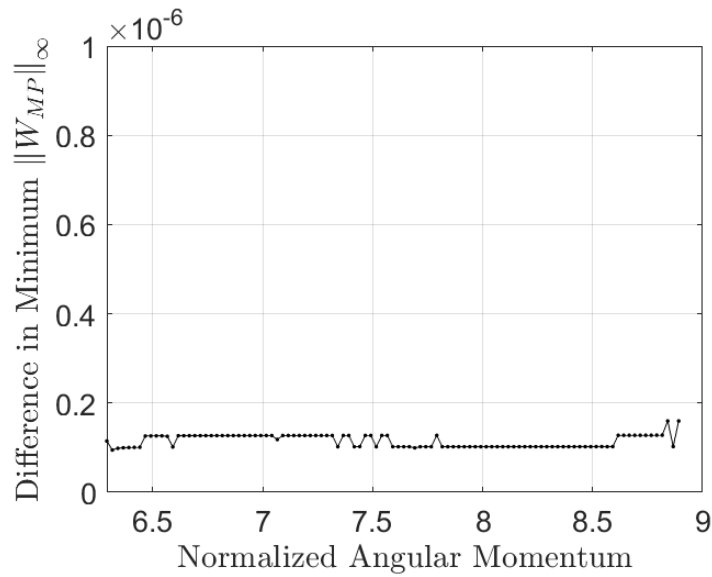


Figure 39. $\|W_{MP}\|_\infty$ calculated using the the SQP numerical optimizer minus $\|W_{MP}\|_\infty$ calculated using the provided constraint functions for arrays with nine CMGs.

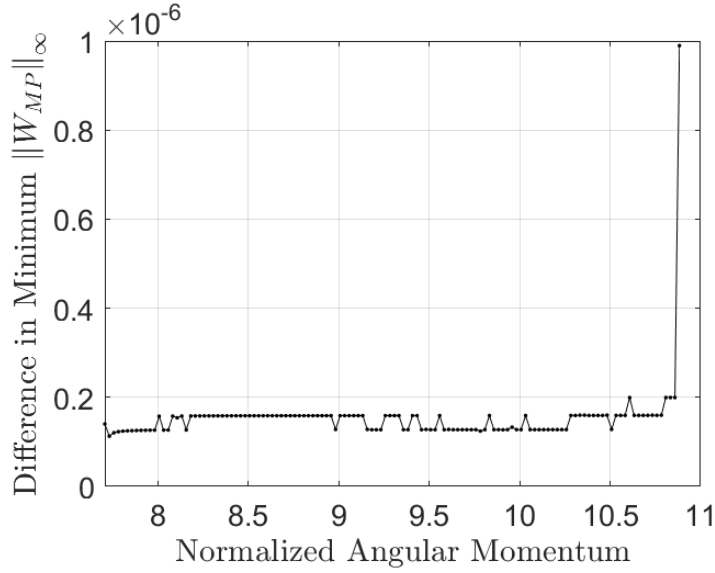


Figure 40. $\|W_{MP}\|_\infty$ calculated using the the SQP numerical optimizer minus $\|W_{MP}\|_\infty$ calculated using the provided constraint functions for arrays with eleven CMGs.

Figures 37 - 40 show that the numerically calculated minimum value for $\|W_{MP}\|_\infty$ is always within the tolerance of the optimization of the analytically computed value for $\|W_{MP}\|_\infty$ using the provided gimbal-angle constraint function. The numerical results provide evidence that the provided gimbal-angle constraint functions globally optimize torque capability for the declining angular-momentum region.

7.3 Spherical Constraint Function for Four-CMG Box-90 Array

The spherical constraint function shown in Eq. (55) offered the second greatest performance of all evaluated constraint function formulations. Using the spherical constraint, an expression for Ψ is developed using the same methodology as discussed in Section 4.2. The resulting constraint function is shown in Eqs. (161, 162).

$$\tilde{H}_{x_1} - \frac{\tilde{H}_x - \Psi}{2} = 0 \quad (161)$$

$$\Psi = b \sqrt{1 - \left(\frac{\tilde{H}_x}{2}\right)^2 - \left(\frac{\tilde{H}_y}{2}\right)^2 - \left(\frac{\tilde{H}_z}{2}\right)^2} + P(\tilde{H}_x) \quad (162)$$

$$P(\tilde{H}_x) = \frac{1}{2^5} \tilde{H}_x^8 - \frac{3}{20} \tilde{H}_x^6 + \frac{9}{40} \tilde{H}_x^4$$

$$\tilde{H}_x = \cos(\delta_1) + \cos(\delta_2) + \cos(\delta_3) + \cos(\delta_4)$$

$$\tilde{H}_{x_1} = \cos(\delta_1) + \cos(\delta_2)$$

$$\tilde{H}_y = \sin(\delta_1) + \sin(\delta_2)$$

$$\tilde{H}_z = \sin(\delta_3) + \sin(\delta_4)$$

$$b = \frac{4\sqrt{6}}{3}$$

The performance of this constraint function is shown in Figure 41. As discussed in Section 4.2, the minimum TC at most angular-momentum magnitudes is greater than the what is achieved using the cubic constraint function provided above. However, the constrained angular-momentum envelope is limited to a sphere of $2h$, which is smaller than what is achieved using the cubic constraint function.

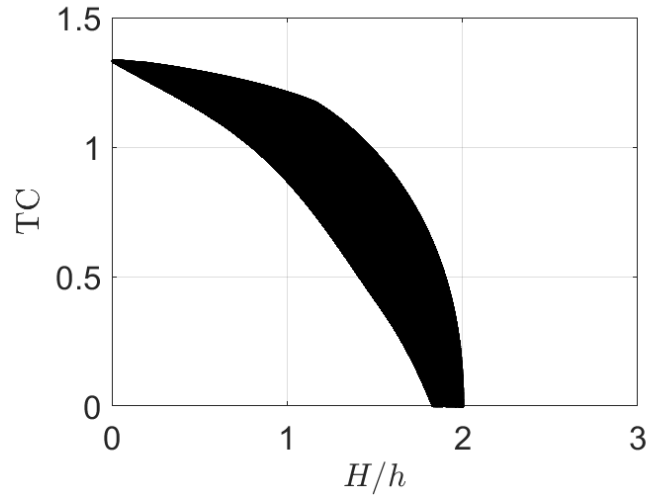


Figure 41. Spherical constraint performance.

7.4 PETER's Chassis Shape

The chassis shape has three main effects on the mobility of the rover. First, the chassis shape dictates the terrain on which the rover can remain static, which dictates the traversable terrain. If the rover cannot remain static on an incline or obstacle without actuator input, then the terrain is not considered traversable, because if the actuator input cannot be applied due to power failure or actuator limitations, the rover will roll uncontrolled, which could potentially harm the rover. Second, the chassis shape dictates the robustness of the rover to disturbance torques and off-axis torques from the CMG. The terrain's terra-mechanical properties will not be known perfectly before operation, so it is likely large disturbances will be acting on the body during a step, which can perturb the rover off its desired trajectory. Thus, the rover should be robust to off-axis torques to ensure predictable motion of the rover. Additionally, to enable the single CMG array to actuate the rover, the chassis must be robust to off-axis CMG torques. Third, the chassis shape effects the

amount of torque required to make a step. To determine the chassis that enables the greatest mobility on extreme terrains, the three factors listed above are used to compare chassis shapes.

For the analysis of the chassis shape, three simplifications are made. First, only the platonic solids are analyzed. By analyzing this small set of shapes, insight can be gained in how chassis shape effects the rover’s performance, which can aid in future research on optimal chassis shape. Second, it is assumed that the center of mass of the rover is at the geometric center. Third, it is assumed that the translation of spikes in contact with the surface are constrained to have no translation. Fourth, it is assumed that the CMG will be able to cancel out the disturbance torques about \hat{r} . During operation, as discussed in Section 5.4.1, the CMG is constrained to be capable of applying torque in the \hat{r} direction, enabling the CMG to cancel bounded disturbance torques. As a result of the last two assumptions, only disturbances about \hat{N} are considered in the comparison.

From the geometry, the slopes on which each platonic solid can remain static are shown in Table 8. From Table 8, it is clear that the tetrahedron is the most stable of all the platonic solids.

Table 8. Maximum slope each chassis can remain static on.

Tetrahedron	Cube	Octahedron	Dodecahedron	Icosahedron
54.7 degrees	45 degrees	35.3 degrees	31.7 degrees	20.9 degrees

For the chassis design it is desirable to increase the robustness of the rover to off-axis torques. However, by increasing the robustness, the amount of torque the array needs to produce to take a step increases, along with the amount of off-axis torque produced by the CMG. To effectively compare chassis shapes based on both criteria, the two criteria are included into one expression as shown in Eq. (163), where τ_r is the torque about \hat{r} required to make a step and τ_{dist} is the minimum disturbance torque about \hat{N} required to cause fewer than two spikes to be in contact with the surface.

$$\eta = \frac{\tau_r}{\tau_{dist}} \quad (163)$$

Both τ_r and τ_{dist} are dependent on the trajectory the rover takes to make a step. For each chassis shape, there is no general trajectory for a step, making the comparison difficult.

Because the dynamic terms of τ_r and τ_{dist} are relatively small compared to the gravity effects, the rover can be assumed to be static, which eliminates the dependency on trajectory, resulting in τ_r and τ_{dist} being dependent only on the orientation of the rover. For comparison, the rover is assumed to be in the orientation where there is no rotation about $\hat{\mathbf{N}}$, and the vector $\mathbf{r}^{cm/o}$ is perpendicular to the gravity vector, which maximizes τ_r and τ_{dist} . Applying these simplifications yield the values of η for the regular polyhedral shown in Table 9. The smaller values of η indicate a greater robustness to disturbances without requiring a large amount of torque to step.

Table 9. Ratio of required torque to step to the maximum allowable disturbance torque.

Tetrahedron	Cube	Octahedron	Dodecahedron	Icosahedron
$\frac{1}{\sqrt{2}} \approx .71$	$\frac{2}{\sqrt{2}} \approx 1.41$	1	$\frac{3 + \sqrt{5}}{2} \approx 2.62$	$\frac{1 + \sqrt{5}}{2} \approx 1.62$

From Table 9, the tetrahedral chassis offers the greatest mobility, because it is robust to disturbances, while not requiring large amounts of torque to step. From the analysis above, the tetrahedral chassis offers the greatest stability on slopes and the greatest disturbance rejection without requiring significantly more torque to make a step. These results informed our current selection of the rover's chassis. This analysis includes many simplifications and only represents a preliminary analysis of chassis shape. Further analyses are required to effectively evaluate each chassis design.

REFERENCES

- [1] F. A. Leve, B. J. Hamilton, and M. A. Peck, *Spacecraft Momentum Control Systems*, 1st ed., vol. 34. Springer International Publishing, Switzerland, 2015.
- [2] M. Peck, M. Paluszek, S. Thomas, and J. Mueller, "Control-Moment Gyroscopes for Joint Actuation: A New Paradigm in Space Robotics," in *1st Space Exploration Conference: Continuing the Voyage of Discovery*, Orlando, Florida, 2005.
- [3] D. S. Elliott and M. A. Peck, "Dynamics and Control of Polyhedral Surface Robots with Control Moment Gyroscopes," in *AIAA Guidance, Navigation, and Control Conference*, Grapevine, TX, 2017.
- [4] M. Peck, "Low-Power, High-Agility Space Robotics," in *AIAA Guidance, Navigation, and Control Conference and Exhibit*, San Francisco, California, 2005.
- [5] D. Li and H. Vallery, "Gyroscopic assistance for human balance," in *2012 12th IEEE International Workshop on Advanced Motion Control (AMC)*, Sarajevo, Bosnia-Herzegovina, 2012, pp. 1–6.
- [6] R. Votel and D. Sinclair, "Comparison of Control Moment Gyros and Reaction Wheels for Small Earth-Observing Satellites," in *The Small Satellite Conference*, Logan, UT, 2012.
- [7] D. Brown and M. Peck, "Energetics of Control Moment Gyroscopes as Joint Actuators," *J. Guid. Control Dyn.*, vol. 32, no. 6, pp. 1871–1883, 2009.
- [8] B. Thornton, T. Ura, Y. Nose, and S. Turnock, "Zero-G Class Underwater Robots: Unrestricted Attitude Control Using Control Moment Gyros," *IEEE J. Ocean. Eng.*, vol. 32, no. 3, pp. 565–583, Jul. 2007.
- [9] F. A. Leve and N. G. Fitz-Coy, "Hybrid Steering Logic for Single-Gimbal Control Moment Gyroscopes," *J. Guid. Control Dyn.*, vol. 33, no. 4, pp. 1202–1212, Jul. 2010.
- [10] L. L. Jones, R. A. Zeledon, and M. A. Peck, "Generalized Framework for Linearly Constrained Control Moment Gyro Steering," *J. Guid. Control Dyn.*, vol. 35, no. 4, pp. 1094–1103, Jul. 2012.
- [11] H. Kurokawa, "Survey of Theory and Steering Laws of Single-Gimbal Control Moment Gyros," *J. Guid. Control Dyn.*, vol. 30, no. 5, pp. 1331–1340, Sep. 2007.
- [12] D. S. Elliott, M. Peck, and I. A. D. Nesnas, "Novel Method for Control Moment Gyro Singularity Avoidance Using Constraints," in *AIAA Guidance, Navigation, and Control Conference*, Kissimmee, FL, 2018.
- [13] I. M. Ross and M. Karpenko, "A review of pseudospectral optimal control: From theory to flight," *Annu. Rev. Control*, vol. 36, no. 2, pp. 182–197, Dec. 2012.
- [14] J. Paradiso, "Global steering of single gimballed control moment gyroscopes using a directed search," *J. Guid. Control Dyn.*, vol. 15, no. 5, pp. 1236–1244, Sep. 1992.
- [15] S. R. Vadali and S. Krishnan, "Suboptimal command generation for control moment gyroscopes and feedback control of spacecraft," *J. Guid. Control Dyn.*, vol. 18, no. 6, pp. 1350–1354, 1995.
- [16] D. Cornick, "Singularity avoidance control laws for single gimbal control moment gyros," in *Guidance and Control Conference*, Boulder, Colorado, 1979.
- [17] T. Yoshikawa, "A steering law for three double-gimbal control moment gyro systems," NASA Marshall Space Flight Center, Huntsville, Alabama, NASA-TM-X-64926, Mar. 1975.

- [18] D. Brown and M. A. Peck, "Scissored-Pair Control-Moment Gyros: A Mechanical Constraint Saves Power," *J. Guid. Control Dyn.*, vol. 31, no. 6, pp. 1823–1826, Nov. 2008.
- [19] H. Kurokawa, "Constrained Steering Law of Pyramid-Type Control Moment Gyros and Ground Tests," *J. Guid. Control Dyn.*, vol. 20, no. 3, pp. 445–449, May 1997.
- [20] D. S. Elliott, M. A. Peck, and I. A. D. Nesnas, "Novel Method for Control Moment Gyroscope Singularity Avoidance Using Constraints," in *AIAA Guidance, Navigation, and Control Conference*, Kissimmee, Florida, 2018.
- [21] B. Wie, D. Bailey, and C. Heiberg, "Singularity Robust Steering Logic for Redundant Single-Gimbal Control Moment Gyros," *J. Guid. Control Dyn.*, vol. 24, no. 5, pp. 865–872, Sep. 2001.
- [22] B. Wie, "Singularity Escape/Avoidance Steering Logic for Control Moment Gyro Systems," *J. Guid. Control Dyn.*, vol. 28, no. 5, pp. 948–956, Sep. 2005.
- [23] K. A. Ford and C. D. Hall, "Singular Direction Avoidance Steering for Control-Moment Gyros," *J. Guid. Control Dyn.*, vol. 23, no. 4, pp. 648–656, Jul. 2000.
- [24] N. S. Bedrossian, J. Paradiso, E. V. Bergmann, and D. Rowell, "Steering law design for redundant single-gimbal control moment gyroscopes," *J. Guid. Control Dyn.*, vol. 13, no. 6, pp. 1083–1089, Nov. 1990.
- [25] B. Siciliano and O. Khatib, Eds., *Springer Handbook of Robotics*, 2nd ed. Springer International Publishing, 2016.
- [26] L. Sciavicco and B. Siciliano, "A dynamic solution to the inverse kinematic problem for redundant manipulators," in *1987 IEEE International Conference on Robotics and Automation Proceedings*, Raleigh, NC, 1987, vol. 4, pp. 1081–1087.
- [27] O. Egeland, "Task-space tracking with redundant manipulators," *IEEE J. Robot. Autom.*, vol. 3, no. 5, pp. 471–475, Oct. 1987.
- [28] I. A. D. Nesnas, "Proper Kinematic Constraint Functions of 'Smart' Redundant Wrists," Doctor of Philosophy, Notre Dame, Notre Dame, IN, 1992.
- [29] S. Yahya, M. Moghavvemi, and H. A. F. Mohamed, "Geometrical approach of planar hyper-redundant manipulators: Inverse kinematics, path planning and workspace," *Simul. Model. Pract. Theory*, vol. 19, no. 1, pp. 406–422, Jan. 2011.
- [30] S. Yahya, M. Moghavvemi, S. S. Yang, and H. A. F. Mohamed, "Motion planning of hyper redundant manipulators based on a new geometrical method," in *IEEE International Conference on Industrial Technology*, Gippsland, VIC, Australia, 2009, pp. 1–5.
- [31] Ye. Somov, S. Butyrin, S. Somov, and G. Anshakov, "GUIDANCE AND ROBUST GYROMOMENT ATTITUDE CONTROL OF AGILE FLEXIBLE REMOTE SENSING SPACECRAFT," *IFAC Proc. Vol.*, vol. 40, no. 7, pp. 533–538, Jan. 2007.
- [32] J. Crenshaw, "2-SPEED, a single-gimbal control moment gyro attitude control system," in *Guidance and Control Conference*, Key Biscayne Florida, 1973, p. 895.
- [33] T. Sands, J. J. Kim, and B. N. Agrawal, "Nonredundant Single-Gimballed Control Moment Gyroscopes," *J. Guid. Control Dyn.*, vol. 35, no. 2, pp. 578–587, 2012.
- [34] B. Wie, "Singularity Analysis and Visualization for Single-Gimbal Control Moment Gyro Systems," *J. Guid. Control Dyn.*, vol. 27, no. 2, pp. 271–282, 2004.
- [35] "The small exploration rovers, MINERVA-III," *JAXA*, 19-Sep-2018. [Online]. Available: <http://www.hayabusa2.jaxa.jp/en/topics/20180919e/>. [Accessed: 19-Mar-2019].

- [36] T. Yoshimitsu, T. Kubota, I. Nakatani, T. Adachi, and H. Saito, “Micro-hopping robot for asteroid exploration,” *Acta Astronaut.*, vol. 52, no. 2–6, pp. 441–446, Jan. 2003.
- [37] B. J. Hockman, A. Frick, R. G. Reid, I. A. D. Nesnas, and M. Pavone, “Design, Control, and Experimentation of Internally-Actuated Rovers for the Exploration of Low-gravity Planetary Bodies,” *J. Field Robot.*, vol. 34, no. 1, pp. 5–24, 2017.
- [38] M. Pavone, J. C. Castillo-Rogez, I. A. D. Nesnas, J. A. Hoffman, and N. J. Strange, “Spacecraft/rover hybrids for the exploration of small Solar System bodies,” in *2013 IEEE Aerospace Conference*, Big Sky, Montana, 2013.
- [39] A. Cavender, “Dynamics and Control of a Novel Spherical Robot,” presented at the University of California at San Diego Department of Mechanical Engineering Colloquium, San Diego, CA, 2012.
- [40] M. Kelly, “An Introduction to Trajectory Optimization: How to Do Your Own Direct Collocation,” *SIAM Rev.*, vol. 59, no. 4, pp. 849–904, Jan. 2017.
- [41] M. Kelly, *OptimTraj*. .
- [42] F. Piltan, M. Mirzaei, F. Shahriari, I. Nazari, and S. Emamzadeh, “Design Baseline Computed Torque Controller,” *Int. J. Eng.*, vol. 6, no. 3, pp. 129–141, Jun. 2012.
- [43] X. Roser and M. Sghedoni, “Control Moment Gyroscopes (CMG’s) and their Application in Future Scientific Missions,” in *Spacecraft Guidance, Navigation and Control Systems*, Keplerlaan, Noordwijk, Netherlands, 1996, vol. 381, pp. 523–528.
- [44] R. C. Hopkins *et al.*, “Xenia Mission: Spacecraft Design Concept,” NASA Marshall Space Flight Center; Huntsville, Alabama, United States, NASA Marshall Space Flight Center; Huntsville, Alabama, United States, Technical NASA/TM-2009-216270, Dec. 2009.
- [45] F. Zhu, D. S. Elliott, Z. Yang, and H. Zheng, “Genetic Algorithms for Autonomous, Learned Robotic Exploration in Extreme, Unknown Environments,” in *IEEE Aerospace Conference*, Big Sky, Montana, 2019.
- [46] M. Cutler and J. P. How, “Autonomous drifting using simulation-aided reinforcement learning,” in *2016 IEEE International Conference on Robotics and Automation (ICRA)*, Stockholm, Sweden, 2016, pp. 5442–5448.
- [47] Y. Pan *et al.*, “Agile Autonomous Driving using End-to-End Deep Imitation Learning,” in *Robotics: Science and Systems*, Pittsburgh, PA, 2018.
- [48] S. Prajna, A. Jadbabaie, and G. J. Pappas, “A Framework for Worst-Case and Stochastic Safety Verification Using Barrier Certificates,” *IEEE Trans. Autom. Control*, vol. 52, no. 8, pp. 1415–1428, Aug. 2007.
- [49] C. Sloth, G. J. Pappas, and R. Wisniewski, “Compositional Safety Analysis Using Barrier Certificates,” in *Proceedings of the 15th ACM International Conference on Hybrid Systems: Computation and Control*, New York, NY, USA, 2012, pp. 15–24.
- [50] S. Prajna and A. Jadbabaie, “Safety Verification of Hybrid Systems Using Barrier Certificates,” in *Hybrid Systems: Computation and Control*, vol. 2993, R. Alur and G. J. Pappas, Eds. Berlin, Heidelberg: Springer Berlin Heidelberg, 2004, pp. 477–492.